In vitro aqueous alteration experiments on cortical bone

Quantification and visualization of alteration effects from the micro- down to the atomic scale

Dissertation
zur
Erlangung des Doktorgrades (Dr. rer. nat.)
der
Mathematisch-Naturwissenschaftlichen Fakultät
der
Rheinischen Friedrich-Wilhelms-Universität Bonn

vorgelegt von
Anna Gabriele Kral
aus
Ulm

Bonn, 2022

Angefertigt mit Genehmigung
der Mathematisch-Naturwissenschaftlichen Fakultät
der Rheinischen Friedrich-Wilhelms-Universität Bonn

1. Gutachter: Prof. Dr. Thorsten Geisler-Wierwille, Universität Bonn
2. Gutachter: Prof. Dr. Thomas Tütken, Universität Mainz
Tag der Disputation: 30. September 2022
Erscheinungsjahr: 2022

Danksagung

Für die Vergabe des Themas, die Unterstützung, die hilfreichen Diskussionen und für die großen Freiheiten bedanke ich mich herzlich bei Prof. Dr. Thorsten Geisler-Wierwille. Prof. Dr. Thomas Tütken sei gedankt für interessante Diskussionen, seine Hilfsbereitschaft und seinen Rat, wenn ich nicht weiterwusste sowie für die herausfordernden Badmintonspiele. Ich bin froh, dass ich die letzten Jahre mit Euch zusammenarbeiten durfte!

Großer Dank gebührt meinen Kooperationspartnern, ohne welche diese Arbeit nicht möglich gewesen wäre: Denis Fougerouse, Fabian Gäb, Paul Guagliardo, Markus Lagos, William Rickard, David Saxey, Katrin Weber und Alexander Ziegler. Weiterhin möchte ich mich bei den Mitgliedern der Forschergruppe 2685 für anregende Diskussionen und Gespräche bedanken.

Bei allen Schlossbewohnern möchte ich mich für die Hilfsbereitschaft und das angenehme Miteinander bedanken. Ich bedanke mich besonders bei Daniela Bungartz und Dagmar Hambach für ihre vielseitige Unterstützung, bei Deniz Öz und Nils Jung für die geruchsintensive Präparation der Knochenproben sowie bei Gerrit Müller für seine Hilfe mit den Experimenten. Ich danke außerdem Moritz Fritzsche, Robin Strack und Fabian Gäb, die für viel Kurzweil, Spaß und die notwendige Ablenkung gesorgt haben, mir aber auch immer mit Rat und Tat zur Seite standen.

Dank gilt auch Sophie Ogan - ohne Dich wären die letzten Jahre sehr viel weniger erfreulich verlaufen!

Ganz besonders danken möchte ich Alexander Ziegler für den starken Rückhalt, die vielen hilfreichen Ratschläge und Diskussionen sowie für seine endlose Geduld.

Ich möchte mich zuletzt bei meiner Familie bedanken, inklusive Bobbi, Sedicus, Gecko, Arya und Denna. Ohne Euren Rückhalt, Eure Liebe und das Vertrauen in mich wäre es vermutlich nie zu dieser Arbeit und deren Abschluss gekommen. Euch widme ich diese Arbeit.

Diese Arbeit wurde finanziert von der Deutschen Forschungsgemeinschaft (GE 1094/23-1).

Abstract

This dissertation addresses the effects of early diagenetic processes on vertebrate bone's organic and inorganic constituents in an aquatic environment.

For this purpose, *in vitro* alteration experiments were performed on compact long bone material from a modern ostrich, as only recent bone allows before-and-after comparison in the context of diagenetic studies. The controlled experiments were performed on 3.5 mm-sized cylindrical cortical bone (CB) samples immersed in different aqueous solutions under simulated early diagenetic conditions. The variable parameters of the experiments were (1) temperature, (2) experimental duration, and (3) solution composition. Experiments were conducted at 30, 60, and 90 °C for up to 30 days in seawater (SW) and two different freshwater (FW) solutions with additional artificial sediment added to one of the freshwater solutions (FWS). After completion of the *in vitro* experiments, the bone samples and the corresponding experimental solutions were analyzed using state-of-the-art analytical methods: micro-computed tomography (µCT), electron microprobe analyzer (EMPA), nanoscale secondary ion mass spectrometry (nanoSIMS), atom probe tomography (APT), inductively coupled plasma-mass spectrometry (ICP-MS), Raman spectroscopy, and isotope ratio infrared spectrometry (IRIS).

In the first part of the present work, µCT was used to perform a detailed quantitative and qualitative characterization of the bone samples in 3D before and after the experiments. The results showed that the internal bone structure was barely changed under the different conditions. Only the samples from the FW experiments showed an increased weight loss with increasing experiment duration. Here, the loss of collagen rather than the dissolution of the mineral phase is assumed to be the causative factor since neither an increase in bone porosity nor an increase in calcium and phosphorus concentrations in the solution was observed. Furthermore, a bright reaction rim (RR) was detected by µCT in the same FW samples. Based on these data, chemical and mineralogical analyses were performed, described in the second part of this dissertation. Here, it was shown that the RR is caused by enrichment with heavy elements, which was already measurable shortly after the beginning of the experiments. Lighter elements were not only concentrated in the RR but also distributed into the bone through the cortical canals. However, the processes leading to the accumulation of elements in the CB are not purely diffusive as previously assumed but rather involve transport and reaction processes. In addition, new apatite was formed at least

in the RR of the bone samples, which is chemically and mineralogically different from the original bioapatite. In the experiments presented in the third part of this dissertation, the FW and SW solutions enriched with the isotope ^{18}O and the FWS solution with additional sediment containing calcium hydrogen phosphate labeled with ^{18}O were used to assess the growth of new apatite. This revealed that new fluorapatite was formed only in the bone samples that were in contact with sediment and not in those samples that were only in contact with an ^{18}O-enriched solution without an external phosphate source.

Based on the present work results, it was possible to derive a detailed phenomenological model describing the interactions between bone and aqueous solutions in an early diagenetic setting.

Table of Contents

List of Abbreviations

2D	two-dimensional
3D	three-dimensional
µCT	micro-computed tomography
a.u.	arbitrary unit
CCN	cortical canal network
CB	cortical bone
EMPA	electron microprobe analysis
FAp	fluorapatite
FW	freshwater (solution)
FWS	freshwater plus sediment (solution)
HAp	hydroxylapatite
HPLC	high-performance liquid chromatography
ICP-MS	inductively coupled plasma-mass spectrometry
IRIS	isotope ratio infrared spectrometry
LA	laser ablation
MALDI-TOF MS	matrix-assisted laser desorption/ionization coupled to time-of-flight mass spectrometry
nanoSIMS	nanoscale secondary ion mass spectrometry
PL	photoluminescence
qBEI	quantitative backscattered electron imaging
SE	secondary electron
SR	synchrotron radiation
SW	seawater (solution)
XRF	X-ray fluorescence

List of Figures

List of Tables

„Je mehr der Mensch versucht, göttliche Geheimnisse zu erforschen, desto mehr ist er dabei auf teuflische Erfindungen angewiesen.“

— Markus Weidmann

1 Introduction

The fossil record reflects the known history of life on Earth and comprises the remains of plants, bacteria, fungi, and animals preserved directly (body fossils) or indirectly (trace fossils) over geological time scales. When our planet formed about 4.55 billion years (Ga) ago (Tera, 1980; Dalrymple, 2001), it did not take long - from a geological time scale perspective - for the first life to evolve in the Archean (Fig. 1.1): the first, albeit indirect, evidence for life in the form of small hematite tube and filament trace fossils was found in 3.77 Ga-old hydrothermal vent precipitates from the ancient seafloor (Dodd et al., 2017). However, the earliest direct evidence for life, in the form of a microbial body fossil, was found in a 3.47 Ga-old Apex chert rock from Western Australia (Schopf et al., 2018).

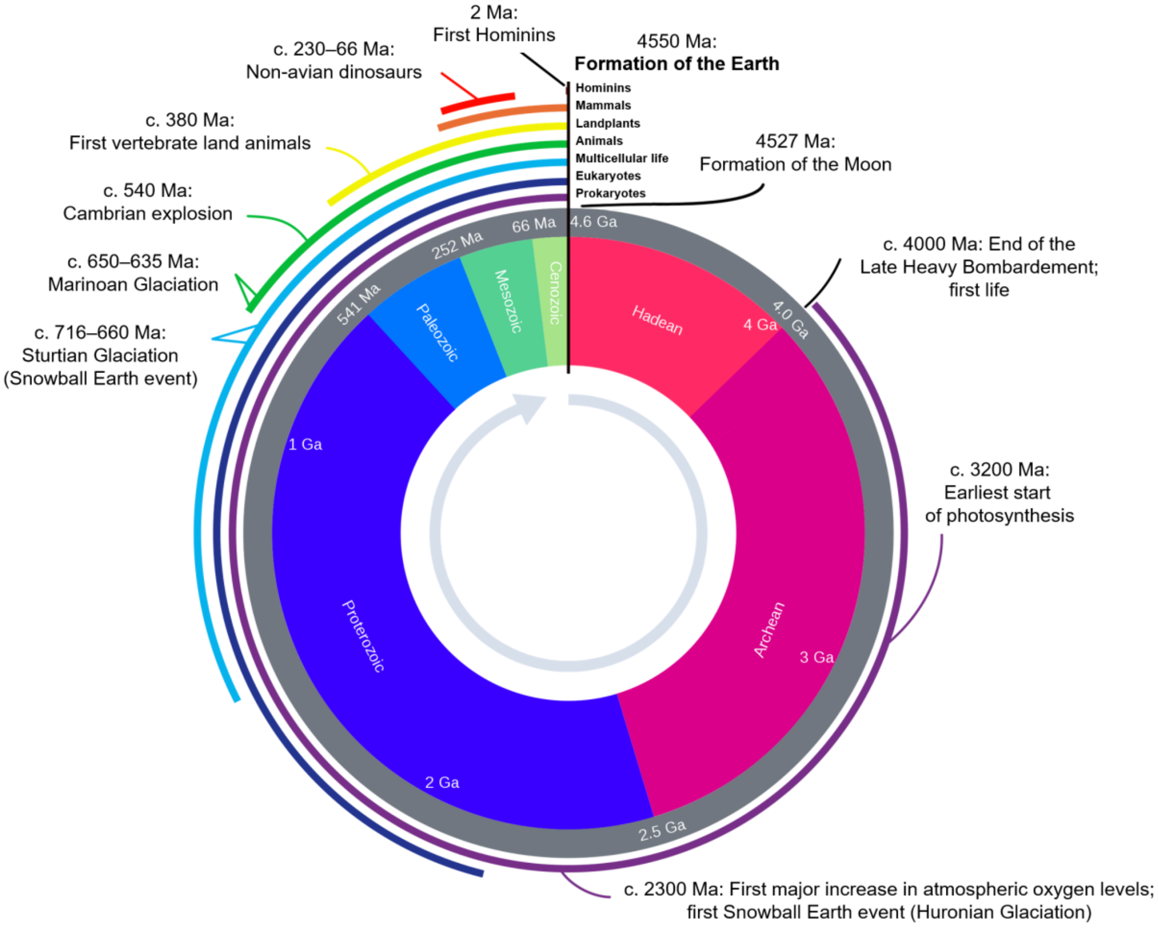

Figure 1.1 | The geological clock represents the Earth's history from its formation until now. The clock is subdivided into the Eons Hadean, Archean, Proterozoic, and Phanerozoic, with the latter subdivided into the Eras Paleozoic, Mesozoic, and Cenozoic. One hour on this clock stands for approximately 375 Ma. Ga = Giga years (billions of years), Ma =mega years (millions of years). Derivative work: Hardwigg, Public domain, via Wikimedia Commons.

Organisms with mineralized tissues, such as vertebrates (Chordata: Craniota), which yield many iconic body fossils, appear much later in the fossil record during the Phanerozoic (Fig. 1.1). The earliest jawed vertebrates (Craniota: Gnathostomata) are dated to the Early Silurian (Brazeau & Friedman, 2014), and the earliest tetrapod (Gnathostomata: Tetrapoda) body fossils to the Late Devonian (Daeschler et al., 2006). Despite their relatively late occurrence, fossilized skeletal tissues are an essential cornerstone of the fossil record, as they allow clarifying evolutionary hypotheses and reconstructions of past environmental and living conditions. Any evidence of life older than ≈ 10,000 a is considered a fossil, the age of fossilized bones thus ranges from about 10,000 a to more than 400 million years (Ma). Consequently, even the youngest fossil bones must have been exposed to changing external conditions over at least thousands of years, which is sure to have modified the bones' original structure and composition (e.g., Keenan, 2016; Dauphin, 2022). These so-called diagenetic alteration processes set in *post mortem* as soon as an organism dies and lead to the loss or even destruction of information on the macroscopic down to the molecular or atomic scale. Therefore, the fossilization process limits our understanding of the past. While the discovery of fossils makes our knowledge of the past richer, it is crucial to understand the fossilization process in detail in order to put these objects into a scientific perspective.

1.1 Bone structure and composition

Bone is a complex, hierarchically ordered nanocomposite material (Vellet-Regí & Navarrete, 2016; Reznikov et al., 2018; Talal et al., 2020; Buss et al., 2022), which can be divided into an outer cortical (or compact) and inner trabecular (or spongy/cancellous) compartment covered by the periosteum (Fig. 1.2). This study focuses on the cortical bone (CB), representing the most frequently encountered type of fossil bone. CB is hierarchically organized on different scales (Currey, 2011; Currey & Shahar, 2013; Reznikov et al., 2014a, b; Liu et al., 2016; Doineau et al., 2021), with osteons forming the largest constituent units (Fig. 1.2). Osteons consist of osteonal bone, i.e., concentric layers of lamellar bone with osteocyte lacunae, whereby the latter is connected via canaliculi. Osteonal bone surrounds the so-called Haversian canals, which *in vivo* host blood vessels and nerves (Fig. 1.2). Haversian canals, in turn, are interconnected via Volksmann's canals that are oriented transversely and in living bone tissue contain additional blood vessels for nutrition. Although CB is permeated by a complex microstructural canal network, its porosity ranges, depending on the given vertebrate, from only 2 to 5 % (Cooper et al., 2016; Kral et al., 2021; chapter 2). The remaining 95 to 98 % are bone mass, which consists of a mineralized extracellular matrix (Reznikov et al., 2016) comprised of an organic (20-25 wt.%) and an inorganic phase (60-65 wt.%) as well as ca. 10 wt.% of water (Rogers & Zioupos, 1999).

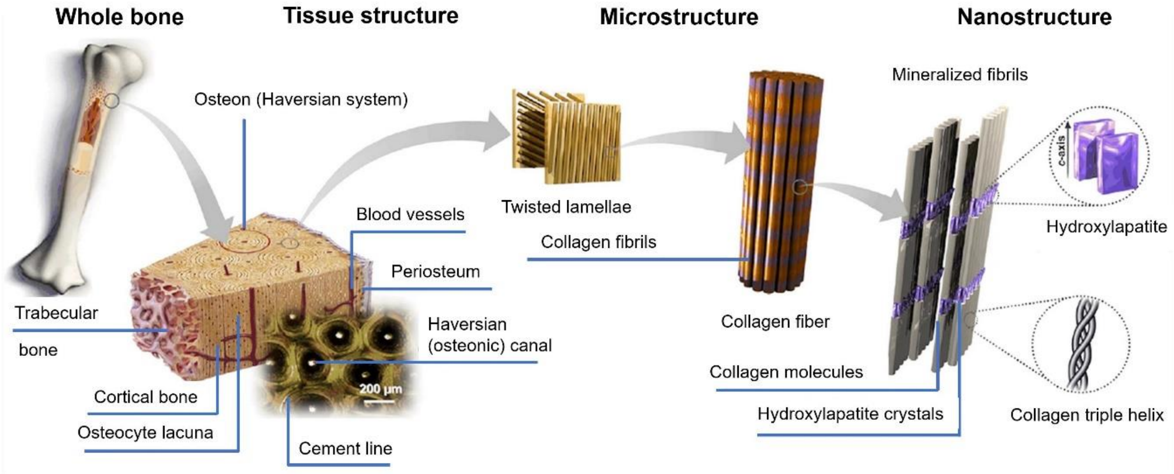

Figure 1.2 | Illustration of the hierarchical organization of CB. The four structural levels are (1) the whole bone or macroscopic level, (2) the bone tissue or mesoscopic level, (3) the microstructural, and (4) the nanostructural level (modified after Sadat-Shojai et al., 2013).

The inorganic fraction consists of biogenic hydroxylapatite (HAp), also termed bioapatite (Fig. 1.2), which is a nanocrystalline, carbonated calcium phosphate apatite (LeGeros et al., 1969, 1984; Combes et al., 2016). Its chemical formula was proposed to be $Ca_{10-x}[(PO_4)_{6-x}(CO_3)_x]$ $(OH)_{2-x}\cdot/CO_3$ nH_2O (Wopenka & Pasteris, 2005; Pasteris et al., 2014), where n ~1.5 and x ranges between about 0.4 and 1.0. Carbonate can substitute for either the phopshate (B-type substitution) or the hydroxyl (A-type substitution) group in bioapatite (Tonegawa et al., 2010; Madupalli et al., 2017). In fossil bone, the hydroxyl group is usually replaced by fluorine (e.g., Pasteris & Ding, 2009; Qiao et al., 2017). Calcium in the bone apatite structure can partially be substituted by many mono-, di- or trivalent metals, such as magnesium, zinc, strontium, sodium, or rare earth elements (REEs) (e.g., Pan & Fleet, 2002; Boanini et al., 2010). The organic phase primarily consists of mineralized type-I collagen fibers comprised of bundled collagen triple helices whose framework is reinforced by *in vivo* precipitated bioapatite nano-crystallites (Fig. 1.2) (Shoulders & Raines, 2010; Reznikov et al., 2013, 2015). However, the organic phase also contains a few non-collagenous proteins such as osteocalcin, osteonectin, and osteocytes, i.e., bone cells that maintain metabolism (Kini & Nandeesh, 2012).

Thus, bone is a living, mineralized hard tissue and is considered a highly specialized endocrine organ (Guntur & Rosen, 2012; Morgan et al., 2013). The primary bone functions are - besides acting as a supporting (biomechanical) framework for the entire body - to regulate calcium homeostasis, i.e., control of the amount of calcium in the blood (Rigo et al., 2012) as well as hematopoiesis, i.e., the formation of blood cells and blood plasma (Sommerfeldt & Rubin, 2001). During a vertebrate's lifetime, its bone tissues are continuously replaced during the so-called bone remodeling cycle (Fig. 1.3) (Parfitt, 1994; Kenkre & Bassett, 2018 and references therein). This cycle lasts for about 120 or 200 days in cortical and trabecular bone, respectively (Agerbaek et al., 1991).

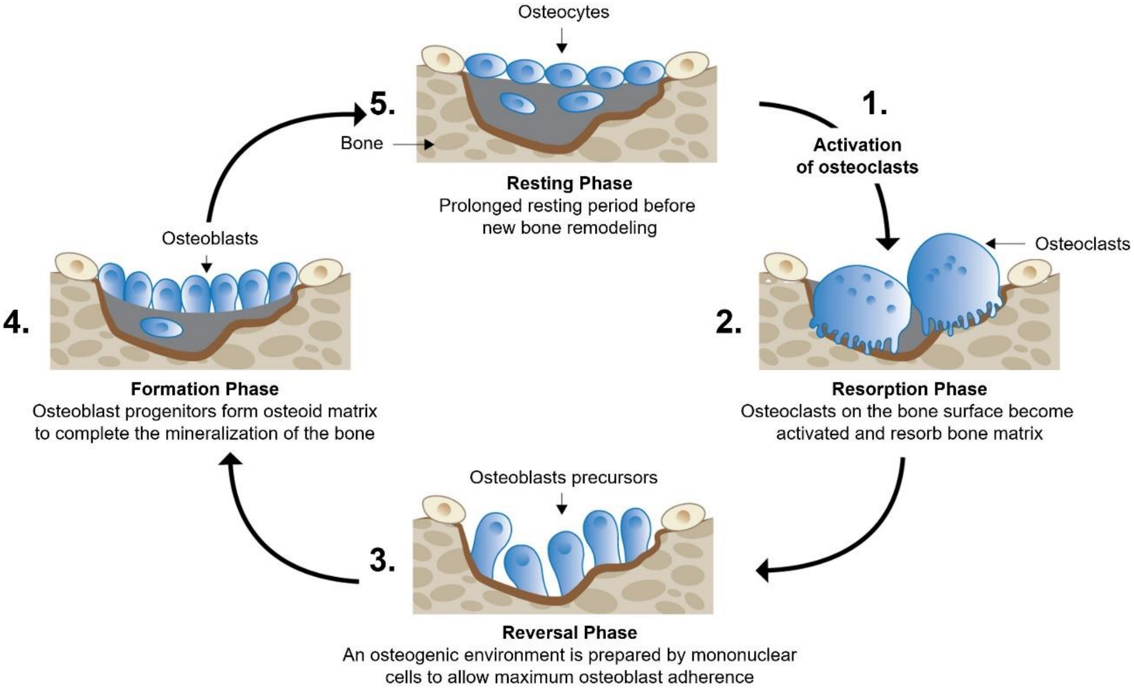

Figure 1.3 | Schematic illustration of the five phases of the bone remodeling cycle. Bone remodeling constantly occurs throughout the life of a vertebrate organism and ideally leads to repeated renewal of the entire skeletal tissue (modified after Beck-Nielsen et al., 2021).

During the bone remodeling cycle, five steps occur repetitively in so-called basic multicellular units (Frost, 1969; Smith et al., 2012): (1) the activation of osteoclast precursor cells (Fig. 1.3-1) initiates (2) the osteoclastic resorption of the bone matrix (Fig. 1.3-2), which is followed by (3) a reversal phase (Fig. 1.3-3). There is a lack of knowledge about this particular phase, but it is probably an essential step for linking bone resorption to the bone formation by creating an osteogenic environment at remodeling sites that improve osteoblastic adherence. For new bone tissue to form inside this space, (4) osteoblasts enter the previously cleared resorption space, deposit a cement line surrounding it, and fill the resorption space (Fig. 1.3-4). Finally, (5) the cycle is repeated after a resting phase (Fig. 1.3-5). All remodeled structures are called secondary osteons and are bordered by highly mineralized cement lines. In contrast to primary osteons, only osteons formed initially by cartilage mineralization are considered primary osteons (Martin & Burr, 1989).

In addition to the structural renewal of bone, its chemical composition is also altered during the bone remodeling process. Throughout life, bones are permanently supplied with nutrients, oxygen, and sometimes toxic elements via the bloodstream (Marenzana & Arnett, 2013). The bone remodeling cycle and bone remodeling-independent ion exchange processes between bone and blood (Kelly & Bassingthwaighte, 1977; Marenzana et al., 2005; Wang et al., 2020) lead to the incorporation of these elements. For instance, bone tissue can incorporate poisonous "bone-seeking" elements to avoid their accumulation in soft tissues (O'Flaherty, 1991a, b; Bahia et al., 2020), e.g., strontium (Dow & Stanbury, 1960; Dahl et al., 2001; Marx et al., 2020), lead (Barry, 1975; O'Flaherty, 1991c, 1993, 1995), or uranium (Rowland & Farnham, 1969; Larivière et al., 2013; Wang et al., 2020). This is possible because bioapatite is a highly reactive phase with a flexible crystal lattice for chemical substitution (Ressler et al., 2021). Therefore, while bone must be considered the body's "trash can", it is also a valuable source of information as bone continuously adopts the blood's actual chemical and isotopic compositions, which in turn strongly depends on and reflects the isotopic and chemical composition of the organism's ingested food (e.g., Toots & Voorhies, 1965; Schweizer et al., 2007; Barrios-de Pedro et al., 2020), water (Longinelli, 1984; Kohn, 1996), as well as the air it is breathing (e.g., Gehler et al., 2011; Pack et al., 2013; Feng et al., 2022). Consequently, the bone's chemical and isotopic composition is representative for an average of the surrounding environmental conditions over a longer interval of time (Erel et al., 2021; Sykut et al., 2021). Thus, if the surrounding physical and chemical environment changes during the lifetime of an organism, this information will be recorded in the bioapatite's chemical and isotopic composition. Unfortunately, during fossilization, such information will not necessarily be preserved.

1.2 Bone as a source of information

Fossilized skeletal tissues are presumably the most abundant preserved physical evidence of life in a land before time. With chemical and isotopic information stored *ante* and *post* *mortem*, these signatures have become important tools for reconstructing the life history and living conditions of vertebrates, as well as for reconstructing their *post mortem* history (Fig. 1.4). The following paragraphs provide a brief overview of the information stored in bone *ante* and *post mortem*.

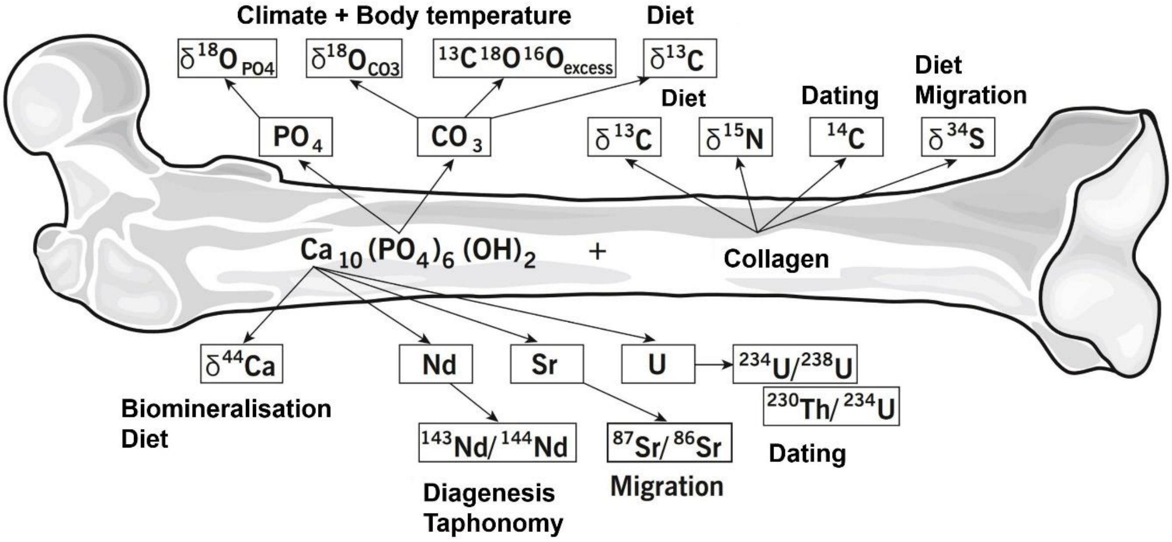

Figure 1.4 | Schematic sketch of a bone with information obtained from the apatite mineral phase and bone collagen (modified from Tütken & Vennemann, 2011). Note that calcium can be replaced by several elements such as neodymium, lutetium, strontium, and uranium.

The traditional stable isotopes of carbon and nitrogen were the first used for reconstructing dietary behavior and trophic levels in fossil species (Fig. 1.4). They were predominantly used to differentiate between carnivores, insectivores, omnivores, and herbivores (DeNiro & Epstein, 1978; DeNiro & Epstein, 1981; Caut et al., 2008; Krajcarz et al., 2018; Leichliter et al., 2020). For instance, isotopic analysis using $\delta^{13}C$ and $\delta^{15}N$ values showed that the primary protein source of European Neanderthals were large terrestrial herbivores such as horses, bovids, mammoth, and woolly rhinoceros (Richards et al., 2000, 2008; Bocherens et al., 2005; Richards & Trinkaus, 2009; Bocherens, 2009; Jaouen et al., 2019; Wißing et al., 2019; Drucker et al., 2021; Hardy et al., 2022). However, technical and methodological advances in mass spectrometry established non-traditional stable isotope ratios as new dietary indicators (Martin et al., 2017; Tacail et al., 2020), in particular, calcium ($\delta^{44}Ca$: Heuser et al., 2011; Reynard et al., 2011; Dodat et al., 2021), magnesium ($\delta^{26}Mg$: Martin et al., 2014, 2015; Nitzsche et al., 2020), and zinc ($\delta^{66}Zn$: Jaouen et al., 2016a, b; Bourgon et al., 2020).

Furthermore, information about past climatic conditions is stored in the phosphate ($\delta^{18}O_P$) and carbonate ($\delta^{18}O_C$) oxygen isotope composition in fossil vertebrate bone (Fig. 1.4) (e.g., Gehler et al., 2012; Wierzbowski, 2021 and references therein) as this composition reflects the oxygen isotope signature of meteoric water ($\delta^{18}O_W$) ($\delta^{18}O_P$: Longinelli et al., 1973; Longinelli, 1984; Fricke & O'Neil, 1999; Luz & Barkan, 2010; Passey & Levin, 2021 and references therein; $\delta^{18}O_C$: Iacumin et al., 1996; Sponheimer & Lee-Thorp, 1999; Göhring et al., 2018). The precipitation of biogenic apatite occurs in oxygen isotope composition equilibrium with body fluids, which are mainly characterized by the oxygen isotope signature of the ingested water and food (Kolodny et al., 1983; Luz & Kolodny, 1985; Amiot et al., 2017; Green et al., 2018; Fraser et al., 2021). Thus, variations in the precipitation temperature of biogenic phosphate are recorded in the $\delta^{18}O_P$ signature and permit reconstructing the mean annual air temperature during the final years of an animal's lifetime. A box model was developed by Langlois & Lécuyer (2003) that allows determining surrounding environmental (e.g., air temperature, relative humidity) and physiological (e.g., body mass, diet) parameters of a fossil vertebrate based on $\delta^{18}O_P$ signatures. In addition, $\delta^{18}O_P$ and the clumped isotope composition of the structurally bound CO_3 ^{13}C-^{18}O isotopic composition (Fig. 1.4) provides information about thermophysiology, i.e., the mean body temperature ($\delta^{18}O_P$: e.g., Kolodny et al., 1996; Bernard et al., 2010; CO_3 ^{13}C-^{18}O: Eagle et al., 2010, 2011, 2015; Suarez & Passey, 2014; Dawson et al., 2020). Further, oxygen isotopes in skeletal bioapatite can also be used for assessing the diagenetic alteration of bioapatite (e.g., offset between $\delta^{18}O_P$ and $\delta^{18}O_C$: Iacumin et al., 1996; Pellegrini et al., 2011; triple oxygen isotope composition of $\delta^{18}O_P$: Gehler et al., 2011).

Apart from reconstructing climatic conditions and dietary behavior, information on geographic location and migration behavior is also essential for reconstructing life on Earth. Strontium isotopes ($^{87}Sr/^{86}Sr$) in bones or teeth (Fig. 1.4) serve as a geochemical fingerprint for the geographic area (overview in Bentley, 2006), which is also a helpful tool for studying the migration of individuals or even entire populations. In addition, using this approach, local and non-local traces in diet or burial patterns can be differentiated (Copeland et al., 2008; Maurer et al., 2012; Lugli et al., 2017; Burton & Katzenberg, 2018; Weber et al., 2020; Tütken et al., 2020). More specifically, the $^{87}Sr/^{86}Sr$ in bone and tooth mimics the ratios of ingested food and water, thus reflecting the local geological terrain inhabited during tissue formation. However, after crown mineralization, the $^{87}Sr/^{86}Sr$ in mammalian tooth enamel does not change over time; $^{87}Sr/^{86}Sr$ is, therefore, representative of the bioavailable Sr ingested during childhood. In contrast, the bone remodeling cycle mentioned above leads to a continuously evolving $^{87}Sr/^{86}Sr$ in a given bone. Bone $^{87}Sr/^{86}Sr$ values thus reflect the last ontogenetic year and provide insights into the individual's place of death. For example, bone and tooth $^{87}Sr/^{86}Sr$ data recently revealed that the mobility among the ancient Maya in Mesoamerica was not restricted to their homeland and cultural boundaries. Instead, the range of their trading networks and resource acquisition extended much further. In addition, isotopic evidence was found that non-Mayan people were also part of their community (Miller Wolf & Freiwald, 2018).

However, *post mortem*, all biological processes inside the body suddenly cease, and bone is no longer in equilibrium with the body fluids shortly after. In the following, bone is continuously modified to reach equilibrium with the site-specific physicochemical conditions, significantly affecting its chemical and isotopic composition. For instance, extant bones contain only very low REE concentrations, while fossil bone can contain REE concentrations of up to several thousand ppm (Reynard et al., 1999; Lécuyer et al., 2003). Thus, it is generally assumed that REE uptake in bone occurs predominantly *post mortem* (Wang et al., 2020); therefore, they constitute an excellent measure of the *post mortem* interaction between bone and diagenetic fluids (e.g., Trueman, 1999). Concentration profiles of REEs and their spatial distribution in bone have great potential for revealing information about diagenetic conditions as well as taphonomy and fossilization history (Fig. 1.4) (Trueman & Benton, 1997; Thomas et al., 2007, 2011; Tütken, 2003, 2014; Tütken et al., 2008; Suarez et al., 2010; Herwartz et al., 2013a; McCormack et al., 2015; Decrée et al., 2018). Uranium and vanadium are suggested as proxies to determine whether the inorganic phase in fossil bone is diagenetically altered (Fig. 1.4) because these elements are not incorporated in significant amounts *in vivo* (Grimstead et al., 2018). Furthermore, it has recently been shown that REE concentration profiles in fossil bones are a suitable proxy for assessing the degree of soft tissue and biomolecular preservation (Ullmann et al., 2020).

Finally, determining the age of a given fossil is essential for a correct chronological classification of these objects in the fossil record. Fossils younger than 50,000 a can be dated using radiocarbon (^{14}C) dating (Fig. 1.4) if sufficient organic material is preserved and/or if the CO_3 group is still intact (Taylor, 1992, 2000; Zazzo & Saliège, 2011; Zazzo et al., 2012; van der Plicht & Palstra, 2016; Willoughby, 2016; Cersoy et al., 2017). However, due to the short half-life (ca. 5,700 a) of the radiogenic carbon isotope ^{14}C, this method is not suitable for fossils older than 50,000 a. Interestingly, incorporating other natural radiogenic elements present during early diagenesis enables the direct dating of older fossil remains (Fig. 1.4) (Grün, 2006; Grün et al., 2010 and references therein). For example, the age of fossils has been determined with different success using (1) uranium-series (Pike et al., 2002; Grün et al., 2014; Farkh et al., 2015), (2) electron spin resonance (Grün, 2008; Joannes-Boyau, 2014; Richard et al., 2017), (3) lutetium-hafnium (Barfod et al., 2003; Kocsis et al., 2010; Herwartz et al., 2013b), (4) (uranium, thorium)-helium (Fanale & Schaeffer, 1965; Kramers & Makhubela, 2022; Makhubela & Kramers, 2022), (5) uranium-thorium (Hellstorm & Pickering, 2015; Dirks et al., 2017), as well as (6) uranium-lead (Romer, 2001; Balter et al., 2008; Tomaschek et al., 2008) dating.

1.3 Diagenetic bone alteration

In general, reconstructions of past conditions of vertebrates are primarily based on their bone (and tooth) apatite and collagen's chemical and isotopic compositions. However, these two main phases that constitute bone are subject to diagenetic alteration during bone taphonomy and fossilization. The term taphonomy encompasses all biological and physicochemical processes initiated after death until the organism's decomposition or preservation and finally its discovery as a fossil. All *post mortem* processes that lead to post-depositional physicochemical changes are grouped under diagenesis (Lyman, 2010). However, this definition is not uniform and may differ slightly depending on the scientific field. Regardless of the definition, all of these processes lead to *post mortem* modifications of the *in vivo* incorporated major and trace elemental as well as isotopic compositions in bone (Tütken & Vennemann, 2011; Kohn et al., 1999, 2013). Therefore, it is paramount to identify and understand the processes occurring during fossilization and their effects on the original organic and inorganic fractions of bone to reconstruct the past ecology of vertebrates.

In the following, a brief introduction to the current knowledge on fossilization is provided, focusing on early diagenetic bone alteration (please see the overviews in Hedges, 2002; Trueman & Martill, 2002; Keenan, 2016, 2021; Dauphin, 2022 for a more detailed description). Fossilization is the transition from a once-extant organism to a fossil specimen (Fig. 1.5), beginning with (1) the organism's death and subsequent decay of its soft tissues. During and after (2) the deposition of the hard tissues (soft tissue is rarely preserved), (3) recrystallization and permineralization processes lead to the preservation of these hard tissues. Erosion and weathering can eventually lead to (4) the exposure of the fossil and its potential discovery, but also to its destruction (Forbes, 2014). However, an unquantifiable number of fossils will probably never be discovered.

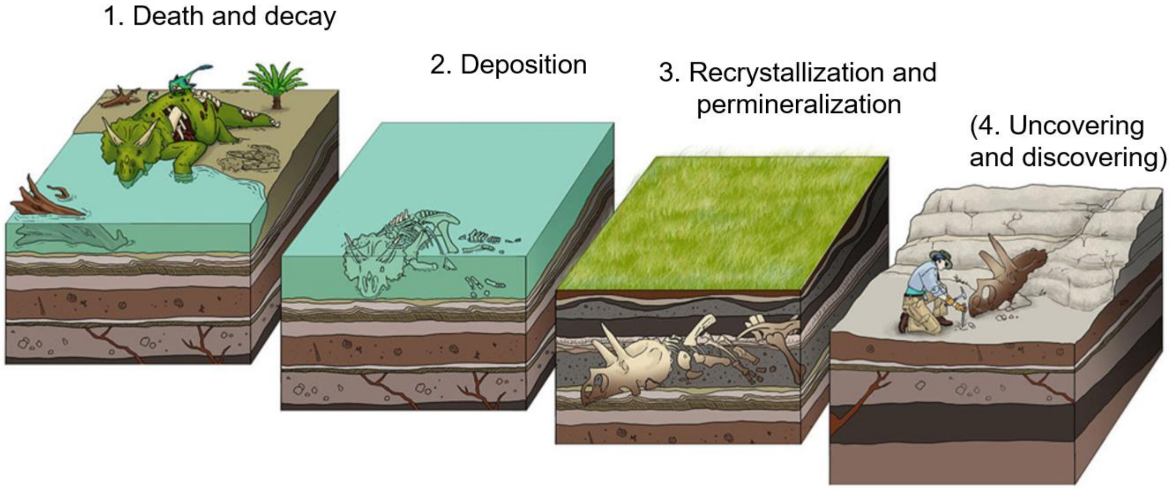

Figure 1.5 | Illustration of the three main steps of fossil formation under perfect conditions until the fossil is discovered. (image courtesy Becky Barnes).

Ante mortem, bone is in relative equilibrium with the body fluids through homeostasis. However, *post mortem*, after the decay of the soft tissues, the skeletal tissues come into contact with the surrounding natural environment. From this point on, the bone tissue is usually no longer stable and undergoes various structural and compositional modifications before, during, and after burial, leading to its preservation or decomposition (Müller, 1992; Denys, 2002; Kendall et al., 2018). Soft tissue, such as muscle or dermis, is the first to break down, primarily due to biostratinomic processes (Grupe & Harbeck, 2015). This alteration ultimately leads to the exposure of hard tissue to the environment, which initializes the biotic and abiotic alteration of bone. These steps, also called bone diagenesis, can be divided into an early and a late phase (Pfretzschner, 2004). At the beginning of the early diagenetic stage (Fig. 1.6), microbial activity, i.e., bioerosion (Jans, 2008; Turner-Walker, 2012; Kendall et al., 2018) and chemical hydrolysis of collagen set in, both resulting in an increased porosity of bone tissue (e.g., Collins et al., 1995, 2002; Nielsen-Marsh & Hedges, 2000; Truemann & Tuross, 2002). Collagen degradation is critical for initial bone alteration because collagen loss opens additional pathways for fluid penetration and exposes bioapatite crystallite surfaces to ambient conditions, thus initiating the diagenesis of highly reactive nm-sized bioapatite crystals (Fig. 1.6).

There are only two options for the bone in this highly vulnerable state, both depending on the environmental conditions: preservation or degradation. During this early stage of diagenetic alteration, the bone's thermodynamic stability is controlled by pH as well as the composition of the ambient diagenetic fluid (Berna et al., 2004). Solutions with low pH and low calcium and phosphate concentration facilitate dissolution, whereas fluids with neutral to slightly alkaline pH and in equilibrium or supersaturated with respect to the bioapatite mineral phase increase the chances of bone preservation (Berna et al., 2004). Another factor controlling the chemical milieu is that bioerosion and chemical alteration of the organic phase leads to an influx of collagen degradation products into the fluid circulating in the bone's canal network (Pfretzschner, 2004).

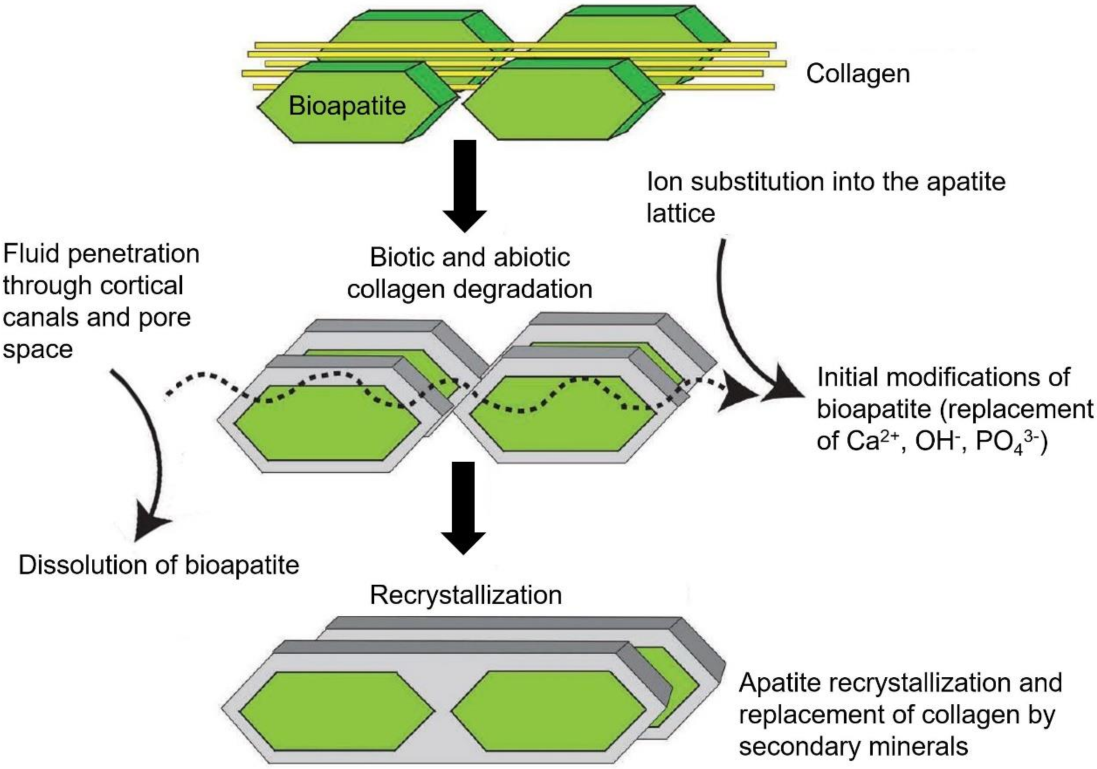

Figure 1.6 | Schematic model of diagenetic bioapatite alteration starting with the intact mineral-collagen-composite material, which gets decomposed first and opens pore spaces. Diagenetic solutions enter the bone via cortical canals and newly created pore space initiating apatite recrystallization and the formation of secondary authigenic minerals that fills inter-crystalline pore space and replaces collagen (modified after Keenan, 2016).

Several processes have been identified to be responsible for the structural and chemical changes (Fig 1.7) that constitute the prerequisite for bone preservation: (1) collagen replacement and filling of cavities through precipitation of secondary minerals, including, e.g., fluorapatite, carbonate, and iron minerals (Wings, 2004) (Fig. 1.7A), (2) ion-exchange between solution and bone apatite, e.g., adsorption of ions at surface sites of bioapatite crystallites or diffusion (Fig. 1.7B; Millard & Hedges 1996; Berna et al., 2004; Kohn, 2008; Trueman et al., 2008), and (3) dissolution-reprecipitation processes (Pasteris & Ding, 2009; Hinz & Kohn, 2010), including so-called Ostwald ripening (Fig. 1.7C). During such fluid-mineral interactions, larger and thermodynamically more stable apatite crystallites with strongly varying compositions are formed (Goodwin et al., 2007). In general, during bone recrystallization, the shape of the bone and its crystallites must not necessarily differ from their original shape (Fig. 1.7D), i.e., pseudomorphs are formed (Kolodny et al., 1996; Pasteris & Ding, 2009) - possibly by an interface-coupled dissolution-precipitation process that recently has been proposed for several mineral replacement reactions (Putnis et al., 2002; Putnis & Putnis, 2007; Ruiz-Agudo et al., 2014; Renard et al., 2019; Deng et al., 2022).

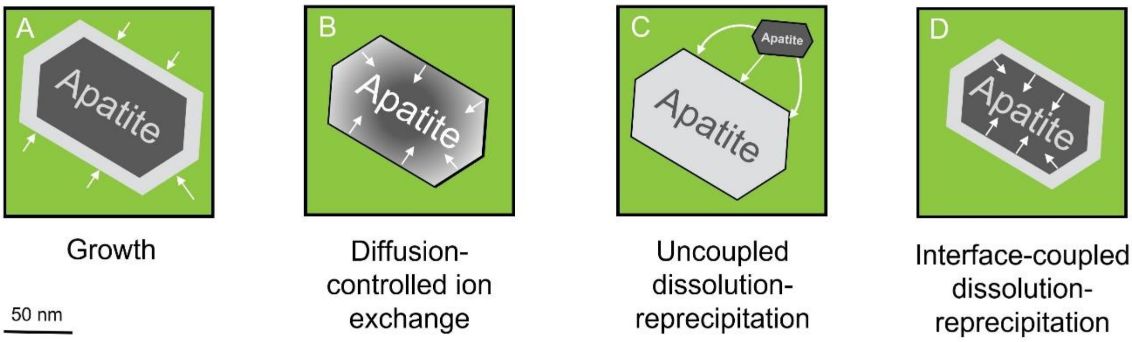

Figure 1.7 | Schematic illustration of re-equilibration and apatite growth processes that may be active during early diagenesis of bone apatite. White arrows indicate the direction of mass transport.

The transition from early to late diagenesis is marked by the complete replacement of collagen with minerals, a change in the chemical milieu, and a slowdown of the alteration processes (Pfretzschner, 2004). This late phase is characterized by the pH-dependent precipitation of minerals in bone cavities (e.g., cracks or canals) rather than by rapid decay or recrystallization processes.

The processes mentioned above occurring during early and late diagenesis illustrate that bone undergoes complex *post mortem* modifications over time on a structural and compositional level.

1.4 A significant bias in the fossil record

A fundamental question that has troubled researchers from various disciplines for decades is whether the fossil record accurately reflects the history of life on Earth. In fact, it is now becoming increasingly clear that there is a significant bias in the fossil record. Whether an extinct species is represented in the fossil record or not depends on multiple factors, such as the period that a given species existed on Earth, the location it was native to, the number of its individuals, or their physical characteristics (Plotnick et al., 2016). Furthermore, animals with a mineralized endo- or exoskeleton are more likely to be fossilized than entirely soft-bodied animals, as soft tissues usually decay relatively quickly during early diagenesis. Interestingly, over 90 % of all discovered fossils inhabited one of the many marine habitats. In contrast, terrestrial organisms are rarely fossilized, and if so, it is usually in aquatic settings as the presence of water enhances fossilization. Therefore, it follows that particular diagenetic conditions must prevail for organisms to fossilize, resulting in an unknown number of species that so far do not and presumably will never appear in the fossil record. In addition, the constant knowledge gain, as well as the advances made concerning technical and analytical methods, have shown that mineralogical and chemical overprinting and associated loss of chemical information must occur during the highly complex fossilization process. Unfortunately, these circumstances render the reconstruction of the past a difficult task. Nevertheless, far-reaching conclusions are often drawn based on information stored in fossil bones and teeth. Admittedly, these fossil remains of vertebrates preserved in the sedimentary record are frequently the only possible source of information. Consequently, in order to correctly interpret and classify the preserved information, the limitations of the fossil record must be identified and understood, which requires an in-depth understanding of the process of fossilization. A large field of research focuses on this aspect, seeking to understand how an organism fossilizes, what processes occur during fossilization, what influence these processes may have on the organic and inorganic constituents of bone (or tooth), and how reliable the standard paleo-proxies are.

Fossil vertebrate remains have been extensively studied using conventional histological and analytical methods, resulting in a basic understanding of fossilization. However, in order to unambiguously investigate early diagenetic processes and to determine the diagenetic conditions required for fossilization, several comparative experimental and analytical approaches have recently proven useful (e.g., Berna et al., 2004; Munro et al., 2007; Kohn & Moses, 2013; Snoeck et al., 2015; Keenan & Engel, 2017; Aufort et al., 2019b; Gäb et al., 2020; Kral et al., 2021; chapter 2; Weber et al., 2021). The continuous development of analytical methods offers multiple opportunities, including analyses at different length scales. At the same time, high-throughput studies have become possible, effectively broadening the spectrum of data used for conclusions.

Over the last decades, it has become increasingly popular to visualize the element and isotope distribution in bones complemented by quantitative data (Simpson et al., 2021 and references therein). Established tools for element mappings of bones are X-ray fluorescence (XRF) techniques with and without a synchrotron radiation (SR) source (Gilfrich et al., 1983; Smolek et al., 2010; Pemmer et al., 2013; Streli et al., 2019; Turyanskaya et al., 2021) as well as laser-ablation inductively coupled plasma-mass spectrometry (LA-ICP-MS) (König et al., 2009; Hare et al., 2011; Rasmussen et al., 2020).

In a recently published study, µ- and nano-XRF with spot sizes of 50 µm x 50 µm and 500 nm x 600 nm, respectively, were used to visualize the distribution of Mg, Y, and Zn in bones (Streli et al., 2019). µ-XRF usually allows for qualitative and semi-quantitative analysis of medium- and high-Z elements, while vacuum conditions are required to detect low-Z elements (Smolek et al., 2010), and an SR source is necessary to measure low concentrations of elements, so-called ultra-trace elements (Gilfrich et al., 1983). SR-nano-XRF with a resolution of ≈ 500 nm appears to be a good tool for investigating small structures in bone tissue, although this approach is restricted to tiny and thin samples. A combination of SR µ-XRF with a spatial resolution of 1 µm per pixel with quantitative backscattered electron imaging (qBEI) was successfully used to determine the distribution and accumulation of the trace elements Zn, Pb, and Sr in human bone (Pemmer et al., 2013). In turn, using LA-ICP-MS allows for producing quantified element distribution maps, first shown for REEs and U with spot sizes varying from 5 - 300 µm and a detection limit for REEs of approximately 1 ppm in Late Cretaceous bones (Koenig et al., 2009). A similar approach was used to determine and quantify the distribution of ^{66}Zn, ^{88}Sr, ^{111}Cd, and ^{208}Pb in tooth bioapatite with a spatial resolution of 30 µm x 30 µm (Hare et al., 2011). Another approach to determine the local element concentrations is to combine LA-ICP-MS measurements for element mappings with solution ICP-MS to calibrate the data acquired by LA-ICP-MS (Rasmussen et al., 2020). However, the low spatial resolution (i.e., in the µm range) of most of these methods (except for nano-XRF, which is, however, limited to tiny samples) is a limitation for investigating the distribution and accumulation of isotopes, trace elements, and REEs in fossil bones in high (i.e., sub-µm) spatial resolution. As outlined above, bone is a heterogeneous material with complex microarchitecture and histological features on the sub-micrometer scale (Fig. 1.2). Thus, to analyze trace elements individually as well as isotope distribution (and composition), analytical techniques with a spatial resolution at the nanometer scale are required. Atom probe tomography (APT) has previously been shown to provide deep insights into the bone's hierarchical structure and chemical composition at the atomic level (Langelier et al., 2017), but only for nanometer-scale samples. A method for investigating larger samples with high (i.e., sub-µm) resolution is nanoscale secondary ion mass spectrometry (nanoSIMS). This technique was developed explicitly for (trace) elemental and high-precision isotopic analysis with the highest spatial resolution of solid samples. Although these properties make nanoSIMS a suitable method for the above-mentioned bone analysis, it has not yet been used in bone research.

1.5 Focus and aims of the present thesis

This dissertation presents the results of a sub-project within the DFG Research Unit FOR 2685 "The Limits of the Fossil Record: Analytical and Experimental Approaches to Fossilization", which addresses the fundamental question of the origin of fossils from different perspectives and with different analytical approaches. In this context, the present thesis investigates how early diagenetic processes affect the CB's inorganic and organic components, thereby directly impacting its preservation or degradation potential. To this end, controlled, isothermal aqueous alteration experiments were performed on CB samples originating from a modern ostrich to shed light on the taphonomic processes occurring during the first days to weeks *post mortem*. Different physicochemical parameters were chosen to mimic conditions potentially encountered in an early diagenetic aquatic depositional setting. A novel multi-method approach was pursued, which combined qualitative and quantitative analytical techniques with comparatively low (µCT: 3 µm isotropic voxel resolution), medium (EMPA: 0.5 - 1 µm pixel size), and high resolution (nanoSIMS: 50 - 150 nm pixel size, as well as APT: 0.1 - 0.3 nm resolution in depth and 0.3 - 0.5 nm laterally).

Large element mappings were obtained using EMPA to determine the element distribution of the bone's primary elemental components (i.e., phosphorus and calcium), whose concentrations were above the quantification limit of the nanoSIMS system, as well as to pre-select representative areas for nanoSIMS analysis. The high resolution of nanoSIMS enabled displaying the distribution of isotopes in CB on a sub-micrometer scale, including small-sized histological features such as canaliculi (0.1 – 0.5 µm diameter, Reilly et al., 2001; You et al., 2004; Cardoso et al., 2013; Varga et al., 2015). An advantage of nanoSIMS over other high-resolution techniques is the possibility of analyzing larger areas by generating multiple mosaic images consisting of individual nanoSIMS maps combined with the ability to distinguish different isotope species. These chemical maps were stitched together, thus generating an element mapping comparable in size to EMP element distribution maps but at a much higher spatial resolution. APT was used to gather information in four dimensions (spatial distribution plus chemical composition) at the atomic length scale. Confocal Raman spectroscopy was applied to investigate and quantify modifications of the biogenic apatite crystal structure and the organic matrix. The approach was complemented by using high-resolution ICP-MS and isotope ratio infrared spectroscopy (IRIS) analysis for quantitative chemical and isotope analysis of the respective experimental solutions.

The first part of the study focused on the microarchitecture of bone, which is of critical importance in bone diagenesis by acting as the main pathway for the influx of fluids. The microarchitecture is thus closely related to modifications of the bone's structural components. For this reason, the first study was designed to investigate and understand whether structural and textural changes in the CB microarchitecture occur on a macro- to mesoscopic scale already shortly after exposing the CB samples to different diagenetic fluids at different temperatures. To this end, a comprehensive comparative µCT study was performed to characterize each sample qualitatively and quantitatively before and after the alteration experiments.

In the second part of this thesis, subsequent investigations of the CB samples and the corresponding experimental solutions aimed to understand and quantify the chemical and mineralogical changes on the micro- to nanometer-scale associated with the diagenetic aqueous alteration. More specifically, the aim here was to understand the early mineralization of bone and the mechanisms and kinetics of incorporating selected elements from aquatic solutions into bone.

Finally, while it is common knowledge that bone gets mineralized during the fossilization process, the origin of the material required for bone mineralization through the formation of new apatite by uptake of calcium and phosphorus is still not yet fully understood. For this reason, the experimental solutions were additionally doped with $H_2{}^{18}O$ to analyze if and under what conditions bone can be mineralized with new hydroxylapatite from calcium and phosphorus derived from the solution. Finally, one *in vitro* bone alteration experiment was performed with additional artificial sediment containing ^{18}O-labeled calcium hydrogen phosphate to address the same issue with phosphate potentially available from the sediment source. The results derived from these experiments are reported and discussed in the third part of the thesis. A more detailed model of early bone diagenesis was developed as an overarching aim.

2 Experimental aqueous alteration of cortical bone microarchitecture analyzed by quantitative micro-computed tomography

Anna G. Kral[1], Alexander Ziegler[2], Thomas Tütken[3], Thorsten Geisler[1]

[1]Institut für Geowissenschaften, Rheinische Friedrich-Wilhelms-Universität, Bonn, Germany; akral@uni-bonn.de, tgeisler@uni-bonn.de

[2]Institut für Evolutionsbiologie und Ökologie, Rheinische Friedrich-Wilhelms-Universität, Bonn, Germany; aziegler@evolution.uni-bonn.de

[3]Institut für Geowissenschaften, Johannes-Gutenberg-Universität, Mainz, Germany; tuetken@uni-mainz.de

This manuscript was published in Frontiers in Earth Science 9:609496 (https://doi.org/10.3389/feart.2021.609496). All co-authors agree to the use of the publication for the present dissertation and the presentation of the doctoral candidate's contribution.

Author contributions:

Thorsten Geisler and I conceived the study. Alexander Ziegler and I performed the µCT experiments. I conducted the alteration experiments and developed the evaluation method for quantitative 3D µCT analysis. Further analysis of the quantitative µCT data was conducted by Alexander Ziegler, Thorsten Geisler, and myself. Thomas Tütken provided literature and information on bone diagenesis. I wrote the first draft of the manuscript, while all authors contributed to data interpretation and the final manuscript.

2.1 Summary

The following paragraphs summarize the article "Experimental aqueous alteration of cortical bone microarchitecture analyzed by quantitative micro-computed tomography", published in Frontiers in Earth Science in 2021. The original publication is attached in section 2.2 Supplementary Material and can be accessed online at https://doi.org/10.3389/feart.2021.609496. This first study presents comprehensive and comparative *in vitro* bone taphonomy experiments of modern ostrich long bone samples.

Bones preserve chemical and isotopic information, which allows for reconstructing past life and environmental conditions. However, the various complex processes of bone taphonomy modify or even destroy this information. Thus, rendering a better understanding of the significance of the data stored in fossil bones is a prerequisite for future analysis. Although many alteration processes occur at the sub-micron level, it would first be essential to determine the bone microarchitecture's resistance against diagenetic changes as the microstructure controls the transport properties for mass transfer.

The present comparative study based on high-resolution X-ray micro-computed tomography (µCT) constitutes the first quantitative and time-resolved three-dimensional (3D) characterization of cortical bone (CB) experimentally altered under controlled conditions. The experiments aimed at investigating the modifications of CB samples resulting from aqueous alteration as a function of temperature, time, and composition. Furthermore, the study aimed to examine whether diagenesis-induced changes occur on a micrometer scale within a single month.

µCT is a non-invasive imaging technique applied here to characterize the microstructure of the whole CB sample volume qualitatively and quantitatively in 3D. Commonly, 3D quantitative µCT is involved in trabecular bone research, e.g., osteoporosis research, while the quantitative analysis of CB using this technique is still in its infancy. However, in this study, an evaluation method was developed that allowed trabecular bone parameters to be used to quantify CB microstructure. Both the quantitative results and the 3D visualizations proved significant in determining experimentally induced changes in CB microstructure.

For the experiments, cylindric CB samples (~3.4 mm in diameter and height) were exposed to 2 mL of artificial aqueous solutions of different compositions: seawater (SW), freshwater (FW), and 3 mL of sediment-bearing (0.5 g) freshwater (FWS) solutions. These solutions covered the range of typical natural, near-surface water compositions as close as possible.

The FW solution was enriched with U, Nd, Lu, and Sr, whereas the SW solution was only enriched with Sr and Zn. The run duration of the unbuffered and isothermal experiments varied between one and 30 days at 30, 60, and 90 °C. The first two temperatures reflect typical burial temperatures, while the 90 °C experiments aimed to accelerate the alteration processes. Experimental parameters were chosen to accelerate occurring processes and determine the possible time and temperature dependences. Before each experiment, the cylindrical CB samples were scanned using µCT to document the initial texture of the sample. After the termination of the experiments, the same samples were examined again by µCT so that experimentally induced changes could be quantified directly and be associated with changes in the controlled parameters.

The two-dimensional (2D) and 3D visualizations were helpful in systematically identifying the areas where mineralogical and chemical changes potentially occurred. The quantitative results demonstrated that the CB microarchitecture was mainly resistant to aqueous alteration and generally remained well-preserved on the macroscopic scale (≈ 3 µm), even under different experimental conditions. The most pronounced changes occurred in canals with a diameter of less than ≈ 10 µm, while canals with diameters greater than 50 µm did not experience notable changes. In addition, the response of CB microarchitecture to the alteration experiments was relatively uniform, as the observed structural modifications were not restricted to a specific area. However, differences in the extent of alteration were observed depending on the composition of the experimental solution. CB samples in FW experiments experienced the most significant modifications, SW experiments the least, and FWS experiments behaved entirely different from the two other experimental series because the solution was continuously brought back into equilibrium with the sediment during the experiments, thus keeping the solution composition relatively constant. Furthermore, a several micrometer-thick X-ray dense reaction rim that grew over reaction time was detected in experiments with FW and FWS solutions but not in samples treated in the SW solution.

Overall, it was observed that the solution composition had a more substantial impact on textural and chemical changes observed in the samples than did temperature or time. The results highlight the complexity of the interaction of different diagenetic factors. Based on these findings, investigations regarding chemical and mineralogical changes occurring on the sub-micron level during early bone diagenesis were carried out. These studies are presented in chapters 3 and 4.

2.2 Supplementary material

3 Rapid alteration of cortical bone in fresh- and seawater solutions visualized and quantified from the micro- down to the atomic scale

Anna G. Kral[1], Markus Lagos[1], Paul Guagliardo[2], Thomas Tütken[3], Thorsten Geisler[1]

[1]Institut für Geowissenschaften, Rheinische Friedrich-Wilhelms-Universität, Bonn, Germany; akral@uni-bonn.de, mlagos@uni-bonn.de, tgeisler@uni-bonn.de

[2]Centre for Microscopy, Characterization and Analysis, The University of Western Australia, Australia, paul.guagliardo@uwa.edu.au

[3]Institut für Geowissenschaften, Johannes-Gutenberg-Universität, 55128 Mainz, Germany, tuetken@uni-mainz.de

This chapter has been submitted to Chemical Geology and is currently under review.

Author contributions:

Thorsten Geisler and I conceived the study. I performed the EMPA measurements and evaluated the obtained data. Paul Guagliardo and I conducted the nanoSIMS measurements. I analyzed the collected nanoSIMS data. The Raman spectroscopic measurements were conducted by myself. Thorsten Geisler aided with data processing and evaluation. Markus Lagos helped with the ICP-MS measurements and data evaluation. Thomas Tütken, Thorsten Geisler and I discussed and interpreted the results. I wrote the first draft of the manuscript, while all authors contributed to write the final manuscript.

3.1 Abstract

It is widely known that *post mortem* diagenetic alteration processes cause modifications and overprinting of the chemical and isotopic proxies incorporated *in vivo* in bone apatite and collagen. Understanding the processes occurring during the interaction between fluids and bones in an early diagenetic setting is fundamental to determining the extent to which the commonly-used geochemical proxies in bone get modified during fossilization. The present study investigates the structural and chemical changes in bone induced by controlled *in vitro* aqueous alteration experiments and derives a deeper phenomenological and quantitative understanding of the transport and reaction processes that occur during the early stage of fossilization. For this purpose, 3.5 mm-sized cylinders were drilled from modern ostrich cortical bone and immersed in different experimental solutions enriched with tracers such as Zn, Sr, rare earth elements, and U. The experiments ran for several hours to weeks at 30, 60, and 90 °C. Both the bone samples and the experimental solutions were analyzed using micro-analytical techniques such as Raman spectroscopy, electron microprobe, high-resolution inductively coupled plasma-mass spectrometry, and nanoscale ion microprobe to assess mineralogical, chemical, and structural changes from the millimeter to the atomic scale. The results show that element uptake into the bone sample occurs already within hours after the samples have been exposed to an aqueous solution instead of years, as previously assumed. Additionally, distinct modifications of the organic phase were observed, accompanied by new apatite growth by dissolution-reprecipitation and recrystallization processes. From these data, a phenomenological model is derived that explains the interaction between bone and aqueous solutions during the earliest stages of fossilization. This study also demonstrates the importance of using a comprehensive methodological approach when investigating alteration processes whose effects range from the millimeter down to the atomic scale.

3.2 Introduction

Investigating the uptake of major, trace, and rare earth elements (REEs) in fossil bone during diagenesis and the associated changes in its original chemical and isotopic composition (Henderson et al., 1983, Williams et al., 1997) provides valuable information about *post mortem* environmental conditions and processes (e.g., Wang & Cerling, 1994; Nielsen-Marsh & Hedges; 2000, Trueman & Tuross, 2002; Pucéat et al., 2004; Trueman et al., 2008;

Herwartz et al., 2013a; Reynard & Balter, 2014; Tacail et al., 2020). Bones are mineralized tissues composed of meta-stable nano-crystalline bioapatite, collagenous proteins, and water (Glimcher et al., 2006; Boskey & Robey, 2013; Grandfield et al., 2018; Reznikov et al., 2018). Bioapatite, the main constituent of bone, is a calcium phosphate mineral ($Ca_{10-x}[(PO_4)_{6-x}(CO_3)_x]\ (OH)_{2-x}\cdot nH_2O$, Pasteris et al., 2014) that can incorporate a large number of elements and molecules. On the one hand, this property renders bioapatite a valuable source of chemical and isotopic information for reconstructing, for example, ancient and modern climate and living conditions (e.g., Longinelli, 1984; Hedges et al., 2004; Levin et al., 2006), diet (e.g., DeNiro & Epstein, 1978, 1981; Schoeninger & DeNiro, 1984; Wang & Cerling, 1994; Fogel & Tuross, 2003; Scott & Poulson, 2012; Jaouen et al., 2013; Davis & Munoz, 2016; Bourgon et al., 2020), or provenance and migration patterns (e.g., Ericson, 1985; Hoppe et al., 1999; Beard and Johnson, 2000; Taylor et al., 2019; Guiry et al., 2020; Kowalik et al., 2020; Monti et al., 2021). However, on the other hand, the same properties and its nano-crystalline nature make bioapatite prone to *post mortem* diagenetic alteration induced by changes in the physical and chemical environment. For example, pseudomorphic replacement of bioapatite can lead to modifications and overprinting of the bone's *in vivo* chemical and isotopic composition, while the original morphology may still be preserved (Kolodny et al., 1996; Pasteris & Ding, 2009). The ability to retain its fine-scale morphology during a mineral replacement process was demonstrated, for instance, by an experimental study by Kasioptas et al. (2010). They experimentally replaced the filigree, micrometer-sized, chamber-like architecture of squid cuttlebone (*Sepia officinalis* Linnaeus, 1758), made of aragonite, in aqueous solutions with hydroxyapatite (and a small amount of ß-tricalcium phosphate). Therefore, the need arises to differentiate between chemical and isotopic information incorporated *in vivo* versus that information altered by *post mortem* taphonomic processes. *Post mortem* modifications depend on the diagenetic environment (e.g., Kohn et al., 1999; Collins et al., 2002; Hedges, 2002; Jahns, 2008; Karr & Outram, 2012; Matthiesen et al., 2021) but also on the susceptibility of individual elements for diagenetic mobilization (Martin et al., 2017 and references therein). Thus, a thorough understanding of how the chemical and isotopic composition of bones can be affected in different diagenetic settings by the alteration processes already shortly after the death of the individuum is essential.

A variety of studies have systematically investigated the effect of diagenesis on the chemical and isotopic composition in bones and teeth (e.g., De Niro, 1985; Nelson et al., 1986; Zazzo et al., 2004; Trueman et al., 2004; Sponheimer & Lee-Thorp, 2006; Fricke et al., 2008; Hinz

& Kohn, 2010; Herwartz et al., 2011; Heuser et al., 2011; Tütken & Vennemann, 2011; Tütken et al., 2011; Trueman, 2013; Tütken, 2014; Bourgon et al., 2020; Suarez & Kohn, 2020). Most of these studies focused on diagenetically altered archeological or fossilized bones, while systematic alteration experiments using modern bones or teeth covering the first days to years after death are scarce. Long-term burial experiments in wetland soils with modern alligator bones performed by Keenan & Engel (2017) showed that compositional alteration and distinct bioerosion were monitored already after one week. In mesocosm experiments, microbial colonization was inhibited, and transformation from bioapatite to a more stable apatite phase was observed already after one month. Kohn & Moses (2013) conducted aqueous alteration experiments on bones to determine experimentally induced diffusion coefficients at 20 °C for numerous trace elements, including Sr, Zn, U, and REEs. This study showed that common charge-coupled element species limited the diffusion rate in bone and lead to similarities in diffusion rates. Consequently, trace element profiles in fossilized bone were unlikely to be caused by intra-bone volume diffusion as formerly assumed, are presumably the result of recrystallization and transport limitations. Moreover, aqueous alteration experiments, in which calcined bone and tooth enamel were exposed to ^{87}Sr-doped solutions for one year, showed that the ability to incorporate Sr into the apatite crystal lattice is considerably smaller for bones or teeth with high apatite crystallinity (Snoeck et al., 2015). Another controlled alteration study with modern bone in aqueous NaF solution at pH 9-10 for up to three weeks at maximum temperatures of 70 °C was performed by Aufort et al. (2019a). The authors proposed a transformation mechanism that involves the partial dissolution of bioapatite and reprecipitation of secondary apatite, which occurs irrespective of the presence or absence of F, thus leading to the formation of carbonate-bearing fluorapatite (FAp) and/or hydroxylapatite (HAp), respectively. Furthermore, recently a comprehensive time-resolved aqueous alteration study on modern elephant tooth pieces was performed under controlled conditions representing an extreme acidic early diagenetic environment (Weber et al., 2021). This study showed that the Ca, Sr, Zn, and Mg isotope compositions in dentine are strongly affected by diagenetic alteration. In contrast, only the outermost 100-300 µm were affected by alteration in enamel, while the central part of the mm-thick enamel remained unaltered.

Kral et al. (2021; chapter 2) used a similar experimental approach in an *in vitro* aqueous alteration study on modern ostrich cortical bone (CB) mimicking natural aquatic early diagenetic conditions to study their effect on CB microarchitecture. The CB samples were experimentally altered in fresh- and seawater-like solutions (FW and SW, respectively) at different temperatures (30 to 90 °C). This study showed that the CB microarchitecture remained mainly resistant to aqueous alteration on a microscopic scale. However, in CB samples altered in FW solutions, an unevenly distributed reaction rim (RR) was detected within the outermost layer, demonstrating a strong influence of the solution chemistry on the alteration.

The results of the present study expand on and complement the results obtained by Kral et al. (2021; chapter 2) through analysis of the same altered cylindric bone samples using various micro-analytical techniques. Micro-computed tomography (µCT) images of the reacted CB samples were used to define the areas of interest (such as the RRs), which were then further investigated by electron microprobe analysis (EMPA) chemical imaging, which, in turn, delivered the basis for selecting samples and sample areas of interest for nanoscale secondary ion mass spectrometry (nanoSIMS) element mapping at the sub-µm resolution, which has so far not been applied to investigate modern or fossilized bone. These bone tissue data were supplemented with quantitative analyses of the initial and final solutions of the respective *in vitro* alteration experiments using high-resolution inductively coupled plasma mass spectrometry (HR ICP-MS). In addition, confocal Raman spectroscopy was used to investigate potential alteration effects on the organic and inorganic components of the CB samples. Finally, atom probe tomography (APT) was applied to visualize and quantify changes in element distribution in three dimensions (3D) from the millimeter down to the atomic scale. With this approach, the study aimed to gain more insights into the interaction between CB and aqueous fluids and derive a more detailed phenomenological and quantitative understanding of the transport and reaction processes active in the early stage of fossilization or bone degradation.

3.3 Materials and methods

3.3.1 Experimental setup

All experimental run products analyzed here originated from *in vitro* aqueous alteration experiments of a recently conducted study to assess changes in bone microstructure (Kral et al., 2021; chapter 2) – the reader is referred to this article for detailed information on the CB samples and the experimental setup. Briefly, the cylindric CB samples (Fig. 3.1A) were drilled (3.5 mm x 3.5 mm cores) from the bone cortex of a tibia from a modern ostrich (*Struthio camelus* Linnaeus, 1758) and then exposed to three types of aqueous solutions by putting one CB sample and 2 mL of a solution into sealed 3 mL Teflon vials and letting them react for up to 30 d at 30, 60, and 90 °C. The more elevated temperatures of 60 and 90 °C were applied to accelerate the reaction and transport processes (Dobberstein et al., 2009; Abdel-Maksoud, 2010; Turner-Walker, 2011).

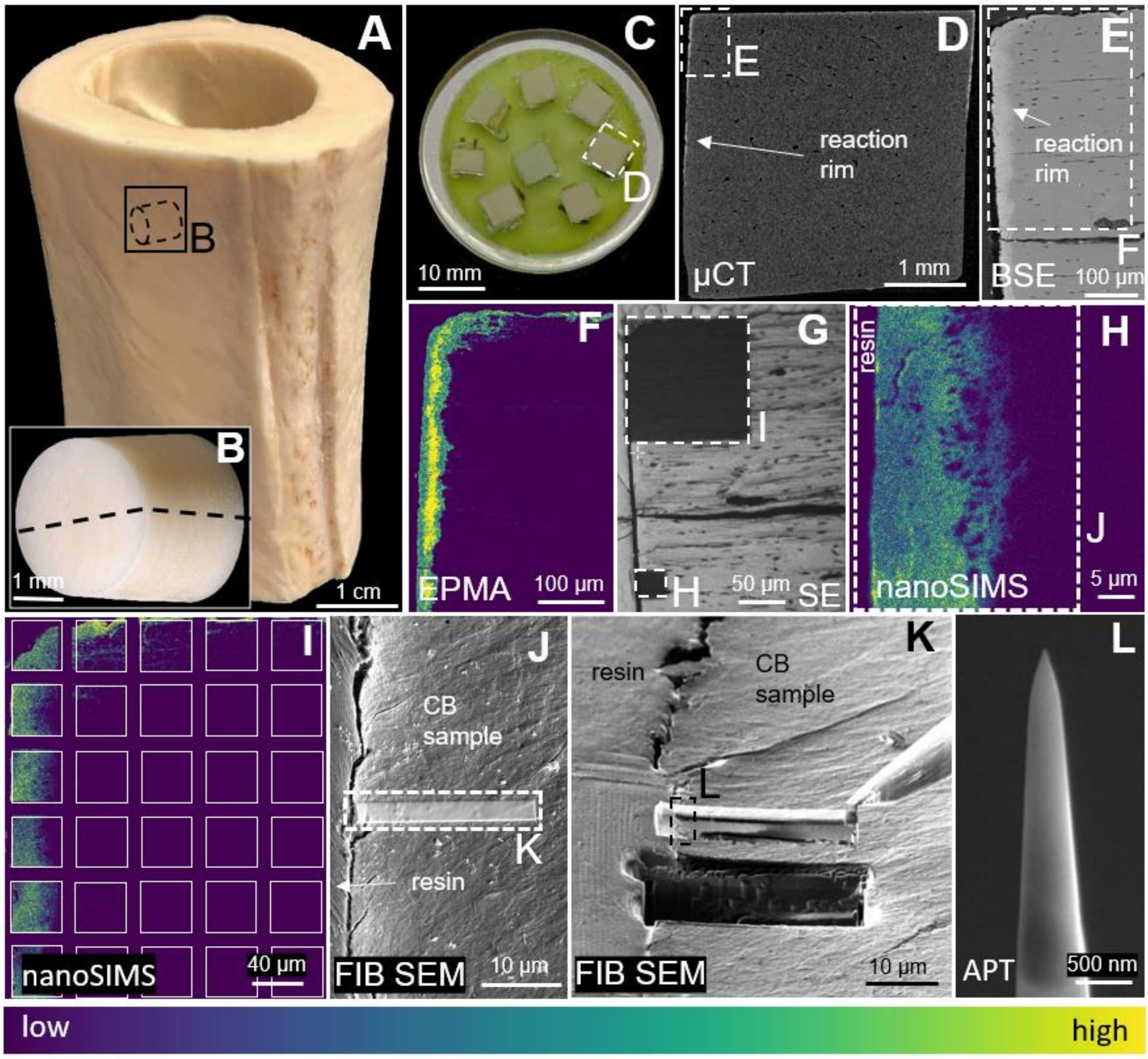

Figure 3.1 | Methodological overview of chemical analysis of *in vitro* altered bone at different spatial scales. **(A)** The cortex of the diaphyseal part of the analyzed modern ostrich tibia. **(B)** Cylindric CB drill core sample with dashed lines indicating the cutting plane. **(C)** Representative mount with polished samples embedded in Technovit© resin. **(D)** Representative µCT section illustrating the bright RR and the selected area for EMPA and nanoSIMS. **(E)** Backscattered electron (BSE) image with the dashed lines marking the area chosen for electron microprobe analyses (EMPA). **(F)** Color-coded EMPA images displaying the U distribution. **(G)** Secondary electron (SE) image showing the localities of **(H)** a single nanoSIMS map and of **(I)** a mosaic image consisting of 30 individual nanoSIMS maps, both display the spatial distribution of U. **(J)** SE image of the area perpendicular to the sample's edge that was selected for APT and covered with platinum. **(K)** Extraction of an APT wedge that was later cut into five sections and **(L)** prepared in the form of a needle. The uniformly-scaled Viridis palette was used for color-coding the images.

Only CB samples derived from two of the three experimental series were further investigated in the present study. These solutions had either a FW composition, isotopically labeled with depleted U and enriched with Nd and Lu or a SW composition, enriched with Zn only (see Table 3.1 for details). These two solutions were used as model analogs of the most abundant types of aqueous solutions on Earth in which bones typically fossilize. The elements of particular interest were B, F, Mg, P, Ca, Zn, Sr, Nd, Lu, and U, all commonly used to reconstruct the paleoecology or taphonomy of vertebrates.

Table 3.1 | Element concentrations of freshwater (FW) and seawater (SW) stock solutions in ppm.

Cation/anion	**FW**	**SW**
B^{3+}	2.34 ± 0.06	3.15 ± 0.07
Na^{+}	*100.0 ± 0.2*	*10,770 ± 22*
K^{-}	*100.0 ± 0.2*	*390.0 ± 0.8*
Ca^{2+}	1,426 ± 15	562 ± 6
Cl^{-}	*775 ± 2*	*19,350 ± 39*
Mg^{2+}	122.0 ± 1.4	859.2 ± 1.7
F^{-}	*5.00 ± 0.01*	*5.00 ± 0.01*
Sr^{2+}	137.6 ± 0.9	140.1 ± 1.9
Zn^{2+}		9.6 ± 0.5
Lu^{3+}	3.51 ± 0.01	
Nd^{3+}	1.754 ± 0.003	
U^{6+}	16.0 ± 0.2	

The composition of the stock solution constituents B, Ca, Mg, Sr, Zn, Fe, Lu, Nd, and U [ppm ± SD] was determined using a Thermo Scientific Element XR. For the remaining constituents, the concentration was calculated from the weight-in and is given in italic font [ppm ± 0.2 %]. The weighted substances contained in both types of solution were B_2O_3, $NaHCO_3$, NaF, KCl, $CaCl_2$, $MgCl_2$, and $SrCl_2$, while the FW solution solely had $FeCl_3$, $NdCl_3$, $LuCl_3$, and $UO_2(NO_3)_2$ and the SW solution NaCl, Na_2SO_4, $Ca(NO_3)_2$, and $ZnCl_2$.

For instance: δ^{26}Mg (Martin et al., 2015), δ^{44}Ca (e.g., Heuser et al., 2011; Tacail et al., 2020), δ^{66}Zn (e.g., Jaouen et al., 2016a, b; Bourgon et al., 2020) and $\delta^{86/88}$Sr (Knudson et al., 2010; Lewis et al., 2017) have been used for the reconstruction of the trophic level and food webs, while ^{87}Sr/^{86}Sr was used to determine habitat use and migration patterns (e.g., Hoppe et al., 1999). REE, here represented by Nd as a light REE and Lu as a heavy REE, are important diagenetic proxies for the taphonomic setting and stratigraphic provenance (Trueman et al., 2006) as well as for early diagenetic alteration of bone (Trueman et al., 2004). Lutetium and the trace element U in fossil bones can both be used for radiometric dating using Lu-Hf (Kocsis et al., 2010; Herwartz et al., 2011), U-Th (Grün, 2006; McGregor et al., 2011; Grün et al., 2014), or U-Pb isotope analysis (Romer, 2001; Tomaschek et al., 2008; Ludwig et al., 2012). However, U-Pb only works with limited success. Additionally, U enables differentiating diagenetically altered from unaltered areas in bone (Grimstead et al., 2018). In bone health research, B has been of interest for decades, as it positively influences the bone metabolism and, in particular, bone growth and strength by preferentially binding to substances with hydroxyl groups like hydroxylapatite or the biomolecule collagen I (Chapin et al., 1997; Nielsen, 2014; Dessordi & Navarro, 2017; Rondanelli et al., 2020 and references therein). Finally, F plays an essential role in the preservation of hard tissues during diagenesis by substituting the hydroxyl-ions in the apatite lattice, thereby leading to greater stability (lower aqueous solubility) of the apatite phase (e.g., Kolodny et al., 1996; Truemann & Tuross, 2002; Pasteris & Ding, 2009; Aufort et al., 2019a).

3.3.2 Electron microprobe analysis

EMPA was performed using a JXA 8200 Superprobe (JEOL Ltd., Tokyo, Japan) with five wavelength-dispersive spectrometers and an energy-dispersive X-ray, a backscatter, and a cathodoluminescence detector. The polished sample mounts were coated with ≈ 20 nm of carbon. Suitable areas for analysis were selected based on µCT images acquired during sample pre-characterization (Fig. 3.1D). X-ray backscattered electron (BSE) images (Fig. 3.1E) and qualitative element distribution images with a point-by-point step size of 1 µm (Fig. 3.1F) were taken from an unaltered CB sample as well as from altered samples representative for the different solutions and reaction temperatures. For each BSE image, contrast and brightness were adjusted to achieve the maximum information about bone density changes. Therefore, comparisons of the greyscale levels between the images are only conditionally possible. The acceleration voltage was set to 15 keV at 15 nA beam current. Peak and background counting times were 10 s for all elements except Na (5 s). The Kα-lines were used for F, Na, Mg, P, Cl, Ca, and Zn analysis, whereas the Mα line was used for U and the Lα line for Sr and the REEs Nd and Lu. The standards used for calibration were magmatic fluorapatite for P and Ca, magnesium oxide for Mg, and natural uraninite for U. Smithsonian microbeam references NMNH 133868 (anorthoclase; Jarosewich et al., 1980) and NMNH 10065 (strontianite; Jarosewich & White, 1987) were used for Na and Sr calibration, respectively. The REE orthophosphate $NdPO_4$ (USNM 168492) and $LuPO_4$

(USNM 168491) reference samples were used as standards for Nd and Lu quantification (Jarosewich & Boatner, 1991; Donovan et al., 2003). The ZAF matrix corrections were applied to correct peak intensities for backscattered electron loss, absorption, and secondary fluorescence effects (Philibert & Tixier, 1968; Goldstein et al., 1992).

3.3.3 Nanoscale secondary ion mass spectrometry

The nanoSIMS 50L system (Cameca, Gennevilliers, France) was used for qualitative elemental analysis. Mounts were coated with 10 nm of Au before analysis. Secondary electron (SE) imaging was used to locate target areas (Fig. 3.1G), previously determined using EMPA qualitative imaging. Before element mapping, fields of view between 45 µm and 60 µm edge length were pre-sputtered using a current of 1 nA for 10 min. The element distribution maps obtained for B, F, Na, Mg, P, Ca, Zn, Sr, Nd, Lu, and U were displayed either as single nanoSIMS maps - each 40 x 40 µm^2 in size with 512 x 512 px in the sub-µm scale (Fig. 3.1H) - or as mosaic image consisting of a series of single nanoSIMS maps covering larger areas (Fig. 3.1I). Mappings acquired using a Cs^+ primary ion beam were located directly beside the previous maps scanned using an O^- ion beam to avoid charging effects and potential oxygen contamination caused by the ion beam. For imaging, the focused 16 keV Cs^+ primary ion beam with a lateral resolution of approximately 100 nm rastered a defined surface area to generate the negative ions $^{16}O^-$, $^{18}O^-$, $^{19}F^-$, $^{24}C^-$ ($^{12}C_2$), $^{26}N^-$ ($^{12}C^{14}N$), and $^{35}Cl^-$, while the O^- primary ion beam with a lateral resolution of approximately 200 nm was used to generate the positive ions $^{11}B^+$, $^{23}Na^+$, $^{24}Mg^+$, $^{31}P^+$, $^{40}Ca^+$, $^{67}Zn^+$, $^{88}Sr^+$, $^{142}Nd^+$, $^{175}Lu^+$, and $^{238}U^{16}O^+$. Seven different ion species were simultaneously detected. An electrostatic and a magnetic sector were used to collect and detect the secondary ions. The O^- beam current was set to 50 pA, whereas the Cs^+ beam current was set to 4-5 pA - the eGun was used with the latter. Dwell times varied from 2.5 to 5 ms per pixel, and multiple planes were recorded for each image. The obtained images were processed, and large mosaic images were constructed using the software Fiji v1.53c with the plugins OpenMIMS (http://nano.bwh.havard.edu) and NRRD Mosaics (https://github.com/BWHCNI/OpenMIMS.wiki.git).

3.3.4 Atom probe tomography

Elemental and isotopic 3D compositional analyses were performed on the near-atomic scale on three representative CB samples using a CAMECA LEAP 4000X HR APT. To extract small sample volumes, an area of 2 µm x 20 µm traversing the RR was sputtered with Pt (Fig. 3.1J) using a TESCAN Lycra3 Ga^+ focused ion beam SEM (Rickard et al., 2020). The sputtered area was cut to a rectangular prism and removed using the *in situ* lift-out technique described by Thomson et al. (2007) (Fig. 3.1K). Each prism was cut into up to 10 segments, with every segment being mounted on a post on pre-fabricated coupons and finally shaped needle-like by the ion beam (Fig. 3.1L). Detailed information on data acquisition and image reconstruction is provided elsewhere (Reddy et al., 2020).

3.3.5 Raman spectroscopy

Raman measurements were performed with a LabRam HR800 system (Horiba Scientific, France) equipped with a BX41 microscope (Olympus America Inc., Center Valley, PA, USA). Spectra were collected from CB samples (n = 6) treated for 30 d in FW and SW solutions at 30, 60, or 90 °C. For excitation of Raman scattering, a 200-mW diode-pumped solid-state laser (783.976 nm) was used, but only about 10 % laser power reached the sample surface. The measurements were performed using a 100x objective with a numerical aperture of 0.9 and a confocal hole of 1,000 µm. Before collection using an electron-multiplier charge-coupled device (CCD) detector, the scattered Raman light passed through a 100 µm spectrometer entrance slit and was dispersed by a 600 grooves/mm grating. With these settings, the theoretical, diffraction-limited lateral and axial resolution was about 1 µm and less than 2 µm, respectively. At the beginning of each measurement session, the spectrometer was calibrated with the first-order band of a pure silicon standard at 520.7 cm^{-1}. Additionally, to correct for shifts during long-term analysis, the 886.19 cm^{-1} line of the laboratory room's ceiling light was used as an internal standard. The wavelength of this line was determined beforehand using the 985.43 cm^{-1} line of a neon lamp for which the wavelength is precisely known (Saloman & Craig, 2006). From the width of both lines, a spectral resolution of 1.94 ± 0.02 cm^{-1} was determined, which was used to correct the width of the Raman bands for finite slit width effects (Tanabe & Hiraishi, 1980). The analyses were performed along the sample's edge in the frequency range of 150-2,000 cm^{-1} with an acquisition time of 20 s, two accumulations per spectrum, and a step size of 1 µm. The area covered by each analysis was slightly different depending on the individual sample structure. 41 single analyses were performed parallel to each sample's edge, while the number of analyses perpendicular to the edge varied between 26 and 45. Due to the natural heterogeneity of the CB samples and for direct comparison, spectra were also taken from multiple areas in the presumably unaltered center of each sample. From all spectra, the parameters 'full width at half maximum' (FWHM) and the position of the $\nu_1(PO_4)$ fully symmetrical stretching band of apatite near 960 cm^{-1} were extracted by least-squares fitting. The $\nu_1(PO_4)$ band was fitted with an asymmetrical Gauss-Lorentz function to account for an asymmetry towards the low-frequency side observed in some bone apatite spectra. The procedure and reasoning have previously been described and discussed in more detail in Barthel et al. (2020), Geisler & Menneken (2021), and Weber et al. (2021).

3.3.6 High-resolution inductively coupled plasma-mass spectrometry

Concentrations of B, Mg, P, Ca, Zn, Sr, Nd, Lu, and U were determined by multi-element analyses of the experimental solutions using an Element 2/XR Sector Field ICP-MS system (Thermo Fisher Scientific, Waltham, MA, USA) equipped with a dual-mode secondary electron multiplier (counting and analog mode) combined with a Faraday detector. The three different detection modes allowed for a linear detection range over several orders of magnitude, which enabled analysis of the different experimental solutions with their strongly varying chemical and isotopic concentrations ranging from a few thousand ppm down to the ppt level. Every sequence started by rinsing the system using 2 % HNO_3, followed by a) measuring five 2 % HNO_3 blank solutions, b) the calibration solutions (using a 5-point linear calibration based on several dilutions of the multi-element standard solution Merck Certipur VI), c) several certified reference materials (SPS-SW2, SLRS-6, TM-26.4) which were used to validate the calibrations and finally d) the sample solutions. After every tenth sample solution, a blank solution was analyzed for background correction. Before measuring each new sample, the sample introduction system was rinsed with 2 % or 5 %-HNO_3 for at least 2 min or until an appropriate background level was reached. The mean (n = 2), the standard deviation, and the relative standard deviation were calculated for each sample. Furthermore, the detection limit was determined and used to correct the results, which were also checked for plausibility. For analysis, aliquots were taken from all experimental solutions (n = 30), the stock solutions (n = 2) and from the experimental blanks (n = 3). Before diluting the experimental solutions, all aliquots were centrifuged for 10 min at 13 rpm to ensure that potential suspended matter had settled. The final dilution factor was determined via pre-scans and varied between 5-fold and 300,000-fold. 1 ppb of ^{103}Rh was added to all aliquots as an internal standard to correct short-term instrumental drifts. In addition, potential long-term instrumental drift was also investigated and corrected if necessary. This was done by repeatedly analyzing the calibration solutions throughout the analytical sequence. Details about the analyzed isotopes and the applied resolution modes are given in Table 3.2. Measurements in medium resolution (MR) mode (mass resolution of 4,000) were generally conducted to avoid signal contributions from potential polyatomic interfering species. Regarding elements (B, Mg, Zn, and Nd) that are often prone to interfering species, the signal intensities of two different isotopes were recorded and compared. In the case of Mg, Zn, and Nd, results of both signal intensities agree within uncertainty, and the mean of both was used for evaluation. For B, however, only signal intensities of ^{10}B were evaluated because ^{11}B gave higher intensities throughout presumably due to severe interference from ^{23}Na^{2+}, which was also present in the sample solutions. Lu, for instance, was analyzed in low (LR) as well as in MR mode. Both results agreed within uncertainty, but the LR signal intensities were used for further evaluation because of higher precision and lower detection limits.

Table 3.2 | Overview of the analyzed isotopes and the applied mass resolution for the elements of interest (B, Mg, Ca, Zn, Sr, Nd, Lu, and U).

Element	Isotopes	Mode
B	^{10,11}B	MR
Mg	^{25,26}Mg	MR
P	^{31}P	MR
Ca	^{43}Ca	MR
Zn	^{66,68}Zn	MR
Sr	^{88}Sr	LR
Nd	^{143,146}Nd	MR
Lu	^{175}Lu	MR, LR
U	^{238}U	LR

LR = low resolution, MR = medium resolution

3.4 Results

3.4.1 Textural alteration

BSE images revealed an intact microstructure in pristine CB samples with few microcracks (MCs) in the interstitial bone and only slight differences in greyscale intensities. The interstitial bone appeared slightly brighter than the osteonal bone (Fig. 3.2A) due to its higher degree of bioapatite content and/or variations in nanoscale porosity. After the experiments, the intact CB was pervaded by experimentally induced MCs, which were already observed after 1 d, irrespective of the applied temperature or solution composition (Fig. 3.2B, C). The MCs were only partially visible in the µCT sections due to the lower resolution of these scans (Fig. S3.1). The appearance of the MCs differed depending on the orientation of the CB sample during cutting.

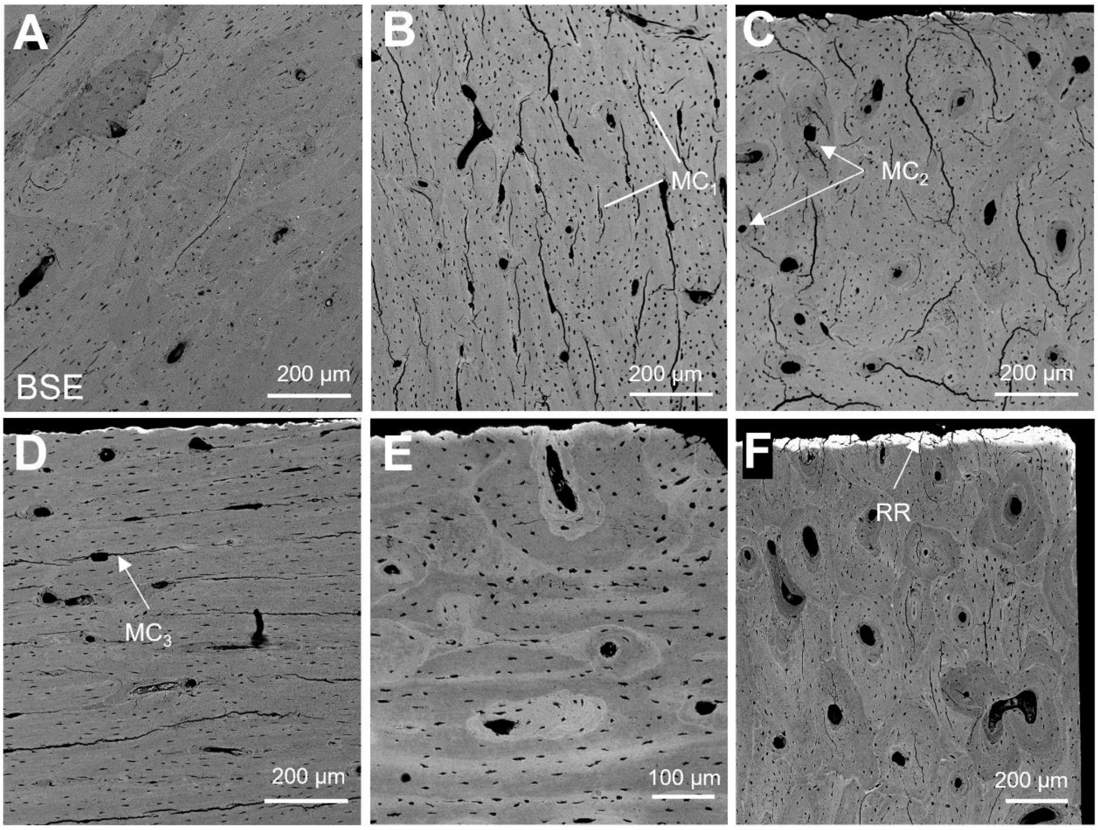

Figure 3.2 | Series of representative BSE images of cross-sections of CB. **(A)** pristine and **(B - F)** altered CB samples. Altered CB samples showed experimentally induced MCs of **(B)** type 1 (1 d at 30 °C in SW), **(C)** type 2 (1 d at 30 °C in FW), and **(D)** type 3 (7 d at 90 °C in FW). See text for details. **(E)** CB sample without MCs (30 d at 90 °C in FW). **(F)** CB sample with a pronounced RR (3 d at 30 °C in FW).

In samples cut perpendicular to the longitudinal growth direction, MCs appeared relatively short in length (≈10 to 200 µm) and unconnected, and predominantly originated in the interstitial bone without any preferential orientation (MC_1 in Fig. 3.2B). MCs were also found within osteons, either entirely restricted to the osteon or connected with the interstitial bone, whereby the cement line was crossed (MC_2 in Fig. 3.2C) - no preferred orientation was observed for this type of MC either. In CB samples cut along the Haversian canals, MCs were primarily located in the interstitial bone but did connect with an osteon at one or both sides. Moreover, these MCs were oriented parallel to each other and reached lengths of up to several 100 µm (MC_3 in Fig. 3.2D). A tendency toward stronger greyscale variations, e.g., in osteonal bone, and a reduction in the number and length of MCs was observed with increasing temperature and experimental duration (Fig. 3.2E). It was also found that CB samples immersed in FW solutions showed a bright (i.e., higher density), unevenly distributed area along the edges of the CB samples with a thickness of up to 20 µm (Fig. 3.2F), which was already described and referred to as the RR (Kral et al., 2021; chapter 2).

3.4.2 Chemical alteration

3.4.2.1 Micrometer-scale observations

Qualitative EMPA element distribution maps obtained from pristine CB samples revealed slightly unevenly distributed P (Fig. 3.3A) and Ca (Fig. 3.3B) at the micrometer scale. Mg (Fig. 3.3C), Na (Fig. 3.3D), and Sr (Fig. 3.3E) were evenly distributed, albeit close to the detection limit (0.01, 0.02, and 0.03 wt.%, respectively). Element concentrations of Zn, Nd, Lu, and U were generally below the detection limit (0.05, 0.02, 0.07, and 0.02 wt.%, respectively). CB samples experimentally altered in FW solutions at 60 °C were depleted in P, Ca, and Mg in the RR to a varying extent but relatively enriched further inside the sample (Fig. 3.3F, G, H, respectively). The spatial distribution of Na (Fig. 3.3I) did not differ significantly from that in pristine CB, irrespective of the experimental solution to which the CB was exposed. Furthermore, in CB samples derived from FW experiments, Sr (Fig. 3.3J), Nd (Fig. 3.3K), Lu (Fig. 3.3L), and U (Fig. 3.3M) were concentrated within the rim area to varying extent. Under 90 °C, these distribution patterns did not change notably, except for Ca, which was enriched along the sample's edge (Fig. 3.3N). CB samples that reacted in SW solutions at 60 and 90 °C showed element distributions comparable to the FW sample, except for Mg and Zn. Magnesium was not significantly changed in its distribution, whereas Zn (Fig. 3.3O) appears to have been enriched along the edge of the sample. Note that Nd, Lu, and U were not included in the SW solution.

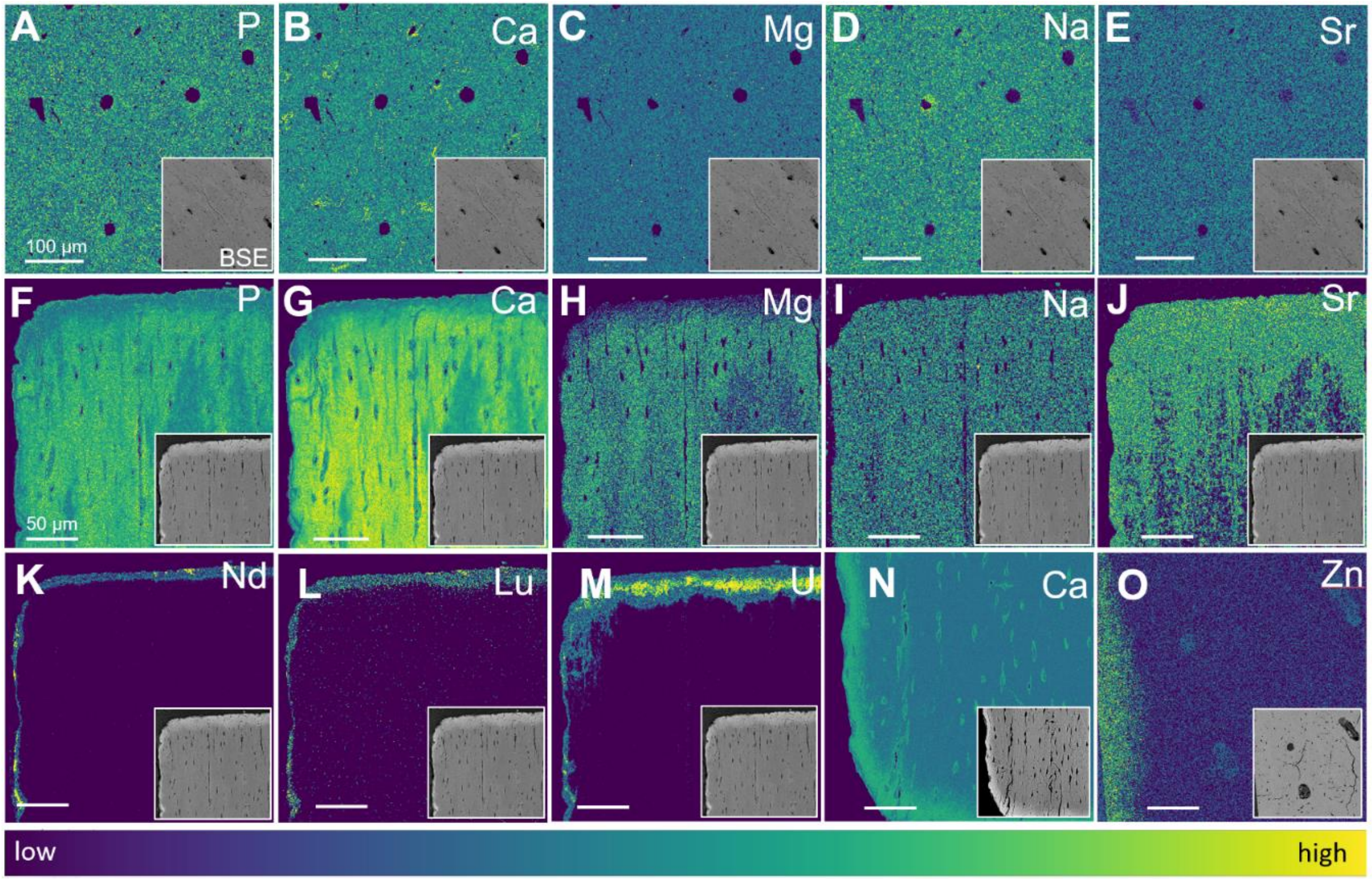

Figure 3.3 | EMPA element distribution maps of pristine and altered CB. Images **A-E** show pristine and images **F-O** altered CB (30 d at 60 or 90 °C) with inset maps representing BSE images with an edge length of 300 µm. **(A-E)** Distribution of P, Ca, Mg, Na, and Sr in unaltered CB, respectively. Images **F-M** display the P, Ca, Mg, Na, Sr, Nd, Lu, and U distribution, respectively, in samples reacted in FW at 60 °C. Similar distributions were observed in samples derived from SW experiments, except for Nd, Lu, and U. Image **N** is representative of the Ca distribution in samples reacted at 90 °C in FW and SW. **(O)** Zn distribution in a sample exposed to SW (FW solutions did not contain Zn). Images **A-E** and **F-O** have the same scale bar of 100 µm and 50 µm, respectively.

3.4.2.2 Nanometer-scale observations

To supplement the EMPA element distribution images with chemical/isotopic images of higher resolution, nanoSIMS imaging was used for the first time to chemically and isotopically characterize experimentally altered CB samples at the nanometer scale. In CB samples from both experimental series (FW, SW), the highest intensities of F were measured in the outermost 20 µm of the samples (Fig. 3.4A, B, respectively). The area enriched with F is sharply limited in the CB sample reacted in the FW solution. In contrast, the SW CB sample showed a gradient with decreasing intensities towards the sample center.

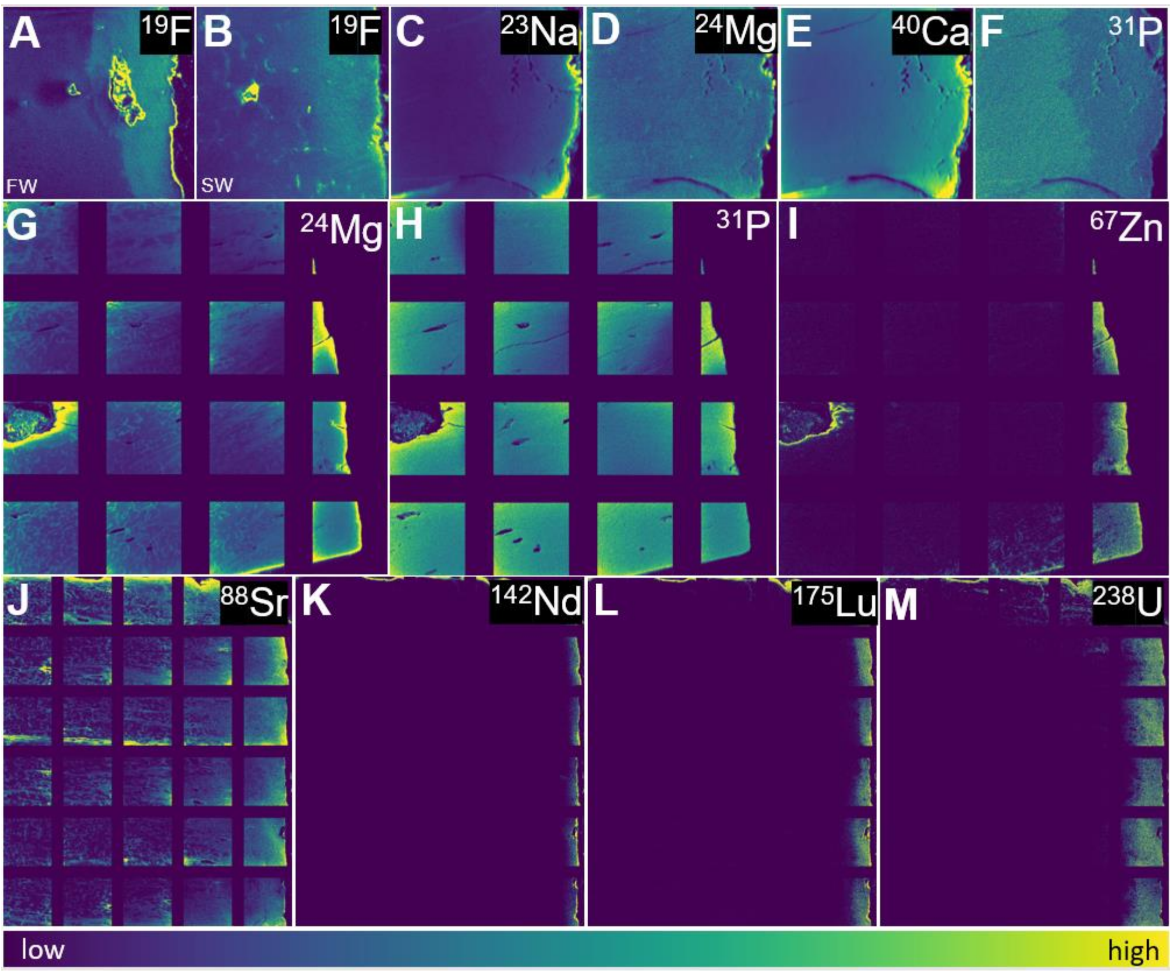

Figure 3.4 | Isotope distribution images obtained by nanoSIMS of representative CB samples. **(A)** and **(B)** show the distribution of ^{19}F in a FW and a SW sample, respectively. Both samples reacted at 90 °C for 30 d. The CB sample exposed to FW for 30 d at 60 °C was chosen to show the distribution of **(C)** ^{23}Na, **(D)** ^{24}Mg, **(E)** ^{40}Ca, and **(F)** ^{31}P. The mosaic images, consisting of 16 and 30 individual maps, show the **(G)** ^{24}Mg, **(H)** ^{31}P, and **(I)** ^{63}Zn distribution and were taken from a sample that was reacted at 60 °C for 30 d in the SW solution. The last four mosaic images show the **(J)** ^{88}Sr, **(K)** ^{142}Nd, **(L)** ^{175}Lu, and **(M)** ^{238}U distribution in a representative CB sample reacted at 60 °C for 30 d in the FW experimental series (doped with Nd, Lu, and U). The size of a single image is 40 x 40 µm².

Single element distribution maps showed that Na (Fig. 3.4C) and Mg (Fig. 3.4D) were homogeneously distributed in all samples and only slightly enriched in the RR. However, the Na element maps contrast with the EMPA results, which do not show any modifications in Na distribution, but this is most likely due to the lower sensitivity of EMPA (Fig. 3.3E). A mosaic image consisting of 16 single element maps from an SW sample revealed that Mg is enriched in the RR and penetrated at least 300 µm deep into CB via the cortical canal network (CCN), which is reflected by a higher Mg content around the canaliculi. In contrast, the interstitial bone is less enriched with Mg (Fig. 3.4G). The altered CB samples were washed with MilliQ water several times before analysis. It was impossible to distinguish between CCN and the interstitial CB material in the RR because the interstitial bone was also enriched with Mg, thus leading to a homogenous distribution within that area.

Calcium was found to be uniformly distributed in all samples. A slight increase in Ca was observed along the RR, the MCs, and porous structures (Fig. 3.4E). This observation again contrasts with the EMPA results (Fig. 3.3G). However, this can be explained by the lower sensitivity of nanoSIMS for Ca concentration. A significant depletion in P was observed within the RR (Fig. 3.4F), which correlates well with the EMPA results (Fig. 3.3F). In contrast, SW samples showed higher P contents along the margin and larger pores (Fig. 3.4H). A distinct and uniform enrichment with Sr was determined along and exceeding the RR (Fig. 3.4J), irrespective of the type of solution. Further away from the edge of the samples, Sr was still detectable, but only directly surrounding the CCN and barely present in the interstitial bone. However, the same applies to Zn, although to a lesser extent (Fig. 3.4I).

Most intriguingly, the elements Nd, Lu, and U (exclusively added to the aqueous solution of the FW experiments) were highly enriched along the edges of all FW samples, marking the RR. Mosaic images of Nd (Fig. 3.4K), Lu (Fig. 3.4L), and U (Fig. 3.4M), consisting of 30 individual nanoSIMS maps, revealed an increase in the penetration depth with increasing atomic number, i.e., 92 (U) > 71 (Lu) > 60 (Nd). However, the incorporation of U was thereby not restricted to the RR, i.e., U was transported further into the CB, comparable to Mg, Zn, and Sr, although the enrichment is less pronounced or detectable. In general, two different distribution patterns were observed: (1) a uniform change in element concentration in the RR, irrespective of histological features (Fig. 3.4A), and (2) some elements further penetrated deeper into the CB via the CCN, which is evident by higher element contents predominantly at the CB–solution–interface in cortical canals (Fig. 3.4J).

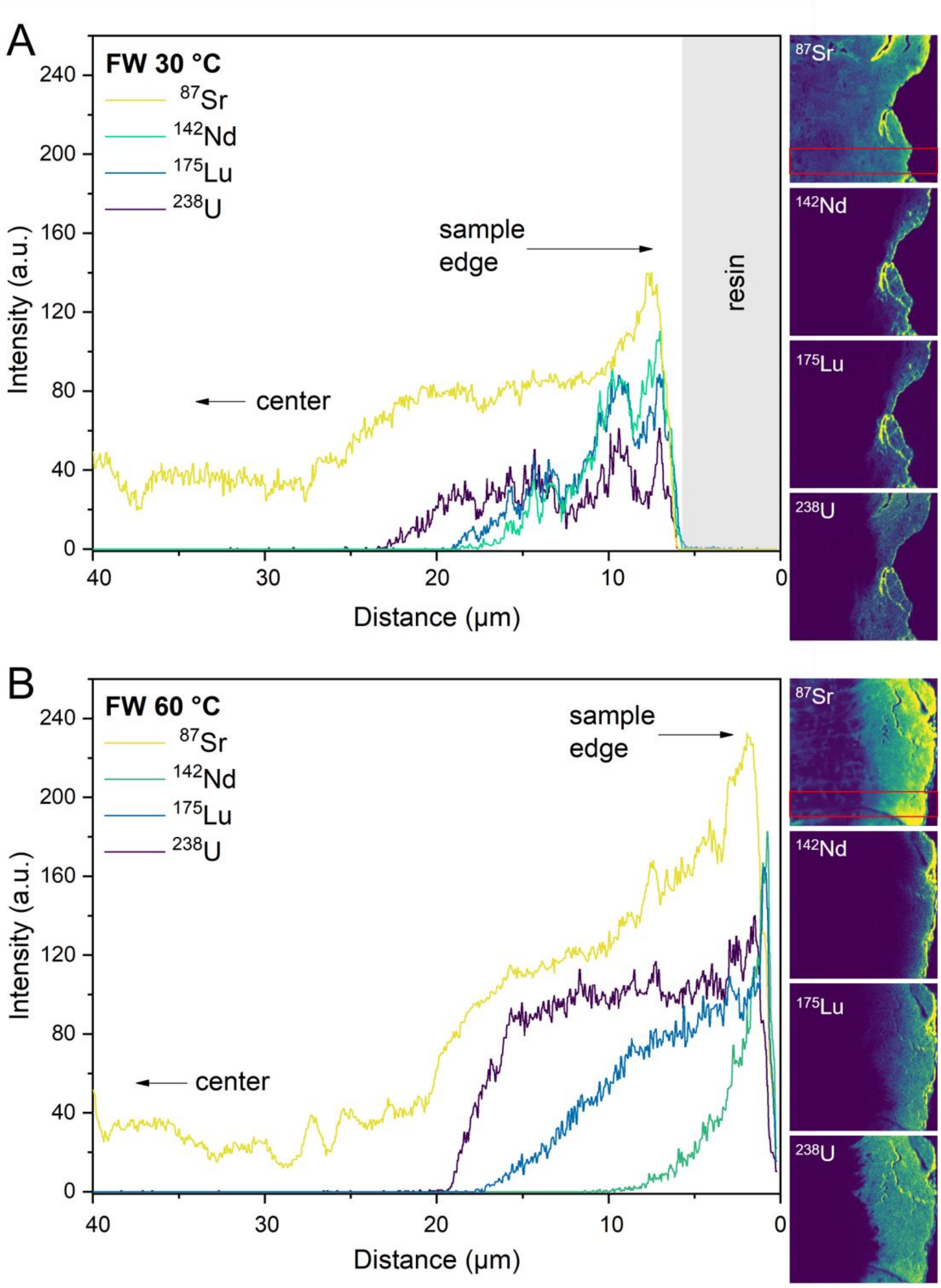

Figure 3.5 | NanoSIMS concentration profiles of FW samples. The intensity of ^{87}Sr, ^{142}Nd, ^{175}Lu, and ^{238}U nanoSIMS signals as a function of distance from the surface of CB samples immersed for 30 d in FW solution at **(A)** 30 °C and **(B)** 60 °C. The red boxes in the ^{87}Sr nanoSIMS maps mark the regions from which the concentration profiles were derived. a.u. = arbitrary unit.

Representative element concentration profiles extracted from the nanoSIMS images of the FW series display the intensity of Sr, Nd, Lu, and U as a function of distance from the surface of CB samples (Fig. 3.5). The greatly fluctuating Sr concentration profiles show that Sr deeply infiltrated the CB (Fig. 3.5A, B), indicating fast but isolated transport paths, i.e., via the CCN. In contrast, Nd, Lu, and U were only detected within the outermost 20 µm. In the 30 °C sample, Nd, Lu, and U showed relatively similar distribution patterns (Fig. 3.5A), whereas, in the 60 °C sample, a clearly distinct spatial distribution of these elements became apparent (Fig. 3.5B). The Nd content continuously decreased from the sample's edge towards the interior of the sample. However, Nd did not penetrate further into the CB than the outermost 10 µm. The shape of the U concentration curve can be described by relatively similar concentrations within the outer 20 µm, limited by a sharp decline in concentration. The form of the Lu profile appears to be intermediate between the shape of the Nd and the U profile. The concentration profiles for the respective elements indicated a transition of the processes responsible for the uptake and incorporation of elements into CB. Intensity profiles of the equivalent 90 °C FW sample are missing, because of the poor data quality of the respective nanoSIMS maps.

3.4.2.3 Atomic-scale observations

In the next step, APT measurements were performed to obtain information about the atomic-scale elemental and isotopic distribution within the RR (Fig. S3.2). In total, more than ten cones were analyzed, but only one cone remained stable enough for a reliable measurement, which revealed an enrichment with U of up to 0.84 at.% in the RR. A weak anti-correlation with U was observed concerning the Ca concentration pattern (≈ 72 at.%) (Fig. S3.2A). Although this was well in line with the observed elemental distribution patterns (Fig. 3.3F, K), there were still significant amounts of Ca present in the U-rich regions, but it remains unclear whether these represent a non-apatite phase. The P signal (≈ 4 at.%) was also anti-correlated with the Ca signal (Fig. S3.2B), which did not necessarily support this assumption because it is difficult to obtain the correct stoichiometry for apatite in atom probe analyses. The main problem here seems to be the high porosity of the reacted samples, leading to the collapse of the APT cones during analysis or creating artifacts partly visible due to white streaks in the reconstructed APT cones (Fig. S3.2B).

3.4.3 Phase composition and structural alteration of the bone apatite phase

To characterize and quantify changes in the bone organic and mineral phase composition and structure of the bone apatite phase as a function of solution temperature at the micrometer scale, confocal Raman spectroscopic measurements were performed on a pristine CB sample and samples altered in SW and FW for 30 d at 30, 60, and 90 °C. Spectra were collected from the edge and the center of the samples. Figure 3.6A shows representative Raman spectra in the wavenumber range between 900 and 1750 cm^{-1} from the outer bone rim of both 90 °C experiments and a representative spectrum from the pristine bone.

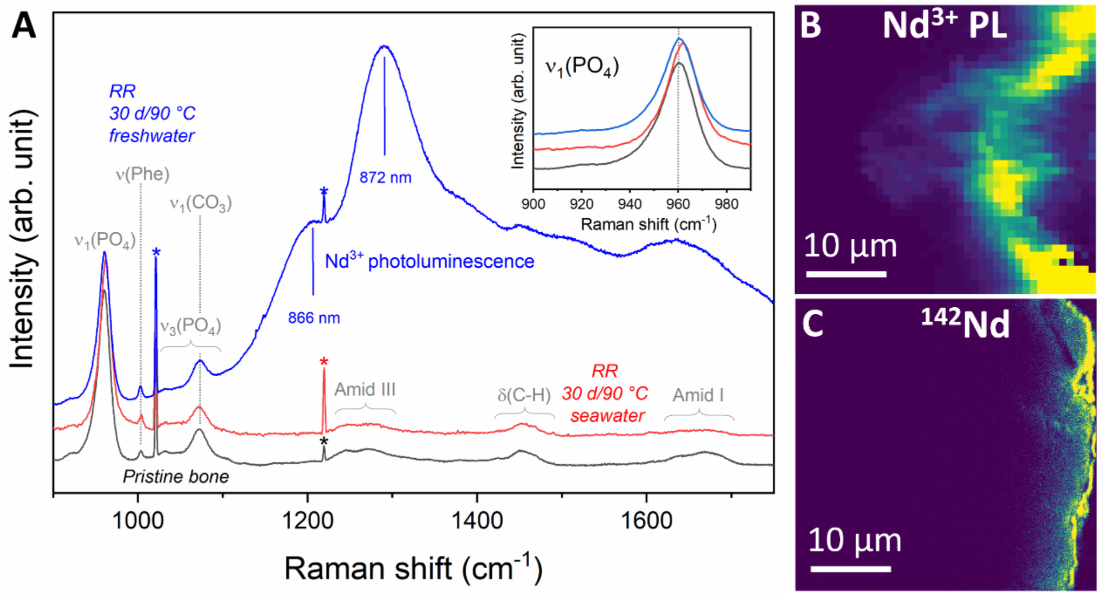

Figure 3.6 | Raman spectroscopic analysis of pristine CB and the RR of altered CB samples. **(A)** Raman spectra of pristine CB (black) as well as of representative CB samples altered in SW (red) and FW (blue) solutions for 30 d at 90 °C. Spectra were normalized to the maximum intensity of the $v_1(PO_4)$ band. The shift of this band is magnified for better comparison in the inset diagram in the upper right. **(B)** Hyperspectral Nd^{3+} photoluminescence image from a CB sample treated in FW solution for 30 d compared with **(C)** the corresponding nanoSIMS Nd distribution image. Differences between both images partly reflect surface changes due to the re-polishing of the sample, which was necessary to remove the nanoSIMS gold coating. (*) the sharp Raman bands are assigned to the laboratory room's ceiling light, used as an internal standard.

These three spectra already show the entire range of visible spectral variations in all 30 d samples. The spectra are characterized by an intense band near 960 cm^{-1}, which can be assigned to the $v_1(PO_4)$ symmetrical stretching mode of the phosphate unit in the bone apatite, whose position is slightly shifted to higher wavenumbers in the RR of the experimentally altered samples (inset Fig. 3.6A). The Raman band at 1,003 cm^{-1} is assigned to the collagen constituent phenylalanine and is present in all spectra from altered samples. An additional, more intense band is visible near 1,070 cm^{-1}, reflecting the $v_1(CO_3)$ vibrational mode of the B-type carbonate group in the apatite lattice. This band partially overlaps with another phenylalanine band at 1,033 cm^{-1} and with broad bands attributed to the $v_3(PO_4)$ antisymmetric stretching vibrations of the phosphate group, complicating the quantification of the carbonate content from a Raman spectrum (Shah, 2020). The bands in the frequency range of 1,215 - 1,340 cm^{-1} and 1,616 - 1,720 cm^{-1} are related to vibrational modes of the collagen components amid III, comprising ν(C–N) and δ(N–H) vibrations, and amid I, respectively. Samples altered in SW resulted in spectra that can hardly be visually differentiated from the spectra of the pristine CB sample. Only spectra from the 90 °C sample show slightly less intense amid I and III bands, i.e., larger $v_1(PO_4)$-to-amid I/III intensity or mineral-to-collagen ratios, indicating some loss of collagen.

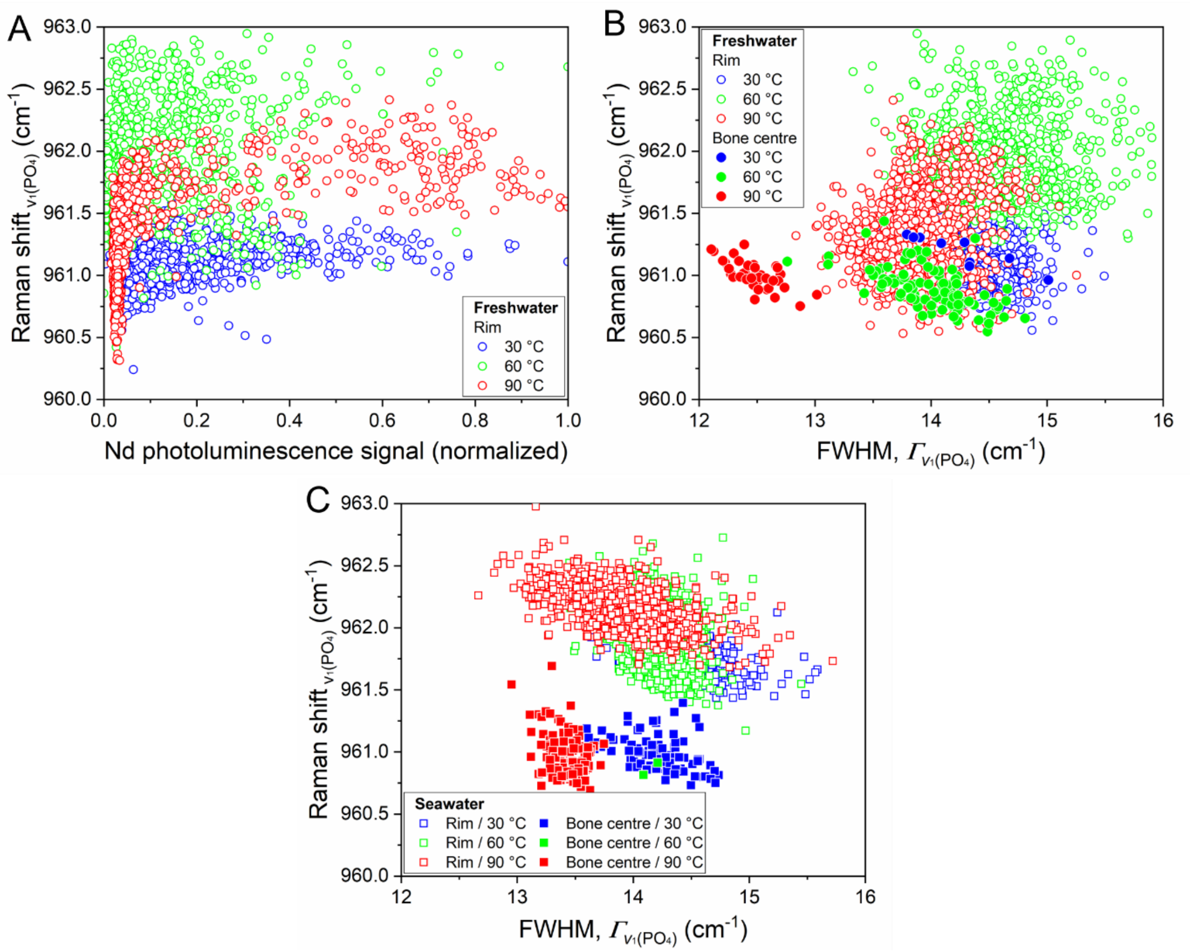

Figure 3.7 | Neodymium PL signals of CB samples altered in SW and FW solutions. **(A)** The Raman shift of the $v_1(PO_4)$ band as a function of the normalized Nd PL signal for CB samples from all temperature regimes exposed to FW for 30 d at 30, 60, and 90 °C. **(B, C)** The frequency of the $v_1(PO_4)$ band as a function of its width given as FWHM for CB samples that were reacted in SW and FW solution, respectively, for 30 d at 30, 60, and 90 °C in SW and FW solutions. Areas in the less altered sample center were measured for comparison due to the strong heterogeneity of the CB samples among each other.

In contrast, Raman spectra from the RR of FW samples are characterized by strong photoluminescence (fluorescence) signals with two maxima at 866 and 872 nm, which can clearly be assigned to $^4F_{3/2} \rightarrow {}^4I_{9/2}$ electronic transitions in Nd^{3+}. This is further confirmed by a good spatial correlation between this photoluminescence (PL) signal and the relative Nd concentrations obtained by nanoSIMS (Fig. 3.6B, C). To quantitatively evaluate the Raman data set, the $v_1(PO_4)$ band position was plotted against the normalized Nd PL signal (Fig. 3.7A). The overall strongest shift of the $v_1(PO_4)$ band to higher wavenumbers (frequencies) is observed in the FW 60 °C sample, but the important information here is that the Nd PL signal is not correlated with changes of the $v_1(PO_4)$ frequency. Information about the structural state of the bone apatite is contained in the position and width of the $v_1(PO_4)$ band, the latter usually specified as the FWHM. Both parameters were plotted against each other for all Raman data of each sample treated for 30 d in the SW (Fig. 3.7B) and FW solution (Fig. 3.7C).

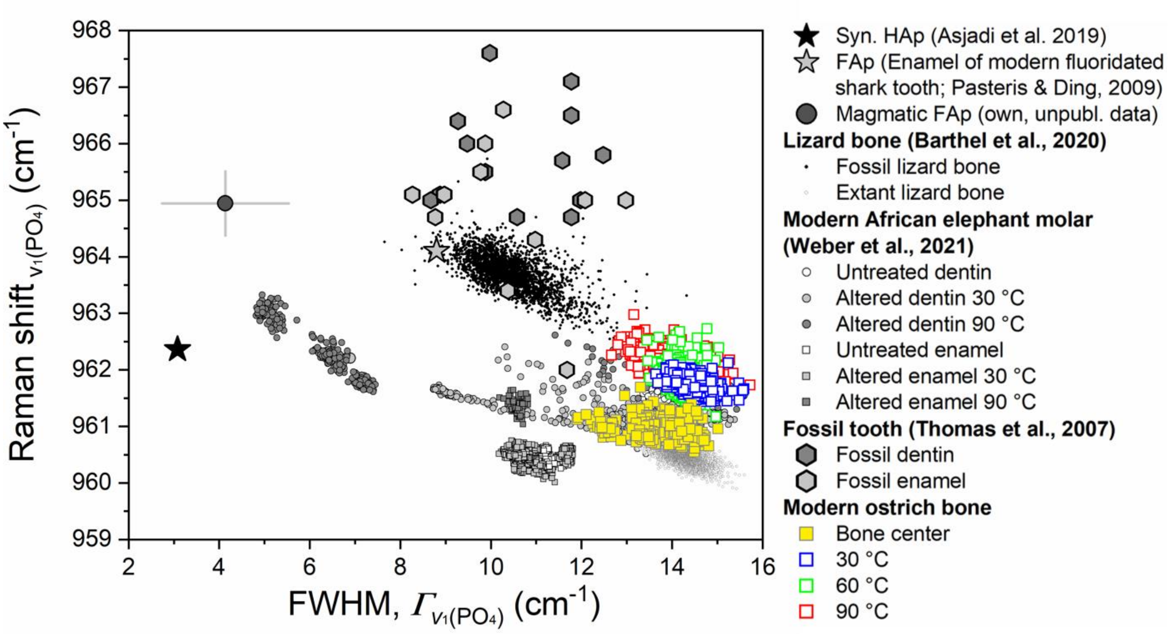

Figure 3.8 | Raman spectral parameters of reference materials and CB samples altered in a SW solution. The frequency of the $v_1(PO_4)$ band as a function of the bandwidth, given as FWHM, for the SW experiment series in comparison with reference data from different modern and fossil bones (Pasteris and Ding, 2009; Barthel et al., 2020) and teeth (Thomas et al., 2007), from experimentally altered teeth (Weber et al., 2021), synthetic HAp (Asjadi et al., 2019) and magmatic FAp (own, unpublished data).

The Raman band parameters obtained from the margin of the altered samples were compared with those obtained from the sample center and various pieces of the pristine bone. Along the edge of the SW samples, a significant shift $v_1(PO_4)$ band towards higher wavenumbers is observed at all three temperatures. There is a clear separation of the analyses from the sample margin compared to those from the interior of the samples and the pristine CB. In FW samples, there is no such distinct frequency difference between the analyses from the RR and the interior. Here, the $v_1(PO_4)$ frequency range is much higher and more evenly spread than in SW samples. Surprisingly, the FWHM of the $v_1(PO_4)$ band did not change significantly. It rather slightly increased when considering the entire data set. This is most pronounced for the 90 °C FW sample, where the $FWHM_{v1(PO4)}$ values from the interior are significantly lower than those from the RR (Fig. 3.7C). In general, the position and width of the $v_1(PO_4)$ band of the unaltered center of the CB samples mark a linear trend towards well-ordered nano-crystalline HAp (Fig. 3.8; Asjadi et al., 2019) that should result when both the size and the structural order of the nm-sized carbonated bone apatite crystallites increase by their recrystallization to HAp. The frequency is comparable to those for pristine tooth dentin and modern lizard bone but smaller than for pristine enamel (Fig. 3.8). Analyses from dentin experimentally altered in an initially F-free, acidic solution partly follow this trend (Weber et al., 2021).

3.4.4 Kinetics of element uptake by cortical bone

The solution composition after a given reaction time (Table S3.1) complements the chemical analyses of the altered bone specimens. Overall, the concentrations of all elements, except P, show the strongest decrease already within the first three days. P was the only element initially released from the bone into the solution. In solutions derived from 60 or 90 °C experiments that ran for 14 d or longer, this was reversed, and P uptake from the solution into the bone occurred. For B, the opposite was observed; after an initial distinct uptake into the bone within the first day, B was released back into the solution, slightly correlating with the increase in temperature. The time-dependence of the Zn, Sr, Nd, Lu, and U contents in solution – elements predominantly enriched in the RR – can be used to gain quantitative insights into the kinetics of the overall trace element uptake process in CB. The element uptake is given by the difference between the concentration (mg/kg) of the element in the initial starting solution, c_i, and the experimental solution after the experiments, c_a. For internal comparability, the element uptake was normalized by the specific tissue surface, σ, of each bone sample obtained by µCT imaging (Kral et al., 2021; chapter 2). To scale the element uptake to the same surface area, a scaling factor B, given by $B = \sigma/\sigma_m$, was defined, where σ_m represents the average specific surface area from all CB samples.

The following equation is derived to compute the surface-normalized percentage element uptake u_σ:

$$u_\sigma = B \cdot \frac{(c_i - c_a)}{c_i} \cdot 100, \qquad \text{Eq.1}$$

In Fig. 3.9, the surface-normalized percentage uptake of the elements Zn, Sr, Nd, Lu, and U from both solution types FW and SW were plotted as a function of time. From the graphs it becomes evident that the uptake rates slowed down to zero already within the first three days, i.e., the element uptake reached saturation level. However, U is an exception in that it did not reach element uptake saturation in CB until after about 18 d (Fig. 3.9F). A two-parameter exponential function of the form

$$u_\sigma = S \cdot (1 - \exp(-bt)) \qquad \text{Eq. 2}$$

was found to be a suitable empirical function to fit the observed time evolution of u_σ and, thus, to determine the asymptotic saturation level, S, and the initial element uptake rates, r, for the elements Sr, Zn, U, Nd, and Lu from both solutions at each temperature (Table S3.2). The rate at a given time t is given by

$$r = \frac{\mathrm{d}u_\sigma}{\mathrm{d}t} = S \cdot b \cdot \exp(-bt) \qquad \text{Eq. 3}$$

and, thus, at $t = 0$, i.e., far from equilibrium by

$$r = S \cdot b. \qquad \text{Eq. 4}$$

In Fig. 3.10A, the fit parameter S is given for the Zn, Sr, U, Lu, and Nd uptake from both solutions against temperature. The saturation level appears to increase linearly with temperature for all experiments, with Lu and Nd having the lowest positive slopes, both of which do not differ significantly from zero at the 95 % confidence level, i.e., the saturation level of both REEs appears to have been independent of temperature.

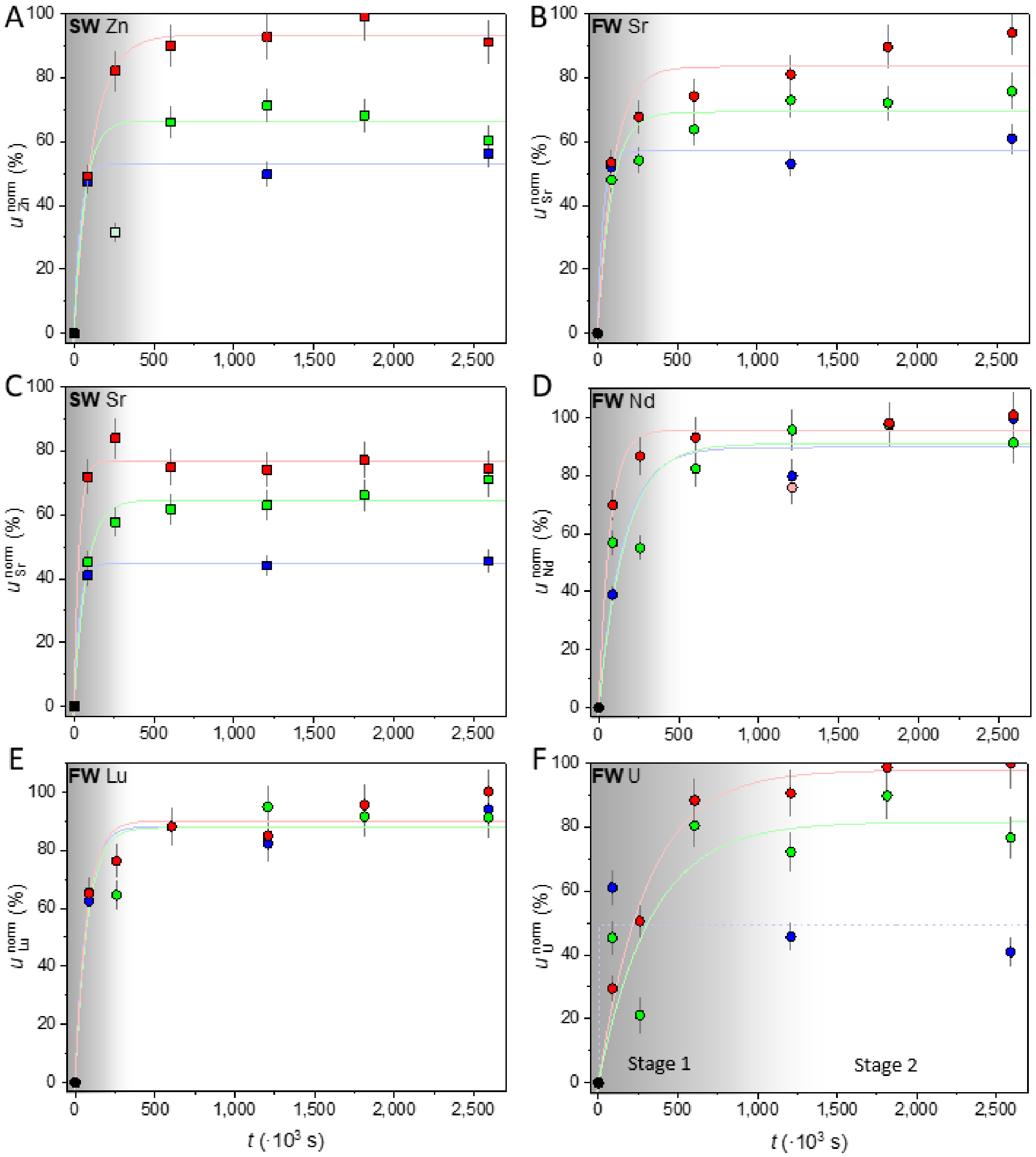

Figure 3.9 | Normalized element uptake of trace elements. **(A)** Zn from SW, **(B)** Sr from FW, **(C)** Sr from SW, **(D-F)** Nd, Lu, and U from FW, respectively, as a function of time. Error bars represent the 2-sigma error. Lightly colored data points in **A** and **D** were excluded as outliers from the fit.

From the rate r, it is possible to estimate the empirical activation energy, E_A, for the element uptake process(es). For this, ln(r) is plotted as a function of the inverse temperature in Fig. 3.10B (Arrhenius diagram). Suppose the activation energy of the process under consideration is constant over the investigated temperature interval; there should be a negative linear correlation with the slope, m, being proportional to the activation energy, i.e., $m = -E_A/R$ with R as the gas constant. Hence, the steeper the slope, the higher the activation energy. It is noticeable in Fig. 3.10B that, in general, there is only a very weak temperature dependency of the element uptake in CB. In fact, except for Nd and Sr from SW, most of the slopes are positive if a linear function is fitted to the data, implying unrealistic negative activation energies. However, the sampling number of the 30 °C experiments was smaller, so only the 1 d data points mainly control the fit parameter *b* in Eq. 2. This is particularly evident from the unrealistic fit of Eq. 2 to the U data from the 30 °C experiment (Fig. 3.9F), which were also excluded from the plots in Fig. 3.10. Therefore, a linear equation was only fitted to the 60 and 90 °C data, excluding U, as its uptake rates are significantly lower than those of the other elements.

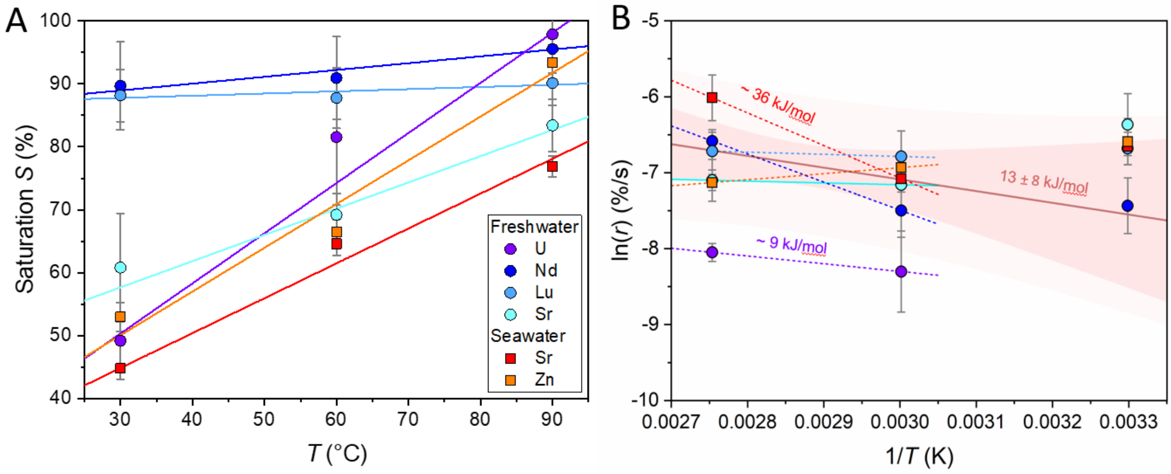

Figure 3.10 | Kinetics of element uptake. **(A)** Element saturation level, S, as a function of temperature for Sr, Nd, Lu, and U in FW experiments and Sr and Zn in SW experiments. **(B)** The logarithm of the element uptake rate, r, is plotted against the inverse temperature. The symbol legend applies to both plots.

The slope yields empirical activation energy for the entire element uptake process of 13 ± 8 kJ/mol for the elements Zn, Sr, Nd, Lu, and U, which has a relatively large error but is different from zero with an error probability of 84 %. Nevertheless, the 95 % confidence and prediction intervals of the linear fit include most of the 30 °C data, but they do not include the U data, further indicating that the uptake of U is significantly slower than the uptake of the other elements. In addition, the activation energies were directly calculated from the slope of the tie lines between two data points of one experimental series, yielding a maximum value of ≈ 36 kJ/mol for Sr uptake in the SW solution. For U uptake, ≈ 9 kJ/mol was obtained, while the logarithm of the measured Zn uptake rate was positively correlated with 1/*T*, suggesting a very low activation energy for Zn uptake.

3.4.5 Weight loss kinetics

The weight loss of the CB samples in the experiments with FW and SW solutions can be attributed predominantly to the decay and loss of collagen. While significantly less bioapatite was dissolved – the cortical porosity increased only marginally (Kral et al., 2021; chapter 2). Thus, the temperature-time dependency of the sample weight contains information about the kinetics of the collagen decay. To account for different sizes of the CB samples, the measured weight loss was normalized to the initial specific volumes of the CB samples (Kral et al., 2021; chapter 2) and then plotted against the reaction time (Fig. 3.11).

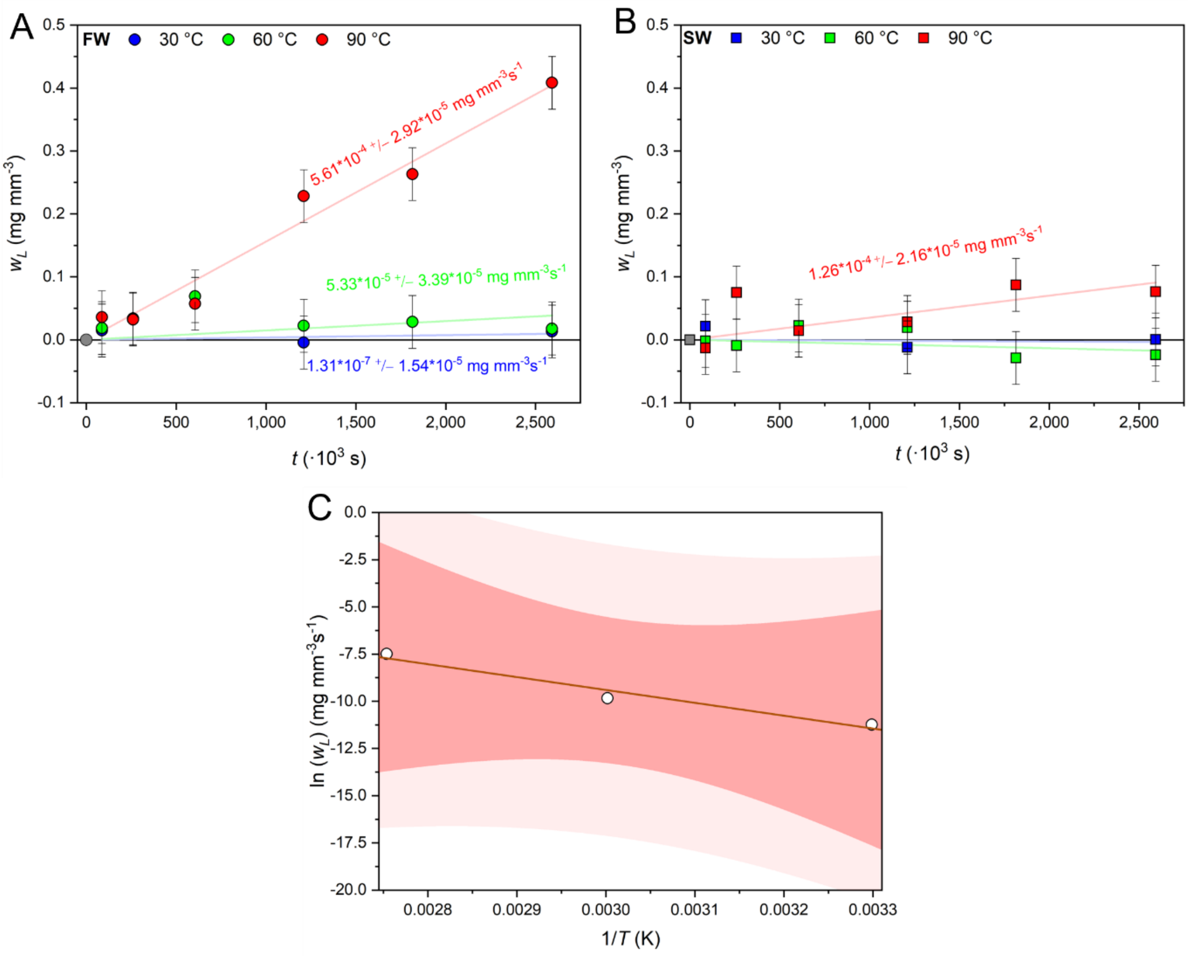

Figure 3.11 | Weight loss kinetics. Volume-normalized weight loss (*wL*) as a function of time. Weight loss rates were calculated for samples exposed to **(A)** FW and **(B)** SW solutions for each temperature. **(C)** *wL* rates were plotted in an Arrhenius diagram against the inverse temperature.

Since weight loss is linearly correlated with time, an intercept-free linear-fitting model ($y = bx$) was used to determine the volume-normalized weight loss rate, w_L. In the FW experimental series (Fig. 3.11A), the rate was low at 30 and 60 °C, and not significantly higher than zero ($w_L = 0.13 \pm 0.15 \cdot 10^{-6}$ mg/mm^{3}s and $5.3 \pm 3.4 \cdot 10^{-5}$ mg/mm^{3}s, respectively), but significantly higher at 90 °C ($w_L = 5.60 \pm 0.29 \cdot 10^{-4}$ mg/mm^{3}s). Nevertheless, if the logarithms of the weight loss rates are plotted against $1/T$ in an Arrhenius diagram, a linear relationship with a negative slope is observed that corresponds to an empirical activation energy of $E_A = 61 \pm 11$ kJ/mol (Fig. 3.11C). In SW experiments, however, only the rate at 90 °C was significantly different from zero ($w_L = 1.26 \pm 0.22 \cdot 10^{-4}$ mg/mm^{2}s; Fig. 3.11B).

3.5 Discussion

3.5.1 Early structural and textural modifications of the cortical bone samples

Following the exposure of CB samples to aqueous solutions with either FW or SW composition, a previously conducted study showed that on a scale down to 3 µm, the CB microarchitecture was largely unmodified (Kral et al., 2021; chapter 2). In contrast, the X-ray BSE images obtained in the present study clearly revealed that within just 1 d of the experiment, the formerly intact CB (Fig. 3.2A) had been strongly pervaded by MCs (Fig. 3.2B-D). However, the large dimensions of some MCs contrasted distinctly with the decrease in cortical porosity (Ct.Po) determined in CB samples immersed in FW solutions (e.g., $\Delta\mathrm{Ct.Po}_{90\,°\mathrm{C},\,1\mathrm{d},\,\mathrm{FW}} = -15 \pm 3$ %, Kral et al., 2021; chapter 2). The number of formed minerals necessary for such a pore space reduction would have rather been reflected by an increase in weight by 0.34 % instead of a slight decrease as observed (e.g., $\Delta\mathrm{wt}_{90\,°\mathrm{C},\,1\mathrm{d},\,\mathrm{FW}} = -0.776 \pm 0.001$ %). In CB samples from FW experiments terminated after 3 d, the Ct.Po showed the opposite trend, i.e., the pore space increased (e.g., $\Delta\mathrm{Ct.Po}_{90°\mathrm{C},\,3\mathrm{d},\,\mathrm{FW}} = 11 \pm 2$ %), although still a large number of MCs as well as slow, but continuous weight loss were detected (e.g., $\Delta\mathrm{wt}_{90\,°\mathrm{C},\,7\mathrm{d},\,\mathrm{FW}} = -1.910 \pm 0.002$ %). Thus, it is most likely that neither mineralization processes nor MC formation predominantly caused the temporary decline in Ct.Po. This supports the first hypothesis by Kral et al. (2021; chapter 2) that collagen swelling, a temporary mechanism with large spatial impact (McKernan & Dailly, 1966), must have significantly reduced the pore space after 1 d. Collagen swelling is caused by the interaction of collagen fibers with aqueous solutions. The solution must therefore have penetrated large parts of the CCN only hours after the initiation of the experiment. This interpretation is indirectly supported by the deep infiltration of Sr, Mg, and Zn into the CB samples.

A second hypothesis suggesting that the increased volume of the swollen collagen fibers must have exerted mechanical stress on the mineralized tissue and thus could have led to MC formation as observed for fossil bone (Pfretzschner, 2000) could not entirely be confirmed by the results of the present study. In CB samples exposed to SW solutions, MC formation also occurred, albeit less pronounced, while collagen swelling was unlikely to happen for physicochemical reasons (Kral et al., 2021; chapter 2). Although it is still not entirely known how the MCs were formed, it is important to note that the number of MCs decreased notably after approximately 14 d – they presumably got filled, even though this is only reflected by an increase in greyscale values as well as Ca and P concentration in the sample's interior. Overall, the CB microarchitecture remained broadly intact, although the bone must have been saturated with the external aqueous solutions.

3.5.2 Element uptake and spatial distribution in cortical bone samples

Dissolved ions were transported via the aqueous solutions into the CB through the CCN and following collagen-crystallite interfaces. However, the elements' penetration depth differed notably. Directly along the sample's edge, an X-ray-dense, sharply delineated, up to 20 µm thick RR became visible in µCT (Kral et al., 2021; chapter 2) and BSE (Fig. 3.2F) images from samples altered in FW solutions. The RR was characterized by higher contents of Mg, Sr, Nd, Lu, and U. It is known that not only divalent molecules and cations (UO^{2+}, $Sr^{2+,}$ and Zn^{2+}), but also mono-, tri-, tetra- and hexavalent cations (Na^{+}, REE^{3+}, U^{4+}, U^{6+}, respectively) can substitute for Ca^{2+} in a metastable hydroxylapatite phase in compliance with a specific charge-compensating mechanism (Pan & Fleet, 2002; Trueman et al., 2004, 2006). CB samples derived from experiments with the SW solutions are characterized by an outer zone enriched with Sr and Zn, which is thus not visible in BSE and µCT images (Kral et al., 2021; chapter 2) but can also be considered a RR.

The penetration depth of the elements enriched in the RR differed notably. The largest change in spatial distribution was observed for Mg, Zn, and Sr. These elements penetrated deepest into the CB sample and were highly enriched at the bone–solution–interface in the CCN. This demonstrates that the CCN was the preferred transport pathway, allowing for deep penetration of water and dissolved chemical species to the interior of the bone. The CCN is anisotropically oriented, with most cortical canals running parallel to the bone surface (Fig. 3.1B). Cutting the samples from the bone perpendicular to its longitudinal growth direction and the CCN made the cylindric bone samples more easily accessible for the solution even at a relatively low temperature. This is reflected by a thicker RR and greater intra-vascular penetration depth in the growth direction, i.e., in the direction of most cortical canals (Fig. 3.4K-M) – a pattern that corresponds well with the area enriched with Nd, Lu, and in particular with U (Fig. 3.3J-L). The penetration depth of these elements is negatively correlated with their atomic radii, i.e., Lu^{3+} (173.4 pm) penetrated only slightly further into the CB than Nd^{3+} (185 pm), while the smaller U^{6+} (138.5 pm) penetrated distinctly deeper into the CB sample. Thus, these elements mark a relatively sharp concentration gradient towards the inside of the CB samples (Figs. 3.4K-M, 5), which agrees well with results from fossil bone (Herwartz et al., 2011). However, these concentration gradients must be associated with distinct reaction processes such as adsorption or crystallization rather than purely diffusional transport, as diffusivities of REEs and U in bone are too similar to cause such disparities (Kohn & Moses, 2013). The observed elemental fractionation within the RR possibly reflects different partition and adsorption coefficients (Hinz & Kohn, 2010; Trueman et al., 2011).

The RR was also depleted in Ca and P relative to the sample center, although the high greyscale values imply a higher density and/or a higher average atomic number than observed before the experiments. The relative depletion in P in the RR can be explained by the substitution of CO_3^{2-} for the PO_4^{3-} site in the apatite lattice, which is reflected by an increase in FWHM and by an intensity increase of $v_1(CO_3)$ relative to $v_1(PO_4)$ (Thomas et al., 2007). Both elements, P and Ca, were concentrated at the sample's center (Fig. 3.3F, G), where also additional Ca derived from the experimental solutions was accumulated. Phosphorus was initially not contained in the experimental solutions. Therefore, a slight increase of P (< 0.5 ppm) in the solutions had to be expected from apatite dissolution. However, in 60 and 90 °C experiments, after a duration of 21 d, even these small amounts of P were again removed from the solutions. This is also strong evidence for the re-deposition of P on surfaces of crystals and/or the formation of larger and thus energetically more favorable apatite crystals, which presumably led to the filling of MCs, reflected by a strong enrichment with Ca and P in the sample center and reducing Ct.Po values over time (Kral et al., 2021; chapter 2).

3.5.3 Bone apatite dissolution and/or recrystallization

The RR was already visible on X-ray µCT and BSE images after 1 d. However, this period is too short for assuming that a dissolution-recrystallization process has led to incorporating Nd, Lu, and U into the apatite lattice. It is more likely that they were first adsorbed onto the organic matrix and/or onto bioapatite crystallite surfaces. In the RR, strong PL signals (Fig. 3.6) related to $^4F_{3/2} \rightarrow {}^4I_{9/2}$ electronic transitions in Nd^{3+} were observed using Raman spectroscopy (Panczer et al., 2012; Lenz et al., 2013; Tuschel, 2016; Mikhalyova et al., 2019) with a laser excitation of 785 nm (Fau et al., *in press*). It is common knowledge that REEs act as the main luminescence centers in minerals (Amoroso & Pope, 2015). Thus, in the case of the formation of secondary apatite (with incorporated Nd or Lu), the occurrence and intensity of the PL signal are expected to correlate with a blue shift of the $v_1(PO_4)$ band, which would indicate a shortening of the average P-O bond length and thus the formation of a less defect or F-rich apatite phase. However, such a correlation was not observed (Fig. 3.7A). Moreover, the PL signal was already detectable after 1 d in the 30 °C temperature regime, while the $v_1(PO_4)$ band was not significantly shifted during the entire experimental duration. Consequently, it is more likely that Nd, which is used as a contrasting agent in electron microscopy, because it concentrates in tissues (Koeppenkastrop & De Carlo, 1992; Köhler et al., 2005; Kuipers & Giepmans, 2020), is adsorbed onto the organic matrix and/or onto the surface of the nano-crystalline bone apatite crystallites instead of being incorporated into newly grown or recrystallized apatite. To a certain extent, the same applies to U, which also has biosorption properties (Volesky & Holan, 1995), wherefore $[UO_2]^{2+}$ di-cations can bind to negatively charged amino acid residues in collagen (Tzaphilou et al., 1982). Furthermore, in an experiment conducted by Kohn & Moses (2013), it was demonstrated that U concentration was about 60 times higher in collagen-bearing than in deproteinated bone. The interaction between collagen and the dissolved ions might also have been supported by the initially occurring collagen swelling leading to a drastically enlarged collagen surface, thus providing more options for adsorption and temporally impeding the penetration into CB. Furthermore, this interpretation is also supported by the observed low activation energy for elemental uptake of about 13 kJ/mol.

Over time and accelerated by heat, the organic matrix was continuously hydrolyzed, which is reflected by a distinct weight loss of up to 20 %, especially in 60 and 90 °C experiments (Fig. 3.11, Kral et al., 2021; chapter 2). Collagen degradation led to the exposure of the bone HAp crystallite surfaces to the solution so that dissolution and/or recrystallization of the nm-sized bone apatite crystals was accelerated. Higher Na contents detected in those areas enriched with Nd and Lu may indicate apatite recrystallization, as the replacement of Ca^{2+} by REE^{3+} requires a monovalent charge-balancing ion like Na^{+} (Voigt et al., 2017), but generally, charge compensation may also be achieved by defect formation, resulting in non-stoichiometric, Ca-deficit hydroxylapatite (Asjadi et al., 2016).

Notably, solution analyses revealed (after an initial uptake) a release of B from the CB sample into the solution over time, particularly in 90 °C experiments. Boron is known to strengthen bone by binding either to the hydroxyl group of hydroxylapatite and/or collagen I (Rondanelli et al., 2020 and references therein). Thus, the release of B into the solution can imply both intensified dissolution of the apatite phase and/or degradation of collagen.

The observed linear relationship between the weight loss rates (w_L) in FW experiments and the inverse temperature yielded an empirical activation energy of 61 ± 11 kJ/mol. Information on collagen degradation kinetics under wet conditions is scarce. Nevertheless, this value can be compared with the E_A measured for the decay of bone collagen in hydrochloric acid, which varies between 6.8 and 25.1 kJ/mol (Castro-Ceseña et al., 2011), while the denaturation of bone collagen induced by heat and under dry conditions (T = 450-670 K) requires an activation energy of 127 ± 8 kJ/mol (Lambri et al., 2016). It is recalled that in both experimental series, w_L was accelerated by increasing the temperature from 60 to 90 °C (Fig. 3.8A, B). These results fit with observations made in a thermal study on unmineralized and mineralized collagen, which showed that in a hydrated environment, the internal cross-links between collagen fibrils break at 65 ± 5 °C, and denaturation starts, ultimately leading to collagen degradation at more elevated temperatures (Bozec & Odlyha, 2011) and thus to weight loss. The distinctly lower weight loss rates in SW experiments clearly showed the effect of (local) pH on the kinetics of bone apatite recrystallization, particularly concerning the recrystallization window (pH range between 7.6 and 8.1) defined by Berna et al. (2004) under which apatite recrystallization was enhanced. Thus, it is conceivable that higher recrystallization rates - reflected by an increase in greyscale intensity in the sample's interior - in SW experiments counterbalanced the heat-induced collagen loss, which would also fit with the observed lower number of MCs. The Raman spectra of FW samples did not allow conclusions concerning collagen degradation or preservation due to intense PL signals covering the collagen-related Raman bands. However, in the SW sample, a significant reduction of the intensity of collagen-related Raman bands, e.g., the amid I or III bands, was observed, which is clear evidence for collagen degradation (Fig. 3.5A).

In Raman spectra obtained from the RR of both experimental series, the $v_1(PO_4)$ band position shifted to higher frequencies. This shift is related to a shortening of the P–O bond length in the phosphate tetrahedra of the apatite lattice, likely due to incorporating F^- in the OH^- position. The presence of F was also shown by nanoSIMS element maps, with a distinct enrichment with F in the RR (Fig. 3.4A, B). However, this contrasts with the increase of the FWHM, which is expected to decrease based on the physics of crystal vibrations and, particularly, when fluorapatite (FAp) is formed. This unusual positive correlation between the frequency and the width can be explained by the convolution of the $v_1(PO_4)$ band of two structurally slightly different apatite phases, as, for instance, of FAp and HAp crystallites, forming one broader band with a maximum that is shifted to a higher frequency. In any case, these results indicate dissolution of bioapatite nano-crystals followed by the formation of an F-bearing phase, e.g., authigenic carbonate-FAp. Unfortunately, the APT measurements did not provide reliable information on the spatial elemental distribution at the atomic scale that would indicate the growth of FAp. The high porosity and the mixture of mineral and organic phases made the APT cones unstable, possibly leading to imprecise 3D elemental reconstructions and eventually to their collapse during the measurement.

3.5.4 Element uptake mechanisms and kinetics

3D visualizations of µCT data showed that the RR is unevenly distributed around the CB samples (Kral et al., 2021; chapter 2). Consequently, the CB microstructure has a significant impact on local element uptake and thus on spatial element distribution. It is assumed that the element’s concentration, the physicochemical milieu in the aqueous solution, the element’s partition and adsorption coefficients, the speciation of the element, and the porosity/permeability of the bone are the parameters predominantly controlling element uptake (Trueman & Tuross, 2002). In general, the term “element uptake into bone” covers both the penetration of solutions carrying dissolved ions into the CB as well as the incorporation of elements into the apatite lattice either due to diffusive processes, dissolution-reprecipitation by a ripening process, or due to an interface-coupled dissolution-reprecipitation process (Putnis, 2009). The results of the present study clearly show that it is crucial to separately consider element uptake and incorporation and to consider them as the result of different, parallel, and/or consecutive transport and reaction processes.

3.5.4.1 Element uptake

It is known that because of its spongy properties, within short time scales bone tends to soak up aqueous solutions carrying various elements (Trueman & Tuross, 2002). The element distribution and BSE images did not reveal any significant modifications after 1 d, although 40 to 70 wt.% of the initial element concentration in solution (except P) were already removed from the solutions within this short time. Element uptake saturation levels were reached after 7 d (Fig. 3.7) and increased from 30 to 90 °C (Fig. 3.8A). However, distinct microstructural changes became first observable after exposure of CB to the experimental solution for more than 14 d. Thus, it is conceivable that an initially fast transport process led to an instantaneous pervasion of the bone by the solution and element adsorption to collagen and/or the bone apatite nano-crystals until the bone was saturated in solution. During this relatively quick process, double-charged ions, such as Mg, Sr, or Zn, were transported in solution following interfaces and cracks deep into the bone (Fig. 3.4G, I, J, respectively). In contrast, tri- or higher valent elements such as Nd, Lu, and U were solely concentrated along the outer bone rim. In aqueous solutions, the predominant species of Nd, Lu, and U are Nd^{3+} (Panigrahi et al., 2018), a fully hydrated Lu^{3+} species ($[Lu(OH_2)_8]^{3+}$ (Rudolph & Irmer, 2018), and uranyl di-cations $[UO_2]^{2+}$, respectively. The high absorption coefficients for the dissolved Nd^{3+} and Lu^{3+} ions between water and apatite surfaces (Koeppenkastrop & de Carlo, 1992) as well as their tendency to form complexes with organics (Kuipers & Giepmans, 2020) led probably to a rapid removal from the pore fluids (Trueman et al., 2004) shortly after entering the CCN. Thus, these elements were rapidly scavenged from the ambient aqueous solution into the RR, while divalent cations could penetrate with the solution via the CCN deeper into the CB.

3.5.4.2 Element incorporation

Element distribution patterns in the bone reflect transport and reaction processes, such as recrystallization of the bone apatite phase and/or adsorption onto crystallite surfaces (Millard & Hedges, 1996; Kohn, 2008). Although the exact underlying mechanisms are still not fully understood, it is widely assumed that element distribution within and incorporation into bone mainly occurs via different transport mechanisms and not via volume diffusion (Millard & Hedges, 1996; Kohn, 2008; Herwartz et al., 2011; Kohn & Moses, 2013) leading to substantial differences in the distribution of, e.g., REEs in bones on a µm-scale (Suarez et al., 2010). However, data obtained in the present study clearly revealed that the element distributions differ even on a sub-µm-scale.

The most prominent diffusion models to explain the element/isotope incorporation into bone are (1) diffusion plus adsorption (DA) of trace elements onto crystallite surfaces, leading to a continuous decreasing concentration gradient towards the interior of fossil bone (Millard & Hedges, 1996); (2) diffusion plus reaction or recrystallization (DR) as a result of bioapatite nanocrystalline surfaces being exposed to a fluid and thus initiating surface-driven dissolution-recrystallization processes, which finally leads to the formation of secondary apatite crystals of different compositions – a sharp border between altered, i.e., recrystallized material and unaltered material is characteristic of DR (Kohn, 2008); (3) the double-medium diffusion model (DMD), which describes the occurrence of two diffusion pathways with different transport properties. DMD concentration profiles typically show very steep concentration gradients in the outermost part of the bone, similar to DA profiles. Concentrations also decrease with distance, but not as much as in DA models. This type of diffusion model is characterized by the relatively high trace element concentration far away from the bone's surface, which is assumed to be related to fast, inter-crystalline diffusion (Kohn, 2008).

In a study performed by Suarez & Kohn (2020), REE and U concentration profiles of partially and completely fossilized bone samples obtained by LA-ICPMS were assigned to different diffusion models. These authors postulated that the exponentially decreasing concentration profile of REEs is typical for either DA or DMD. In contrast, the U profile is associated with DR. These results do not entirely match the observations made in our study. The here observed concentration plots of nanoSIMS isotope distribution images can be better explained by a transition from a purely transport-controlled process (^{142}Nd) towards a transport-reaction process, whereby the reactive part became the predominant part with increasing atomic number (^{175}Lu → ^{238}U). The intensity profile of Lu can be best described as an intermediate state between DA and DR. In contrast, the concentration profile of Sr is similar to a DMD profile. However, it is suggested that instead of fast, inter-crystalline diffusion, a simple transport-reaction process must have caused the higher Sr concentrations further away from the sample's edge - the same applies for Mg and Zn. One possible process is a fast, kinetically uninhibited transport of elements by the solution that percolated through isolated pathways, i.e., the CCN. This is followed by adsorption and/or local interface-coupled dissolution-reprecipitation reactions, which are much slower. NanoSIMS images showed unambiguously that the respective elements were only concentrated around the CCN, whereas diffusion in nanocrystalline HAp would have led to an even enrichment in the interstitial bone (Fig. 4 G, I-M). Here, it needs to be mentioned that with quantitative point analysis or line scans, isotope distributions on such a small scale cannot be resolved, particularly not by using µm-sized spot sizes, because every single measurement would cover much more unaltered than altered bone areas. NanoSIMS analysis, however, provides an extremely high lateral resolution of 50-150 nm and high mass resolution, thereby allowing to determine any element and its isotopes at the nanometer scale and resolve such element distribution patterns. However, the resolution is still not good enough to resolve intra-nanocrystalline chemical patterns.

3.5.4.3 Reaction kinetics

Our time-dependent chemical data revealed that the element uptake of Zn, Sr, Nd, Lu, and U into bone was only barely kinetically inhibited and that the uptake occurred rapidly after the CB samples were exposed to the aqueous solutions – for all elements except U, a saturation level was reached already within the first 3 d. A clear positive linear relationship between the height of the saturation level in CB samples and the temperature was found for Zn, Sr, and U, while the uptake of Nd and Lu seemed to have been independent of temperature. Fernández-Seara and colleagues (2002) have investigated diffusional transport mechanisms of water in CB using nuclear magnetic resonance imaging and spectroscopy. Their experiments at different temperatures revealed a distinct temperature-dependency for the diffusional transport of water through the CB matrix. It was further found that the interaction between water and the bone matrix is diffusion-limited, which is reflected by a higher activation energy of $E_A = 26.8$ kJ/mol than for self-diffusion of free liquid bulk water ($E_A = 18.9$ kJ/mol, Mills 1973; Fripiat et al., 1984). The activation energies determined in the present study of about 13 kJ/mol are in the order of self-diffusion of water (Table S3.2), i.e., the element uptake into bone is not significantly kinetically inhibited.

3.6 Conclusion

This high spatially and time-resolved experimental *in vitro* bone taphonomy study was intended to determine the effects of aqueous alteration on CB under early diagenetic conditions. The most prominent finding is that distinct modifications of the major and trace element composition in bone caused by *post mortem* alteration processes started immediately after the bone’s exposure to artificial FW and SW solutions. The element uptake rates slowed down to almost zero within the first three but not later than after 18 d. The second major finding is that significant alteration of the organic and mineral phase, particularly at the bone samples' margins, occurred within the first few hours to days after exposure to an aqueous solution and not after several years as previously assumed. Most elements, particularly Sr, Nd, Lu, and U, were concentrated behind a diffusion-reaction front near the sample's surface, which was only clearly detectable in samples exposed to FW solutions. Concentration profiles covering the RR revealed a transition from a purely transport-controlled process (^{142}Nd) towards a transport-reaction process (^{175}Lu), whereby the reactive part is more dominant the larger the atomic number (^{238}U). Additionally, fast transport-reaction processes led to the rapid distribution and enrichment of Mg, Sr, and Zn within the CB through the infiltration of the solution along the CCN.

From these results, a more detailed, albeit phenomenological model for the interaction between CB, aqueous solutions, and the elements dissolved therein can be derived: it is here suggested that the elements concentrated in the RR are first and immediately bound by adsorption onto collagen fibers and/or onto crystallite surfaces. Then, collagen hydrolysis, accelerated by heat, leads to releasing those elements into the pore fluid, whereby bioapatite surfaces are exposed to the pore fluid, thus enhancing its dissolution and facilitating reprecipitation and recrystallization processes. The dissolved apatite constituents Ca and PO_4 are relocated into the sample's interior, while thermodynamically more stable, authigenic, and F-bearing apatite crystals are formed in the RR. The entry of solutions is most likely enhanced by the *post mortem* formation of MCs, which, however, can be refilled by new apatite over short periods, thus not resulting in any visual evidence for their previous occurrence. Early recrystallization and formation of more stable carbonated fluorapatite might protect the bone against further alteration and could slow down the uptake of external elements during later stages of diagenesis. However, it is important to point out that Sr and Mg, both proxies for paleo-reconstructions, are altered and incorporated from the aqueous solutions that penetrate much deeper into large areas of the CB in relatively short periods. The results further demonstrate that the specific aqueous environment present immediately *post mortem*, e.g., rainwater puddle, lake, river, or ocean, has a significant impact on the preservation or degradation of bone and thus on the degree of early diagenetic chemical and mineralogical modifications.

3.7 Supplementary material

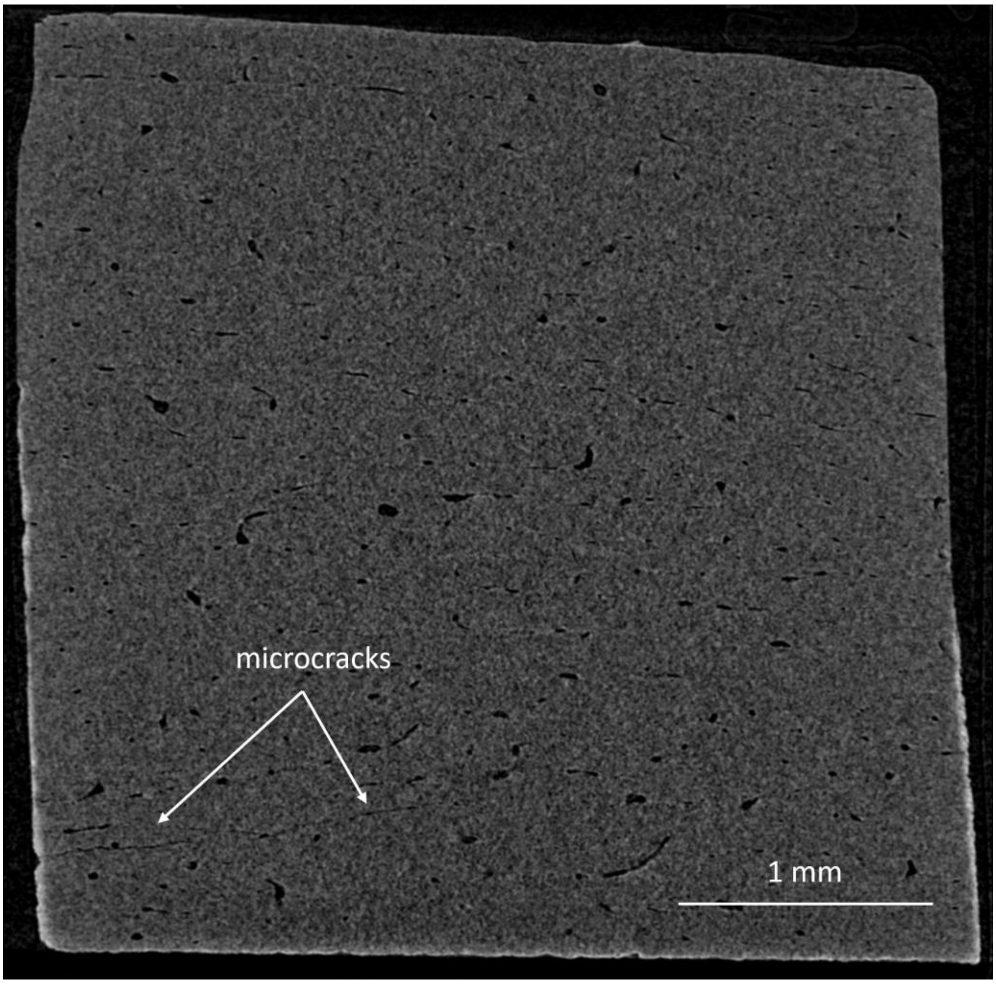

Figure S3.1 | Representative µCT image with MCs.

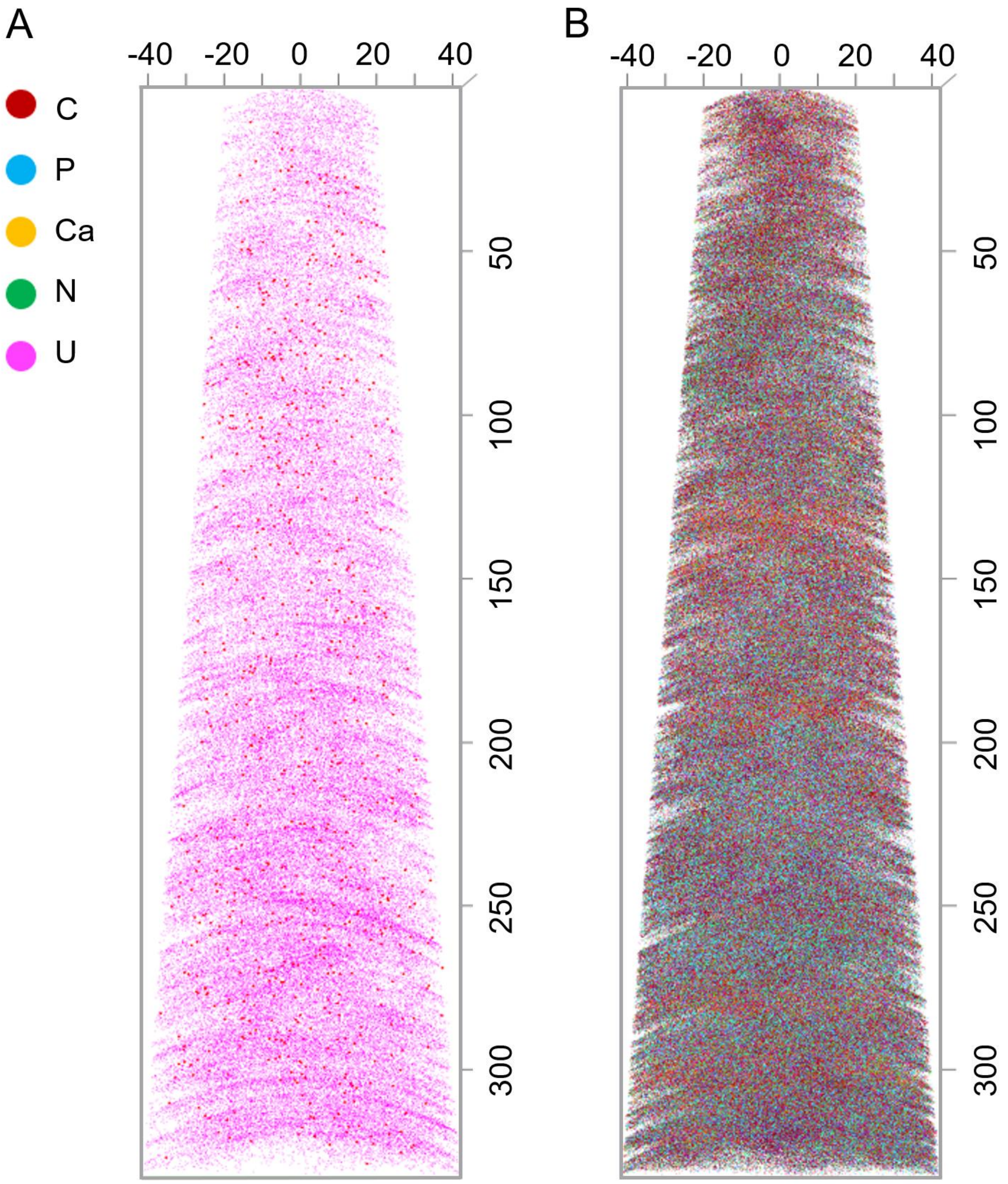

Figure S3.2 | APT maps of a single RR sample from the altered CB sample. **(A)** Ca and U distribution. **(B)** C, P, Ca, N, and U distribution. The scale is given in nm.

Table S3.1 | The solution composition after a given reaction time. The table is continued on the next page.

Solution	T	t	B	SD	Mg	SD	P	SD	Ca	SD
	°C	d	mg/kg		mg/kg		mg/kg		mg/kg	
FW		0	2339	60	121979	1444	3.35	0.03	1425998	15395
	30	1	1432	4	55841	44	75.21	0.57	206965	1358
		14	1592	8	58083	347	93.76	0.11	174175	82
		30	1516	6	58470	165	203.64	2.19	147810	842
	60	1	1447	1	48273	33	46.53	0.19	205208	1972
		3	1464	9	55481	545	94.93	0.96	187010	677
		7	1525	8	49714	359	85.99	1.49	126504	58
		14	1479	7	51894	8	41.82	0.32	132781	142
		21	1611	9	52237	557	87.25	0.28	116255	402
		30	1712	12	50684	471	115.33	0.15	129825	766
	90	1	1505	7	51781	668	93.14	0.17	219741	1065
		3	1559	1	45561	267	163.77	1.56	134756	1111
		7	1870	8	46956	229	286.51	2.16	116084	446
		14	1745	14	40917	385	318.58	0.22	106327	370
		21	1762	3	40944	95	300.64	0.80	94118	610
		30	1751	20	41742	351	205.14	0.34	86917	889
SW		0	3146	68	859204	1646	3.87	0.02	561966	6436
	30	1	1889	6	657990	2409	139.78	1.79	230343	6015
		14	1845	1	674527	4749	261.98	0.75	897414	79545
		30	1905	14	813175	3271	247.28	0.09	294749	4818
	60	1	2044	15	764886	6596	113.38	1.28	302164	3635
		3	2018	14	799983	4490	49.78	1.09	327266	6440
		7	1949	6	773702	11616	175.63	1.81	249257	2694
		14	2052	20	752842	8870	203.66	1.40	275861	5333
		21	2127	10	627509	9594	255.47	2.11	241303	1334
		30	2163	3	672072	1396	84.54	0.81	197968	5050
	90	1	2146	25	754243	6592	146.73	0.18	254678	3525
		3	2135	22	594061	7024	192.67	3.38	194589	1377
		7	2155	8	716427	12839	235.40	1.86	287459	5552
		14	2189	9	658729	4350	246.75	4.47	379353	1017
		21	2162	44	677856	11004	408.06	6.76	237134	1472
		30	2409	2	664917	7239	382.62	0.72	284438	11684
Blank	30		3.27	0.22	2.00	0.10	3.64	0.02	18.9	0.8
	60		0.61	0.04	3.09	0.06	5.62	0.07	47.4	1.5
	90		1.48	0.01	3.77	0.03	16.79	0.00	37.6	1.4

FW = freshwater, SW = seawater

Continuation of Table S3.1

Solution	**T**	**t**	**Zn**	**SD**	**Sr**	**SD**	**Nd**	**SD**	**Lu**	**SD**	**U**	**SD**
	°C	**d**	**mg/kg**		**mg/kg**		**mg/kg**		**mg/kg**		**mg/kg**	
FW		0			137641	941	1754	3	3505	10	15993	210
	30	1			67560	188	1085	6	1362	12	6432	36
		14			61922	109	303.2	0.2	514.8	0.4	8425	7
		30			54876	179	28.1	0.1	246	5	9528	53
	60	1			68720	73	713	3	1114	5	8426	96
		3			62339	272	777.4	0.3	1216	4	12561	222
		7			42327	82	185	2	151.5	0.3	2018	18
		14			44081	66	190	2	403	2	5229	33
		21			38881	29	52	2	305	4	1681	6
		30			33230	26	150	1	299	4	3714	42
	90	1			62890	144	507	5	1180	8	11192	46
		3			46082	99	259	1	875	3	8051	26
		7			31203	91	52.8	0.4	281	2	1248	4
		14			14788	26	289	1	220	1	29	1
		21			13821	6	27	6	143	2	151	1
		30			9430	24	1.94	0.02	26.1	0.3	134	3
SW		0	9611	509	140081	1940						
	30	1	5084	48	82841	226						
		14	4723	39	76879	115						
		30	4152	28	75769	25						
	60	1	4847	50	74428	296						
		3	6447	87	55862	469						
		7	3159	22	52023	103						
		14	2900	29	53678	101						
		21	2836	36	44339	35						
		30	3833	49	41042	4						
	90	1	4777	39	37062	24						
		3	2611	35	35707	125						
		7	1106	9	37146	6						
		14	430	6	33222	132						
		21	308	3	34349	108						
		30	634	4	33302	53						
Blank	30		7	0.1	0.0442	0.0003	< DL		< DL		0.084	0.001
	60		26	0.2	0.1463	0.0004	0.0025	0.0001	0.001	0.000	0.0417	0.0003
	90		1.00	0.02	0.053	0.001	< DL		< DL		1.361	0.004

Table S3.2a | Initial element uptake rates calculated for Nd, Lu, and U at each temperature (°C)

T	**1/T**	**Nd**	**Nd**	**Lu**	**Lu**	**U**	**U**
		b	± 1σ	b	± 1σ	b	± 1σ
30	0.003299	6.58E-06	2.35E-06	1.42E-05	2.96E-06		*Bad fit*
60	0.003002	6.08E-06	2.08E-06	1.29E-05	4.27E-06	3.04E-06	1.57E-06
90	0.002754	1.45E-05	2.15E-06	1.34E-05	3.30E-06	3.26E-06	3.75E-07
		S (%)	± 1σ	S (%)	± 1σ	S (%)	± 1σ
30	0.003299	89.68	6.98	88.16	4.16	49.18	6.10
60	0.003002	90.93	6.55	87.76	4.84	81.56	10.83
90	0.002754	95.55	2.47	90.15	3.60	97.88	2.84
		r = b*S (%/s)	± 1σ	r (%/s)	± 1σ	r (%/s)	± 1σ
30	0.003299	5.90E-04	2.16E-04	1.26E-03	2.67E-04		
60	0.003002	5.53E-04	1.93E-04	1.13E-03	3.80E-04	2.48E-04	1.32E-04
90	0.002754	1.38E-03	2.08E-04	1.21E-03	3.01E-04	3.19E-04	3.78E-05

S = saturation level, b = slope

Table S3.2b | Initial element uptake rates calculated for Sr and Zn at each temperature (°C)

T	**1/T**	**Sr (FW)**	**Sr**	**Sr (SW)**	**Sr**	**Zn**	**Zn**
		b	± 1σ	b	± 1σ	b	± 1σ
30	0.003299	2.82E-05	1.08E-05	2.88E-05	2.41E-06	2.59E-05	7.84E-06
60	0.003002	1.12E-05	3.14E-06	1.31E-05	2.27E-06	1.47E-05	2.63E-06
90	0.002754	9.90E-06	2.68E-06	3.18E-05	9.51E-06	8.59E-06	9.06E-07
		S (%)	± 1σ	S (%)	± 1σ	S (%)	± 1σ
30	0.003299	60.81	8.62	44.77	0.46	52.96	2.28
60	0.003002	69.22	3.37	64.59	1.84	66.46	2.00
90	0.002754	83.40	4.11	76.83	1.67	93.36	1.70
		r (%/s)	± 1σ	r (%/s)	± 1σ	r	± 1σ
30	0.003299	1.72E-03	6.99E-04	1.29E-03	1.09E-04	1.37E-03	4.19E-04
60	0.003002	7.78E-04	2.21E-04	8.43E-04	1.49E-04	9.76E-04	1.77E-04
90	0.002754	8.25E-04	2.27E-04	2.45E-03	7.33E-04	8.02E-04	8.58E-05

S = saturation level, b = slope

4 Phosphate mineralization is an essential process for bone mineralization during diagenesis and fossilization

Anna G. Kral[1*], Thorsten Geisler[1], Paul Guagliardo[2], Thomas Tütken[3]

[1]Institut für Geowissenschaften, Rheinische Friedrich-Wilhelms-Universität, Bonn, Germany; akral@uni-bonn.de; tgeisler@uni.bonn.de

[2]Centre for Microscopy, Characterization, and Analysis, The University of Western Australia, Australia; paul.guagliardo@uwa.edu.au

[3]Institut für Geowissenschaften, Johannes-Gutenberg-Universität, Mainz, Germany; tuetken@uni-mainz.de

This chapter is currently in preparation as a manuscript intended for submission.

Author contributions:

Thorsten Geisler and I designed the study. Paul Guagliardo and I performed the nanoSIMS measurements. I analyzed the collected nanoSIMS data. The Raman spectroscopic measurements were conducted by myself, and Thorsten Geisler aided with data processing and evaluation. Thomas Tütken and I processed the IRIS data, while Thorsten Geisler contributed to the data evaluation and interpretation. Thomas Tütken, Thorsten Geisler and I discussed and interpreted the results. I wrote the manuscript with support from Thorsten Geisler and Thomas Tütken.

4.1 Abstract

Oxygen isotope tracer experiments were conducted to investigate bone mineralization under early diagenetic conditions and to identify the provenance of the phosphate required for bone mineralization. Isothermal alteration experiments were conducted on modern ostrich cortical bone (CB) samples in three different aqueous solutions at 60 and 90 °C for 30 days. Two of the solutions contained ^{18}O-enriched water, and one solution was in contact with artificial sediment that contained ^{18}O-enriched calcium hydrogen phosphate (CHP). These different tracer solutions were used to distinguish between bone apatite recrystallization and new apatite mineralization. Evidence was found that uptake of dissolved PO_4 into the bone occurred in the presence of a sedimentary phosphate source, and new fluorapatite began to form. Moreover, although chemical and structural modifications of the CB occurred, neither newly grown apatite crystallites nor oxygen isotope exchange between dissolved PO_4 and water was found in bones exposed to aqueous solutions at low-temperature conditions lacking a sedimentary phosphate source. The fast incorporation of ^{18}O-doped PO_4 from the CHP accelerated bone fossilization and consequently changed the stable oxygen isotope composition of the phosphate group ($\delta^{18}O_{PO4}$) in bone mineral phase more rapidly than in a diagenetic setting without additional external phosphate. Thus, in order to correctly interpret $\delta^{18}O_{PO4}$ data, knowledge about the burial and diagenetic setting is crucial.

4.2 Introduction

During the fossilization process, the skeletal tissues of vertebrates will be altered by various physicochemical processes and are transformed into a form that will allow bone to survive for millions of years and thus preserve information from times long past. For instance, the stable oxygen isotope composition of the phosphate group ($\delta^{18}O_{PO4}$) in bone mineral phase hydroxylapatite (HAp) is used to determine (paleo)environmental temperatures (e.g., Blake et al., 2010; Pucéat et al., 2010). Fresh bone predominantly consists of a carbonated calcium-phosphate mineral, approximated as HAp (55-60 wt.%), with a composition similar to dahllite ($Ca_{10}(CO_3, PO_4)_6(OH)_2$) (Wopenka & Pasteris, 2005). These crystallites are aligned within an organic matrix of primary type-I collagen fibers (~30 wt.%) (Tzaphlidou, 2008; Boskey, 2015). Furthermore, living bone also contains ≈ 10-15 wt.% of water (Rogers & Zioupos, 1999). For bone to fossilize, HAp must be transformed into a thermodynamically more stable apatite form, such as fluorapatite (FAp). In addition, collagen, which makes up about 25 to 36 vol.% of the bone *in vivo* (Collins et al., 2002; Trueman et al., 2008), gets degraded by chemical and biological processes during diagenesis (Collins et al., 2002; Hedges, 2002; Pfretzschner, 2006). Consequently, in fossil bone, this volume also must be replaced by secondary authigenic apatite, which will require large amounts of exogenous Ca and PO_4. However, it is still unclear where the required material comes from during diagenesis. Possible sources include soft tissue, other bones, and the surrounding sediment, which usually contains little PO_4. Furthermore, little is known about the processes underlying bone mineralization and their effect on the oxygen isotopic composition. Correspondingly, there are still significant gaps in our knowledge about these elements of the fossilization process.

Post mortem, bone taphonomy starts immediately, either leading to the bone's preservation or, more likely, to its decomposition (see Dauphin, 2022 for an overview). The fossilization process during which bone is preserved can be divided into two main stages: early and late diagenesis, which are differentiated by changes in the chemical milieu and bone composition (Pfretzschner, 2004). The early diagenetic stage is characterized by abiotic and biotic decay of soft tissues, loss of collagen, and bone recrystallization (Collins et al., 2002; Trueman & Martill, 2002a; Trueman & Tuross, 2002b; Jans, 2008; White et al., 2014; Turner-Walker, 2019; Procopio et al., 2021). The latter can either happen in the form of a pseudomorph replacement of nm-sized bioapatite and collagen by energetically more favorable and stable authigenic apatite mineral phases, e.g., FAp (Kolodny et al., 1996; Elorza et al., 1999; Berna et al., 2004; Goodwin et al., 2007), or through the addition of authigenic apatite to biogenic apatite crystallites (Hubert et al., 1996; Trueman et al., 2004). When authigenic minerals replace the organic matrix almost entirely, bone cavities such as pore space or cracks get mineralized by secondary minerals during late diagenesis. Such minerals are calcite, siderite, brushite, or different apatite phases, depending on the composition of the diagenetic fluid (e.g., Pfretzschner, 2004; Wings, 2004; Keenan, 2021).

Whether a bone is preserved or decomposed depends strongly on the environmental conditions during early diagenesis (Nielsen-Marsh & Hedges, 2000; Trueman et al., 2004; Kohn, 2008). Decisive for the preservation of bone is the transformation of bioapatite into and the replacement of collagen by carbonated fluorapatite (CO_3-FAp) (Nemliher et al., 2004; Pasteris & Ding, 2009) or similar stable apatite phases. This implies that vast amounts of Ca and PO_4 are required to fossilize bone to infill pore space from collagen degradation and to recrystallize bioapatite to FAp. However, it remains unknown if the Ca and PO_4 for bone fossilization derive from redistribution (i.e., dissolution and reprecipitation) within or among bones or from the embedding sediment. Bone mineralization with new HAp or FAp by Ca and PO_4 derived from a sedimentary source of the burial setting is proposed to be an essential process for bone fossilization (e.g., Trueman & Tuross, 2002b). However, systematic experiments that mainly aim to investigate early bone mineralization under diagenetic conditions and test this hypothesis have so far not been conducted.

In the present study, the provenance of PO_4 for bone mineralization was assessed by *in vitro* alteration experiments of modern ostrich CB with and without artificial sediment containing ^{18}O-enriched CHP. For isothermal aqueous alteration experiments, CB samples were immersed in three different experimental solutions in sealed Teflon© vials for up to 30 d at 30 to 90 °C. ^{18}O was used as a tracer for authigenic apatite growth with different sources of PO_4, i.e., external PO_4 derived from sediment with ^{18}O-enriched PO_4 and internal PO_4 mobilized through bioapatite dissolution. Furthermore, this approach will also allow for investigating the oxygen exchange between dissolved PO_4 and water through the ^{18}O-enriched water used in freshwater- and seawater-like solutions (FW and SW, respectively).

The first two experimental solutions had a FW and SW composition, respectively, and both were labeled with ^{18}O-enriched water but did not contain any sediment (Table 4.1). These experiments aimed at investigating if - and under which hydrochemical conditions - bone can be mineralized with Ca and PO_4 derived from an aqueous solution. In addition, a FW solution (without ^{18}O-enriched water) was used in the third experiment together with artificial sediment containing synthetic ^{18}O-doped CHP to trace a PO_4 transfer from the sediment to the bone. This third solution's composition (Table 4.1) continuously changed during the experiment due to its interaction with the sediment (i.e., dissolution of CHP). Newly grown HAp can potentially be detected by an ^{18}O-enrichment at the sample's edge of the experimentally altered bone samples via ^{18}O-enriched PO_4 transfer via the solution from the sediment because it was not enriched in ^{18}O. Such a scenario may constitute a significant process for bone fossilization in natural sedimentary environments but has not yet been proven experimentally. Under the sub-boiling temperature conditions (30 to 90 °C) of the experiments conducted here, the oxygen isotope exchange between aqueous phosphate and water is slow and thus not be significant during the short duration (30 d) of the experiments (Lécuyer et al., 1999; O'Neil et al., 2003; Geisler et al., 2009). Thus, newly grown ^{18}O-rich HAp can be directly associated with ^{18}O-enriched PO_4 provided by the dissolution of ^{18}O-enriched CHP from the sediment. Mineralogical changes in the bone apatite phase were investigated using confocal Raman spectroscopy, while semi-quantitative nanoscale secondary ion mass spectrometry (nanoSIMS) displayed the spatial

^{18}O and ^{16}O distribution and determined the $^{18}O/^{16}O$ ratios in the altered CB samples. Furthermore, isotope ratio infrared spectroscopy (IRIS) analyses were performed to determine the $\delta^{18}O$ values of the different experimental solutions before and after the experiments. The experiments presented here constitute a fundamental approach aimed at studying potential mineralization processes of bone with PO_4 from an external source during early diagenesis.

4.3 Materials and methods

Cylindric CB samples were drilled from the compacta of a tibia of a modern ostrich (Fig. 4.1) and altered *in vitro* in different aqueous solutions during a previous study (Kral et al., 2021; chapter 2).

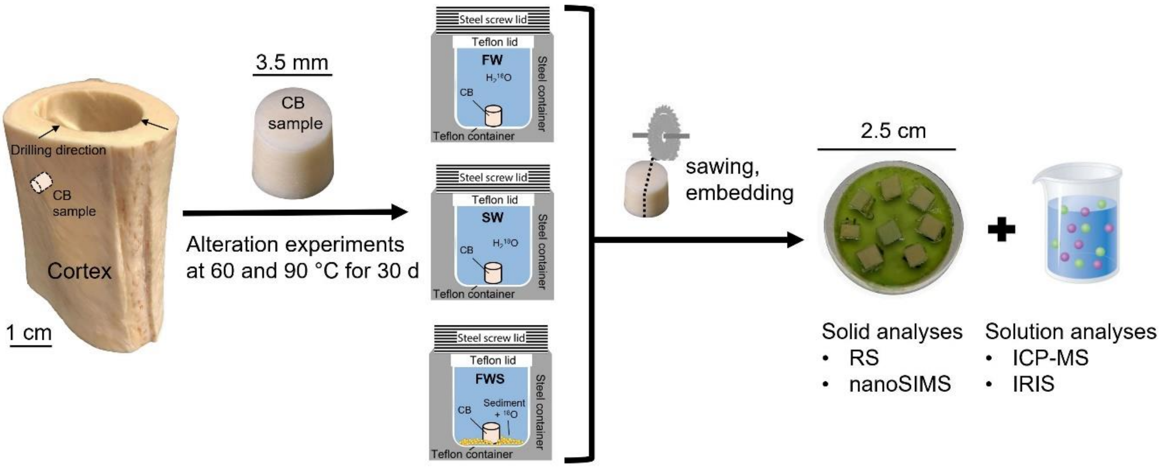

Figure 4.1 | Illustration of the experimental setup (see chapter 2 for further details). Cylindric CB samples (3.5 mm in height and diameter) were drilled out of the bone's cortex. The CB samples were placed in 3 mL Teflon© beakers that contained 2 mL of ^{18}O-enriched FW and SW solutions and 3 mL of the FWS solution, which additionally contained ^{18}O-enriched artificial sediment. The Teflon© beakers were placed in a steel container and heated for up to 30 d at different temperatures (30 to 90 °C) in a custom-made oven. The bone samples were cut into halves and embedded in Technovit© mounts for further geochemical and isotopic analyses. RS = Raman spectrometry, IRIS = isotope ratio infrared spectrometry, nanoSIMS = nanoscale secondary ion mass spectrometry, ICP-MS = inductively coupled plasm -mass spectrometry.

To cover the range of typical natural, near-surface water compositions (i.e., common diagenetic fluids) as closely as possible, the CB samples were immersed in FW and SW solutions (Table 1) and were exposed to 30, 60, and 90 °C for up to 30 d (Fig. 4.1). However, in this study only the 30-days samples from 60 and 90 °C experiments were considered, because these showed the most significant mpodifcations. The experimental solutions contained several elements potentially incorporated *post mortem* in early diagenetic settings and are frequently used to assess diagenesis, e.g., F, Sr, rare earth elements (REEs), and U. Both stock solutions were additionally labeled with ^{18}O-enriched water with 97 at.% ^{18}O (Rotem GmbH, Leipzig, Germany) in a ratio of 2 mL of 97 at.% ^{18}O water on 100 mL MilliQ water from Bonn, Germany, resulting in a $\delta^{18}O_{water} \approx 5,500$ ‰ (Table 4.2). The third solution with a chemical composition similar to FW (Table 4.1) was prepared for an experimental series with artificial sediment as an additive (FWS). Here, the solution itself was not labeled with ^{18}O-enriched water. Instead, the artificial sediment contained ^{18}O-labelled CHP.

Table 4.1 | Composition of freshwater, seawater, and freshwater plus sediment stock solutions given in ppm (modified after Kral et al., 2022; chapter 3).

	FW	**SW**	**FWS**
B^{3+}	2.34 ± 0.06	3.15 ± 0.07	1.79 ± 0.08
Na^{+}	*100.0 ± 0.2*	*10,770 ± 22*	*6.00 ± 0.01*
K^{-}	*100.0 ± 0.2*	*390.0 ± 0.8*	*100.0 ± 0.2*
Ca^{2+}	1,426 ± 15	562 ± 6	197 ± 5
Cl^{-}	*775 ± 2*	*19,350 ± 39*	*600 ± 1*
Mg^{2+}	122.0 ± 1.4	859.2 ± 1.7	67.4 ± 1.5
F^{-}	*5.00 ± 0.01*	*5.00 ± 0.01*	*5.00 ± 0.01*
Sr^{2+}	137.6 ± 0.9	140.1 ± 1.9	122.3 ± 0.2
Zn^{2+}		9.6 ± 0.5	
Fe^{3+}			In sediment (see chapter 2)
Lu^{3+}	3.51 ± 0.01		2.63 ± 0.15
Nd^{3+}	1.754 ± 0.003		0.66 ± 0.02 *
U^{6+}	16.0 ± 0.2		In sediment (see chapter 2)
$^{18}O^{2-}$	12,892.15 ± 100	13,313.2 ± 100	1,994.03 ± 100

The composition of the stock solution constituents B, Ca, Mg, Sr, Zn, Fe, Lu, Nd, and U was determined using a Thermo Scientific Element XR [ppm ± SD]. The elemental concentration of the remaining elements was calculated from the weight-in and is given in italic font [ppm ± 0.2 %]. The isotopic composition of oxygen was determined using IRIS. The weighted substances added to all three solutions are B_2O_3, $NaHCO_3$, NaF, KCl, $CaCl_2$, $MgCl_2$, and $SrCl_2$. The FW solution additionally contained $H_2{}^{18}O$, $NaHCO_3$, $CaCl_2$, $FeCl_3$, $NdCl_3$, $LuCl_3$, and $UO_2(NO_3)_2$. The SW solution comprised $H_2{}^{18}O$, $NaHCO_3$, $CaCl_2$, NaCl, Na_2SO_4, $Ca(NO_3)_2$, and $ZnCl_2$. The FWS solution also contained $NdCl_3$ and $LuCl_3$. Further substances have been added in the form of artificial sediment (see Kral et al., 2021; chapter 2).

* Note that for Nd, a concentration of 0.66 ± 0.02 ppm was determined in the stock solution. However, this value may be biased because, after only 1 d the Nd concentration (determined multiple times) in the solution was on average 2.484 ± 0.002 ppm. The calculated weight-in was slightly higher than that of Lu, so it seems more plausible that the initial Nd concentration is higher than 0.66 ppm – the reasons for this large deviation are presently unknown.

The CHP was synthesized by dissolving it in $H_2{}^{18}O$ (97 at.% ^{18}O), equilibrating the solution for 24 h at 150 °C, and allowing the phosphate to precipitate by evaporation. The ^{18}O content is currently determined using high temperature conversion elemental analyzer (TC/EA, Thermo Fisher Scientific Inc., Bremen, Germany), and it was additionally verified by Raman spectroscopy that ^{18}O was incorporated in significant amounts. More information about the experimental setup and the composition of the materials used for the experiments are described elsewhere (Kral et al., 2021; chapter 2).

IRIS analysis was used to determine the isotopic composition of oxygen ($\delta^{18}O$) of selected experimental solutions (30-d FW, SW, and FWS experiments at 60 and 90 °C) and their respective stock solutions. Aliquots of 0.5 µl were analyzed on a Picarro L2140-i cavity ring-down spectrometer (Picarro, Inc., Santa Clara, CA, USA). For dilution, MilliQ water was used ($\delta^{18}O_{MQ} = -5.47 \pm 0.05$ ‰). Internal standards (Chamonix2020, $\delta^{18}O = -14.15$ ‰, Kona2020, $\delta^{18}O = 1.12$ ‰, and Mainztap2020, $\delta^{18}O = -8.78$ ‰) were analyzed to normalize the $\delta^{18}O$ values of the samples to the VSMOW-SLAP scale (de Graaf et al., 2021). The $\delta^{18}O$ value of each sample was given as the average result of a duplicate measurement ($\delta^{18}O \pm$ 1SD ‰). The precision of the measurements was better than 0.1 ‰. The analytical protocol and information on data calculation are provided elsewhere (de Graaf et al., 2020, 2021).

The pristine control sample and CB samples exposed for 30 d at 60 and 90 °C to FW, SW, and FWS solutions were selected and prepared for nanoscale secondary ion mass spectrometry (nanoSIMS) analyses. A nanoSIMS 50L system (CAMECA SAS, Gennevilliers Cedex, France) equipped with a Cs^+ ion beam was used to generate oxygen isotope distribution maps (^{16}O and ^{18}O) of 40 µm x 40 µm large areas along the sample's edge, consisting of 512 x 512 px. Details on the measurement procedure can be found in Kral et al. (2022, chapter 3). The plugin OpenMIMS v3.0.5 (http://nano.bwh.havard.edu) was used in Fiji v1.53c (Schindelin et al., 2012) for generating and processing the nanoSIMS images. For color-coding of the ^{18}O and ^{16}O isotope distribution maps and to display modifications of the ^{18}O distribution relative to the ^{16}O distribution in the analyzed areas, the uniformly-scaled Viridis color palette was used. The $^{18}O/^{16}O$ value was determined by the counts per pixel extracted from the nanoSIMS images. The Poisson counting error was determined for both the ^{18}O and ^{16}O counts, and the uncertainty of the ratio was determined by error propagation.

A confocal LabRam HR800 Raman spectrometer (Horiba Scientific, France) was used to study structural changes of the CB samples (n = 6) derived from 30-day experiments at 60 and 90 °C. Raman spectra were excited with a 200 mW diode-pumped solid-state laser (783.976 nm) and detected in the range of 150 and 2,000 cm^{-1} with a spectral resolution of 1.94 ± 0.02 cm^{-1} in the frequency range of interest, which was empirically estimated from the line width of Ne lines. For the measurements, a 100x objective with a numerical aperture of 0.9 and a confocal hole of 1,000 μm was used. The spectrometer entrance slit was set to 100 μm, and a diffraction grating with 600 grooves/mm was used to disperse the polychromatic scattered light onto an electron-multiplier charge-coupled device (CCD) detector. The acquisition time per spectrum was 20 s with two accumulations. The first-order band of a pure silicon standard at 520.7 cm^{-1} was used to calibrate the spectrometer before each measurement. The analysis area covered the edges of the sample. Least-square fitting of an asymmetric Gauss-Lorentz function and a linear background was performed to determine the frequency of the $\nu_1(PO_4)$ fully symmetrical stretching band of apatite near 960 cm^{-1} and its width, given as the full width at half maximum (FWHM). Then, the width was corrected for finite slit width effects (Tanabe & Hiraishi, 1980). This correction was also applied to all reference data based on the spectral resolution given in the respective publication. For more details about the fitting procedure the reader is referred to Barthel et al. (2020), Geisler & Menneken (2021), Weber et al. (2021), and Kral et al. (2022; chapter 3).

4.4 Results

4.4.1 Oxygen isotope composition of the experimental solutions

Stable oxygen isotope analysis was performed on stock and experimental solutions, the results are summarized in Table 4.2. The FW and SW stock solutions were initially enriched with ^{18}O and yielded $\delta^{18}O$ values of 5,430 ± 19 ‰ and 5,640 ± 123 ‰, respectively. After the termination of the experiments, the $\delta^{18}O$ values of the FW solutions were about 5 to 10 % lower than their initial value (Table 4.2). In the SW solution from the 90 °C experiment, the $\delta^{18}O$ value was reduced by about 9 %, while it increased by about 3 % in the 60 °C experiment (Table 4.2), which is assumed to represent an outlier. In any case, the reduction in the $\delta^{18}O$ value suggests that some oxygen isotopic exchange reactions between bone and solution have taken place. In contrast, the FWS stock solutions were not enriched with ^{18}O and had a negative $\delta^{18}O$ value of -5.47 ± 0.10 ‰ (Table 4.2).

In these experiments, the only source for ^{18}O was the dissolving CHP in the sediment, and ^{18}O should mainly be bound to the dissolved aqueous phosphate species since the oxygen isotope exchange between water, and aqueous phosphate is slow under the experimental conditions (Lécuyer et al., 1999; O'Neil et al., 2003; Zazzo et al., 2004). In addition to experiments with CB and sediment, complementary experiments only with the stock solution and the sediment were carried out to determine the interaction between ^{18}O-doped sediment and the experimental solution. All FWS solutions from the 60 and 90 °C experiments are characterized by δ^{18}O values that are slightly but statistically significantly larger than those of the stock solution, with the largest changes observed for the 90 °C experiment (Table 4.2). This shows that ^{18}O-doped CHP dissolved, and little O-exchange between the ^{18}O-labelled phosphate and the solution occurred. However, the final ^{18}O enrichment was only about one-sixth of the enrichment in the FW and SW experiments.

Table 4.2 | Oxygen isotope composition of stock and experimental solutions.

Sample	**δ^{18}O (‰)**	**± 2σ (‰)**	**$\Delta(\delta^{18}$O) (%)**	**^{18}O/^{16}O**	**± 2σ**
Stock solution FW	5430	19		0.0128922	0.0001700
FW, 60 °C	4853	589	–10.63	0.0117353	0.0055047
FW, 90 °C	5180	66	–4.60	0.0122465	0.0006077
Stock solution SW	5640	123		0.0133132	0.0010508
SW, 60 °C	5804	1	2.91	0.0136420	0.0000105
SW, 90 °C	5170	276	−8.33	0.0123709	0.0025035
Stock solution FWS	–5.47	0.10		0.0019940	0.0000002
FWS, 60 °C	–4.66	0.22	14.81	0.0019957	0.0000004
FWS, 90 °C	–3.00	0.01	45.16	0.0019990	0.00000002
FWS, 60 °C (without bone)	–5.38	0.30	1.65	0.0019942	0.0000004
FWS, 90 °C (without bone)	–4.30	0.04	21.39	0.0019964	0.0000001

FW = freshwater, SW = seawater, FWS = freshwater plus sediment

4.4.2 Oxygen isotope distribution in altered cortical bone

The ^{18}O/^{16}O distribution in the pristine CB sample and the CB samples exposed for 30 d at 60 and 90 °C to FW, SW, and FWS solutions were imaged by nanoSIMS. The ^{18}O/^{16}O values are given in Table 4.3. The average ^{18}O/^{16}O determined from the pristine CB sample is 0.002358 with a 2-sigma precision of ± 0.9 %, which, however, represents the Poisson counting error only and should thus be considered an internal error (Table 4.3). This value is significantly outside the range of the oxygen ratio in natural waters between 0.00191 to 0.00219 (de Laeter et al., 2003). It also differs significantly from those obtained from the center of the experimentally altered samples, which are assumed to be not altered. This assumption is reasonable considering that alteration should have increased the ^{18}O-^{16}O ratio as the solutions were heavily enriched in ^{18}O. It follows that the large scatter indicates additional sources of errors, which are most likely related to different sputtering conditions under different sample orientations and on different days. A weighted average ^{18}O/^{16}O of 0.00185 and an empirical 2-sigma standard error of ± 0.00078 were obtained from these measurements (Table 4.3). Thus, ^{18}O/^{16}O values larger than about 0.00263 can be considered to reflect a statistically significant ^{18}O enrichment.

Table 4.3 | ^{18}O/^{16}O values extracted from nanoSIMS isotope distribution images.

Sample	**Pixel no.**	**Sample center**		**Pixel no.**	**Reaction rim**	
		^{18}O/^{16}O (ppm)	**± 2σ***		**^{18}O/^{16}O (ppm)**	**± 2σ***
Unaltered control	260,610	2,358.46	21.81		*No reaction rim was observed*	
FW, 60 °C	236,544	1,253.96	4.08			
FW, 90 °C	227,840	1,732.48	6.39			
SW, 60 °C	224,840	1,568.55	4.67			
SW, 90 °C	225,792	2,363.78	4.24			
Weighted average		1,855.45	788.17§			
FWS, 60 °C	244,698	2,837.08	10.76	28,296	6,654.92	13.03
FWS, 90 °C	244,224	5,813.73	6.35	37,036	11,478.23	16.43

(*) Internal counting errors estimated from the total ^{18}O and ^{16}O counts obtained from the nanoSIMS images with the exception of the value marked with § which represents the standard error of the five measurements from the centers of the unaltered, the FW, and SW CB samples. By taking an average, it is assumed here that these measurements all come from areas that have not been altered and thus provide an estimate of the accuracy and the external reproducibility between different samples measured under different sputtering conditions.

The CB samples exposed to ^{18}O-containing FW and SW solutions for 30 d at 60 and 90 °C do not show a difference in ^{18}O/^{16}O between the edges and the center of the bone samples (Figs. 4.2A-D, 4.3A-D). However, along the edges, these samples are enriched with several other elements originating from the solution, including F (Fig. 4.2B, D), U (Fig. 4.2A), and Sr (Fig. 4.2C) as well as Zn, Mg, Lu, and Nd as described and discussed in detail in Kral et al. (2022; chapter 3). In contrast, the nanoSIMS ^{18}O/^{16}O images of the FWS samples show irregular inwardly delimited ^{18}O-enriched domains (Figs. 4.2E, F, 3E, F). Occasionally, the ^{18}O-enriched domains penetrate deeper into the bone along microcracks (arrow in Fig. 2E and F). In agreement with Kral et al. (2021, 2022 see chapter 2 and 3, respectively), this rim is called reaction rim (RR) in the following.

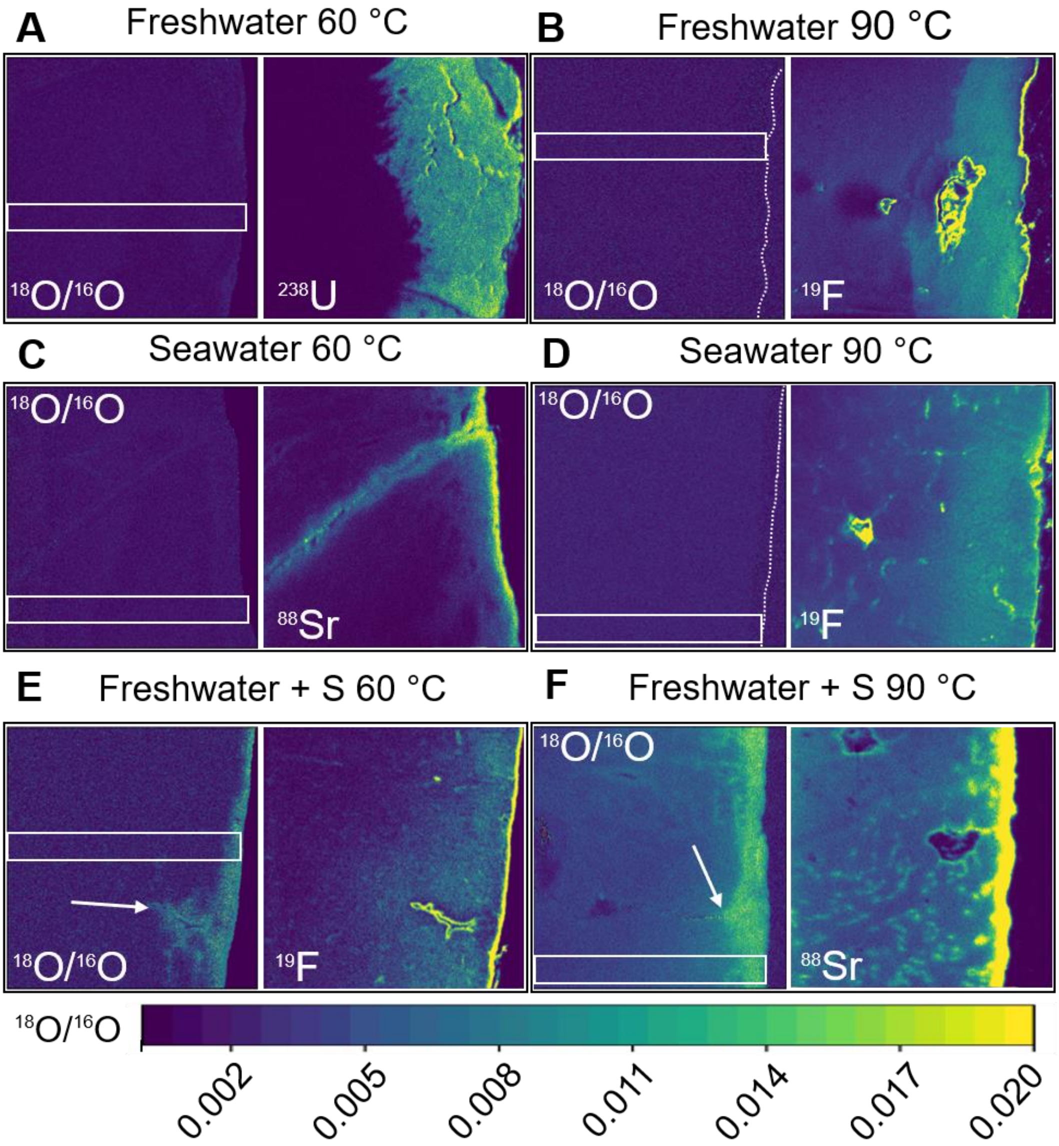

Figure 4.2 | Isotope distribution images obtained by nanoSIMS of CB samples that reacted at 60 and 90 °C for 30 d in **(A, B)** FW, **(C, D)** SW, and **(E, F)** FWS containing ^{18}O-enriched CHP. The images display the isotopic ratio of oxygen at each pixel (0.078 µm) obtained by dividing the ^{16}O and ^{18}O counts of each pixel compared to the isotope distribution of **(A)** ^{238}U, **(B)** ^{19}F, **(C)** ^{88}Sr, **(D)** ^{19}F, **(E)** ^{19}F, and **(F)** ^{88}Sr. The white boxes mark the regions from which nanoSIMS ^{18}O/^{16}O profiles were derived (see Fig. 4.3). The size of each image is 40 x 40 µm^2.

The average ^{18}O/^{16}O calculated from selected areas of the RR is 0.006654 ± 0.2 % for the 60 °C sample (Table 4.3). This value is statistically significantly higher than the ratios measured in the center of the pristine sample (Fig. 4.3E, F). In the 90 °C sample, the ^{18}O enrichment was even more pronounced along the edges and reached far deeper into the CB sample (Figs. 4.2F, 4.3F). The average $^{18}O/^{16}O$ in the sample center and the RR were 0.005813 ± 0.1 % and 0.011478 ± 0.1 %, respectively (Table 4.3), i.e., in this case, even the center of the CB sample is significantly enriched in ^{18}O. It is noteworthy that the F enrichment correlates well with the observed ^{18}O enrichment (Fig. 4.2E).

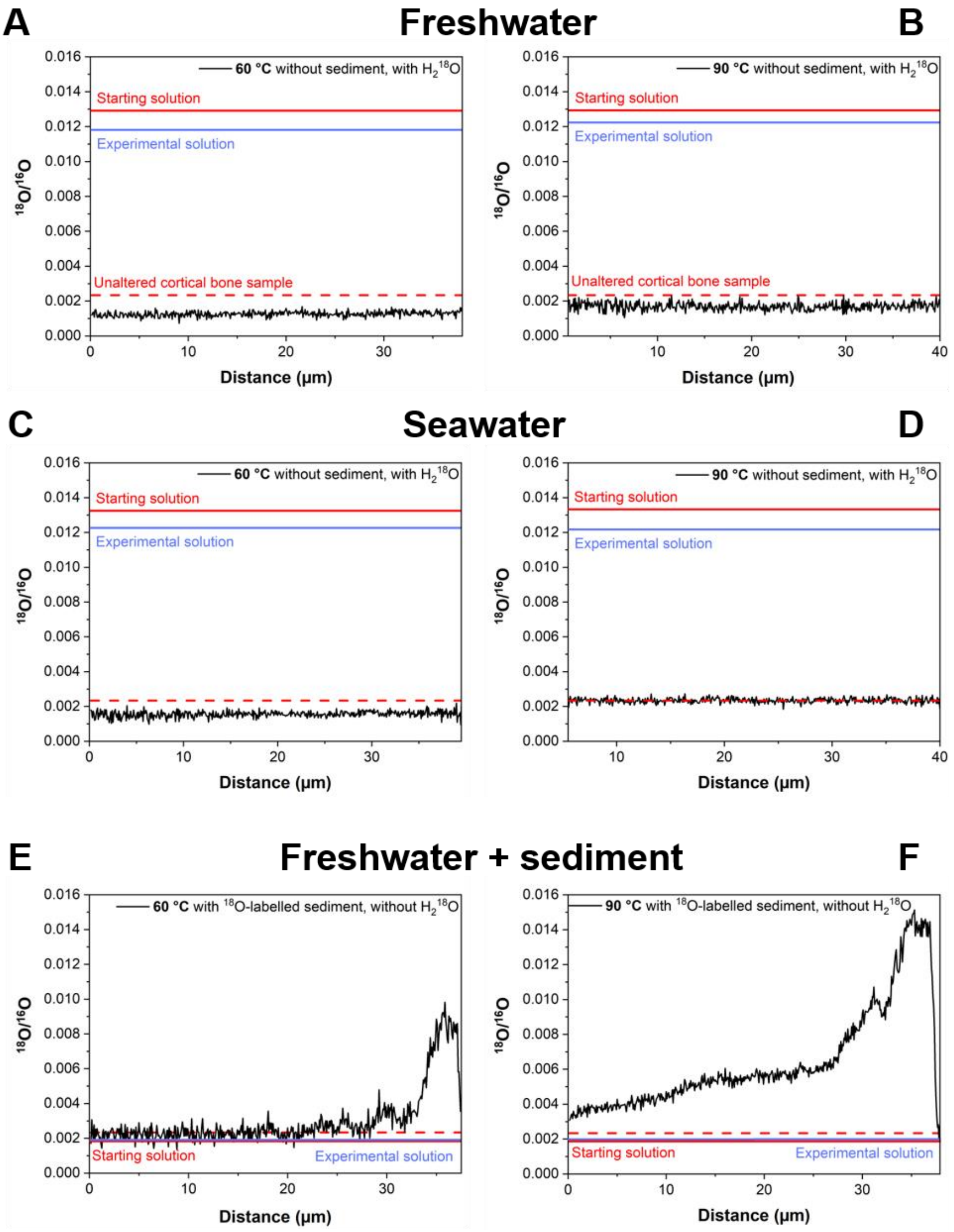

Figure 4.3 | NanoSIMS $^{18}O/^{16}O$ profiles of the CB samples displayed in Fig. 4.2. The $^{18}O/^{16}O$ profiles show the change of the ratio from the edge of **(A, B)** FW, **(C, D)** SW, and **(E, F)** FWS samples towards the center. The $^{18}O/^{16}O$ profiles were derived by integrating the counts of an area (marked as white boxes in Fig. 4.2) of 4 µm in the x-direction and 30 to 38 µm in the y-direction, depending on the thickness of the area covered by resin which was excluded from the plot. The dashed red line marks the $^{18}O/^{16}O$ of the pristine CB sample, while the straight red and blue lines display the stable oxygen isotopic composition of the starting solution and the experimental solution after terminating the experiments.

4.4.3 Mineralogical features of altered bone apatite

Confocal Raman spectroscopy was used to assess possible mineralogical changes associated with the experimental treatment of the CB samples. The bandwidth Γ, given as the FWHM, and the position (frequency ν) of the $\nu_1(\mathrm{PO}_4)$ fully symmetric stretching band are two essential parameters that have previously been used to obtain information on the structure of the bone apatite (Thomas et al., 2011; Dal Sasso et al., 2018; Barthel et al., 2020; Weber et al., 2021; Kral et al., 2022; chapter 3). Figure 4.4 shows a plot of both parameters from the experimentally altered CB samples and reference data from various sources.

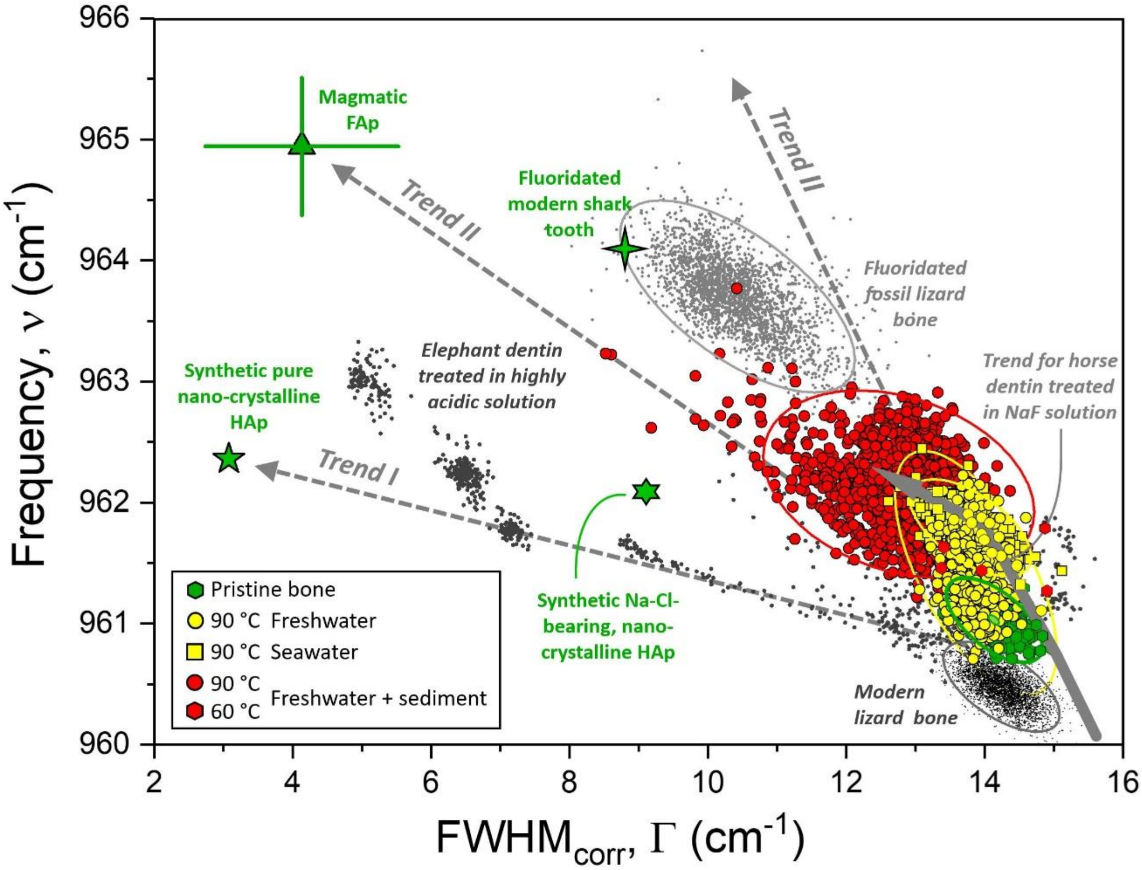

Figure 4.4 | Plot of Raman spectral parameters. The frequency, ν of the $\nu_1(\mathrm{PO}_4)$ band of pristine and altered CB samples as a function of its bandwidth, Γ, compared to various reference data: modern and fluoridated fossil lizard bone (Barthel et al., 2020), modern fluoridated shark tooth and the trend for horse dentin altered in NaF solution (Pasteris & Ding, 2009), magmatic FAp and modern elephant dentin altered in a highly acid, nominal F-free solution at 30 and 90 °C for different durations (Weber et al., 2021), synthetic nano-crystalline, stoichiometric HAp (Asjadi et al., 2019), and synthetic nano-crystalline, Na- and Cl-bearing HAp (Thomas et al., 2011). Trends labeled I, II, and III are explained in the text. Ellipses represent the 95 % confidence limit of the single measurements. However, the small green ellipse on the top of the data from pristine CB represents the 95 % confidence limit of the mean. To assure comparability, all bandwidths were corrected for finite slit width broadening using the given spectral resolution and the equation of Tanabe & Hiraishi (1980).

The Raman spectral parameters from the pristine control sample (*n* = 232) show a distinct variability due to the natural heterogeneity of the CB sample; the $\nu_1(PO_4)$ band position ranges from 960.0 to 961.5 cm^{-1} with an average value of 961.0 ± 0.2 $cm^{-1,}$ and the FWHM lies between 12.7 and 15.0 cm^{-1} with an average value of 14.1 ± 0.3 cm^{-1}. The 95 % distributions of single measurements and their mean are given in the diagram by green ellipses. The length axis of these ellipses, representing the reduced major axis regression, has a slope $d\nu/d\Gamma$ of – 0.40 and, as such, points to the position of magmatic FAp (Trend II in Fig. 4.4). It is noteworthy that the reduced major axis slope agrees very well with the slopes observed for both modern and fluoridated fossil lizard bones (Barthel et al., 2020). By looking at the frequency versus bandwidth relationship for the RR data of the CB samples altered for 30 d at 90 °C (colored in yellow respectively red in Fig. 4.4), it is instantly noticeable that in all experiments, the nano-crystalline bone apatite matrix must have been significantly altered, which is reflected by a clear shift of the $\nu_1(PO_4)$ band to higher frequencies (wavenumbers) and to lower bandwidths compared to the data from pristine CB.

The data of all altered samples together define a fan-shaped region. In contrast, the data from the RR from the CB of the samples of the FWS experiments (red symbols, *n* = 1139) are clearly distinguishable from those from the RR from the CB samples of the SW (yellow squares, *n* = 405) and FW experiments (yellow circles, *n* = 450). They define a broad trend that evolves towards higher wavenumbers and decreasing bandwidths. Towards lower frequencies, the spread of the data is limited by Trend II, connecting the pristine bone apatite and magmatic FAp. Moreover, it appears that the data from experiments without sediment and one part from the experiment with sediment follow a steeper linear array with a slope $d\nu/d\Gamma$ of about – 1.2 (Trend III in Fig. 4.4) that runs parallel to the initial trend defined by horse dentin that had experimentally been fluoridated in NaF solution (Fig. 4.4; Pasteris & Ding, 2009).

In contrast, the data from the RR of the 90 °C FW sample only show, on average, a significant shift towards higher frequencies but with a significant overlap with data from the pristine CB, as already reported by Kral et al. (2022; chapter 3). The reduced major axis slope, i.e., the orientation of the length axis of the confidence ellipse, is comparable to that given by Trend III (Fig. 4.4). The Raman frequencies of the $\nu_1(PO_4)$ mode obtained from the RR of the SW sample are significantly higher than those from pristine bone. In contrast, on average, the $\nu_1(PO_4)$ bandwidth shows only a minimal decrease, i.e., the data are mainly blue-shifted. Their 95 % confidence ellipse is oriented almost parallel to those of the pristine

CB. A similar picture emerges for the Raman data from the RR formed at 60 °C in FW solution, which are not shown here but reported in Kral et al. (2022; chapter 3). However, this data is characterized by an even larger bandwidth, on average, than that of pristine CB, resulting in a positive slope tie-line between pristine and altered CB on the frequency versus width plot.

4.5 Discussion

This study applied a novel experimental approach using an oxygen isotope tracer to investigate potential bone mineralization during early diagenesis. Two types of experiments were performed with a FW solution with and without initial ^{18}O enrichment and for further comparison with a SW solution highly enriched in ^{18}O. However, the non-enriched FW solution was in contact with synthetic sediment containing ^{18}O-enriched CHP, which provided a continuous source for ^{18}O. The rationale here was to use a tracer to distinguish between bone apatite recrystallization and new apatite mineralization. Aqueous PO_4 only slowly exchanges oxygen with water at the temperature and duration of the experiments ($t_{1/2}$ = 380 d at 75 °C and 23 d at 100 °C, Lecuyer et al. 1999), in particular when considering that the residence time of PO_4 in solution is limited to clearly less than 30 d since it was continuously added to the solution by the dissolution of CHP. Therefore, recrystallization of bone apatite in an ^{18}O-labeled but PO_4-free solution is not expected to be reflected in a significant enrichment of ^{18}O, although some exchange via the OH groups can occur if they are not replaced by F. However, if aqueous ^{18}O-labelled PO_4 from the dissolving CHP precipitates as new apatite inside the CB, a significant enrichment of ^{18}O in altered CB would be expected. In fact, this is precisely what was observed.

The most striking finding is the detection of a strong enrichment in ^{18}O in the 10 to 40 µm thick RR of CB treated at 60 and 90 °C in a solution with an artificial sediment added that included ^{18}O-doped CHP (Figs. 4.2E, F, 4.3E, F). The $^{18}O/^{16}O$ in the outer part of the 90 °C FWS samples locally reached a maximum ratio of 0.0274 with an average of 0.011478 ± 0.14 %, which is significantly higher than the VSMOW ratio of 0.002005 ± 0.02 % (Baertschi, 1976). The ^{18}O enrichment in the 60 °C FWS sample did not extend further than a maximum of 10 µm into the center of the CB (Figs. 4.2E, 4.3E). However, the nanoSIMS isotope distribution image clearly shows that in the 90 °C sample, areas 40 µm away from the surface were significantly enriched with ^{18}O (Figs. 4.2F, 4.3F), indicating a strong temperature influence of phosphate transport into CB. In stark contrast, no significant ^{18}O

enrichment in CB was detected from experiments without sediment, although the FW and SW solutions were highly enriched with ^{18}O, and the outer edges of the CB samples are characterized by significant chemical modifications (Fig. 4.2A-D). Thus, an atomic exchange of the PO_4 molecule oxygen atoms against ^{18}O from the aqueous FW and SW solution did not occur. PO_4 is a relatively inert molecule due to strong P-O bonds (Winter et al., 1940) and quite resistant against O-exchange with H_2O molecules at Earth surface temperatures of up to 70 °C and neutral to alkaline pH conditions (Winter et al., 1940; Lécuyer et al., 1999; O'Neil et al., 2003; Chang et al., 2021) – the latter applied to all three types of solution (Kral et al., 2021; chapter 2). Generally, this observation demonstrates that in the FW and SW experiments, the incorporation of elements from the solution was uncoupled from the incorporation of ^{18}O. It follows that the observed ^{18}O enrichment in CB from the FWS experiments is unequivocal experimental evidence for the mineralization of CB through newly grown authigenic apatite, especially in the RR.

The Raman spectra did not deliver any evidence for the formation of other mineral phases than apatite in the altered CB samples, for example other calcium phosphates or fluorite. However, the relationship between the frequency and bandwidth of the $\nu_1(PO_4)$ mode of bone apatite indicates that significant structural and/or mineralogical changes must have occurred. From a physical point of view, it is to be expected that the frequency and lifetime (represented by the bandwidth) of an excited atomic vibration in a disordered, nanocrystalline solid solution such as bone apatite are negatively linearly correlated with each other. At the same time, the absolute values and the slope depend on structural properties such as defect density, substitution mismatch, and crystallite size. For instance, the recrystallization of bone apatite in an F-free solution should result in a trend directed towards stoichiometric, pure nanocrystalline HAp. Such a trend has indeed been observed recently by Weber et al. (2021), who altered modern elephant dentin for up to 63 d in a nominally F-free, highly acidic solution at 30 and 90 °C (Fig. 4.4). Some Raman data from reacted dentin define a linear trend with a relatively flat slope $d\nu/d\Gamma$ of about – 0.14 (labeled Trend I in Fig. 4.4) before bending towards higher frequencies. These authors explained the observed kink away from Trend I to higher frequencies by the release of F from the Teflon© reactor at higher temperatures and durations, resulting in the increasing formation of an F-bearing apatite phase, i.e., a shorter average P-O bond length which is reflected by a higher $\nu_1(PO_4)$ frequency (e.g., Penel et al., 1997; Lanfranco et al., 2003; Thomas et al., 2007, 2011). In a previous study, Kral et al. (2022; chapter 3) have shown by nanoSIMS and EMPA imaging that the RR of both FW and SW samples are enriched with F (Fig. 4.2B, D, E). When interpreting the Raman data from bone material, however, it should be kept in mind that due to the nanocrystalline nature of the apatite phase(s), a Raman spectrum represents a mixed spectrum from thousands of nano-crystallites and consequently the derived Raman parameters. In all three experiments, F was initially present in a solution with a concentration of 5 mg/L, potentially allowing for the crystallization of F-bearing apatite. And indeed, the observed shift of the $\nu_1(PO_4)$ mode frequency to higher values in altered CB compared to those from the pristine reference sample clearly indicates the formation of F-bearing apatite. However, this frequency shift is only accompanied by a little reduction of the measured bandwidth, which has also been observed during the experimental and *in situ* monitored fluoridation of horse dentin (Pasteris & Ding, 2009). These as well as other authors (Ren et al., 2019) suggested that fluoridation occurred by an interface-coupled dissolution-reprecipitation process during which bioapatite nano-crystallites partially dissolved stoichiometrically and released Ca and P to the F-bearing solution, which caused the supersaturation and precipitation of a FAp-HAp solid solution from an interface fluid film, gradually replacing the original bioapatite pseudomorphically. The process is driven by the difference in solubility between bioapatite and highly insoluble FAp. The formation of several nanometer-thick surface layers of FAp on bulk HAp has indeed experimentally been observed but was attributed to kinetically-controlled diffusion of F from the HAp surface into the crystal (Lin et al., 1981; Müller et al., 2010) or the result of an adsorption mechanism (e.g., Sternitzke et al., 2012; Mosiman et al., 2021). However, such an interface-coupled replacement process has been shown for many solid solution-aqueous solution systems (SSAS) to be favored over diffusion-controlled processes, particularly at low temperatures (Putnis, 2002; Prieto, 2009; Putnis et al., 2009; Ruiz-Agudo et al., 2014). In any case, the fluoridation process leads to a composite material on the nanoscale with an F-rich rim and a bone apatite core. It is well conceivable that the new interface formed between the two nanocrystalline apatite phases may cause additional band broadening, which will decrease once FAp fully replaces the bone apatite nano-crystallites. In fact, the kink of the fluoridation trend for dentin towards decreasing bandwidth (Fig. 4.4), as observed by Pasteris & Ding (2009), may be explained by the complete replacement of bone apatite by FAp. Whereas the Raman parameters from experiments without sediment follow the steeply-sloped Trend III, the data from the FWS experiments with PO_4-delivering sediment seem to split into two groups (red symbols in Fig. 4.4). It, therefore, appears to be obvious to link these two groups, following Trends II and III, to (i) variable fractions of a newly crystallized, nanocrystalline and F-bearing apatite and (ii) recrystallized and thereby fluoridated nanocrystalline bone apatite, respectively.

Most of the original bioapatite in fossil bone has been replaced by a secondary, more stable apatite phase of larger crystallite size - generally CO_3-FAp (Berna et al., 2004; Trueman et al., 2004; Piga et al., 2016). It is widely assumed that bone recrystallization and mineralization occur during the early stages of fossilization (Nielsen-Marsh & Hedges, 2000; Trueman et al., 2004, 2008; Kohn, 2008). However, it is still unclear how quickly bone recrystallization begins *post mortem* and what are the specific processes as there are, e.g., diffusional ionic exchange, surface adsorption, and uncoupled and an interface coupled dissolution-recrystallization (Neuman & Mulryan, 1951; Kelly & Bassingthwaighte, 1977; Fernández-Seara et al., 2002; Marenzana et al., 2005; Trueman et al., 2008; Kohn & Moses, 2013; Keenan & Engel, 2017; Konrad-Schmolke et al., 2018; Renard et al., 2019).

In a rare study, the O-exchange between $(PO_4)_{aq}$ and H_2O, the compositional stability of the CO_3 ($\delta^{13}C$, $\delta^{18}O_C$) and PO_4 ($\delta^{18}O_P$) group in bioapatite was investigated under biotic and abiotic conditions by exposing bone and tooth powders to ^{13}C- and ^{18}O-labeled aqueous solutions (Zazzo et al., 2004). It was found that chemical alteration, i.e., rapid incorporation of ^{13}C and ^{18}O into the bioapatite phase of bone either by isotopic O-exchange or the formation of secondary minerals, starts only a few days after death, even before structural modifications become apparent. PO_4 appears to be more resistant against O-exchange under inorganic conditions than carbonate, which was reversed under microbial conditions. It was suggested that such exchanges would also occur in nature within a few days after death, which basically agrees with the observation, that chemical modifications start before changes in the bone histology occur (Kral et al. (2021, 2022, see chapter 2 and 3, respectively). Based on short-term aqueous alteration experiments, these authors showed that element uptake and incorporation into bone occured within the first few days of exposure to an external fluid, while the CB microarchitecture remained relatively unchanged. However, the data presented here can confirm only partially the second assumption regarding the O-exchange resistance of PO_4 and CO_3. Zazzo et al. (2004) stated that under inorganic conditions, as present in the current study, CO_3 is less resistant against O-exchange than PO_4 due to weaker C-O bonds. The present study showed that the isotopic O-exchange between aqueous solution and bone apatite was insignificant even after four weeks at 90 °C in both FW and SW solutions. This is because PO_4 is initially released during the congruent dissolution of bone apatite and then reprecipitated as new, possibly F- and CO_3-bearing apatite along an inwardly moving replacement front, producing pseudomorphs of the original nano-crystallites. However, data from the present study does not show evidence for ^{18}O-enrichment in four weeks under high-temperature conditions (90 °C), which should accelerate the processes. Thus, the nanoSIMS data show indirectly that no substantial ^{18}O isotopic exchange did not occur in PO_4, CO_3, and OH. An explanation for the different results may be that Zazzo and colleagues (2004) used bone and tooth enamel powders, while Kral et al. (2021, 2022, see chapter 2 and 3, respectively) used intact CB samples. The powders have a much larger surface-to-volume ratio than intact bone samples, artificially increasing the oxygen isotope exchange rate, which is a surface-driven process. This result implies that the O-exchange between aqueous solutions and bioapatite is distinctly slower than previously assumed if external PO_4 and probably CO_3 sources are not present. External PO_4 can be present in the embedding environment, either as an already dissolved ion in the diagenetic fluid or in a solid form in the sediment, dissolving over time. In either scenario, the *post mortem* incorporation of external PO_4 occurs rapidly and thus distinctly accelerates bone fossilization. Consequently, the oxygen isotope signature is altered rapidly due to the formation of newly grown FAp, at least in the RR of the CB.

4.6 Conclusion

The *in vitro* alteration experiments using mm-sized CB cylinders at sub-boiling temperatures in aqueous solutions were aimed at determining the phosphate's provenance for bone mineralization. No evidence of newly grown apatite crystallites and oxygen isotope exchange was found in bones exposed to aqueous solutions at low-temperature conditions lacking a sedimentary phosphate source. However, it was demonstrated that uptake of dissolved PO_4 into the bone occurred in the presence of a sedimentary phosphate source, and new FAp began to form. This is evidenced by ^{18}O-enriched PO_4 transfer from sediment to bone and changes in Raman parameters (higher $v_1(PO_4)$ wavenumbers and lower FWHM) in the RR. This indicates that bone started to be rapidly mineralized by new, energetically more favorable, and less soluble FAp within a few weeks after exposure to an aqueous environment with an external PO_4 source. Thus, it is conceivable that the incorporation of external sedimentary PO_4 causes its oxygen isotope signature to be incorporated into the altered bone mineral phase so that in the RR (later possibly throughout the entire bone), a mixture of primary and secondary incorporated PO_4 determines the $\delta^{18}O_{PO4}$ value. An external PO_4 source greatly accelerates the fossilization of the bone, leading to a more rapidly altered oxygen isotope signature than in a diagenetic setting without additional external PO_4. Therefore, a lack of accurate information about the burial and diagenetic environment can bias the interpretations of $\delta^{18}O_P$ values and thus have implications on the reconstruction of, e.g., paleotemperatures or the composition of past environmental waters.

5 Synopsis

The present thesis was designed to study the effect of diagenetic alteration processes on organic and inorganic components of cortical bone from the millimeter down to the atomic scale. Therefore, three different time- and temperature-controlled, *in vitro* bone taphonomy experimental series were performed, followed by an in-depth state-of-the-art analysis of the respective experimental run products.

The introductory chapter describes bone diagenesis and outlines the aims of this thesis. In the second chapter, a comprehensive µCT study is presented. Here, the effect of aqueous alteration on the microarchitecture of the cortical bone samples was characterized and documented in three dimensions before and directly after the experiments. It was concluded that despite slight chemical (reflected as a bright reaction rim) and gravimetric changes, the microarchitecture was generally well-preserved, even under extreme physicochemical conditions. Another important finding was that the most substantial modifications occurred in freshwater than seawater solutions. Thus, the composition of the aqueous solutions controlled the changes in the organic and inorganic phases the most. The visualization of the entire bone structure was used to systematically identify areas where changes occurred. Based on the µCT results, chemical and mineralogical investigations on the micrometer down to the atomic scale were performed and are presented in the third chapter. It was found that massive elemental uptake from the solution into the bone sample occurred within the first few days of the experiment. This was reflected by different enrichment patterns predominantly in the reaction rim of the cortical bone, however, with a slight time delay.

The most significant finding from this study is that element incorporation is controlled by transport and reaction processes instead of diffusion processes, as previously assumed. For instance, such reaction and transport processes led to deeper penetration of magnesium into the bone in less time. The third chapter shows that after only a few weeks, the reaction rim areas of cortical bone samples were mineralized with newly grown fluorapatite. These were exclusively derived from experiments with an external ^{18}O-labeled phosphate source. Bones derived from the control experiments without sediment were not mineralized by newly formed fluorapatite crystallites. It follows that apatite cannot be recrystallized only with calcium and phosphate derived from the solution within this short time frame. This changes our understanding of oxygen isotope exchange between bioapatite and aqueous solutions during early diagenesis.

5.1 Implications

From the results of this thesis, new insights into the initial process of bone alteration emerged and can be explained using the example of the freshwater experiment (Fig. 5.1):

Overall, the initial bone alteration process can be divided into three main phases, which initially proceed according to a specific sequence (Fig. 5.1A-C). However, these phases overlap and occur simultaneously to a certain extent from a certain point on.

The experiments showed that interactions between both started immediately after immersing the cortical bone samples in the solution. The solution penetrated the cortical bone samples via the cortical canals, (micro-)cracks, and micro- and nano-porosity within a single day (Fig. 5.1A). Collagen-solution interaction caused a temporary swelling of the collagen fibers for about one day, resulting in a significantly decreased pore space. Dissolved ions were transported and distributed into the cortical bone depending on their physicochemical properties, thus initiating element uptake (Fig. 5.1B).

The observed formation of microcracks enhanced solution penetration and thus bioapatite dissolution. Within the first three days, the pore fluids had already reached element-specific saturation levels and the incorporation of elements into the cortical bone occurred in steps of different velocities. First, fast transport of solution and dissolved elements led to the distribution of specific elements into and partially throughout the entire cortical bone sample, e.g., Sr, Mg, or Zn. The elements with high adsorption coefficients like Nd, Lu, or U were solely concentrated in the reaction rim and likely first bound by adsorption onto collagen fibers and crystallite surfaces (Fig. 5.1B).

Over time and with increasing temperature, collagen is degraded, reflected by a distinct weight loss in the samples. Thereby, on the one hand, elements bound to collagen peptide chains were released into the pore fluid. On the other hand, bioapatite crystallites were exposed to the pore fluid even more. Apatite dissolution was enhanced, but recrystallization processes were also facilitated due to saturation or supersaturation in pore fluids (Fig. 5.1C). In the reaction rim, a transition from a purely transport-controlled process (^{142}Nd) to a transport-reaction process (^{175}Lu) was observed, whereby the reactive part is more dominant the larger the atomic number (^{238}U). Instead of diffusive processes, these processes were suggested to be responsible for element incorporation. Diffusion is a much slower process, which is more likely to be of importance in later stages of bone diagenesis.

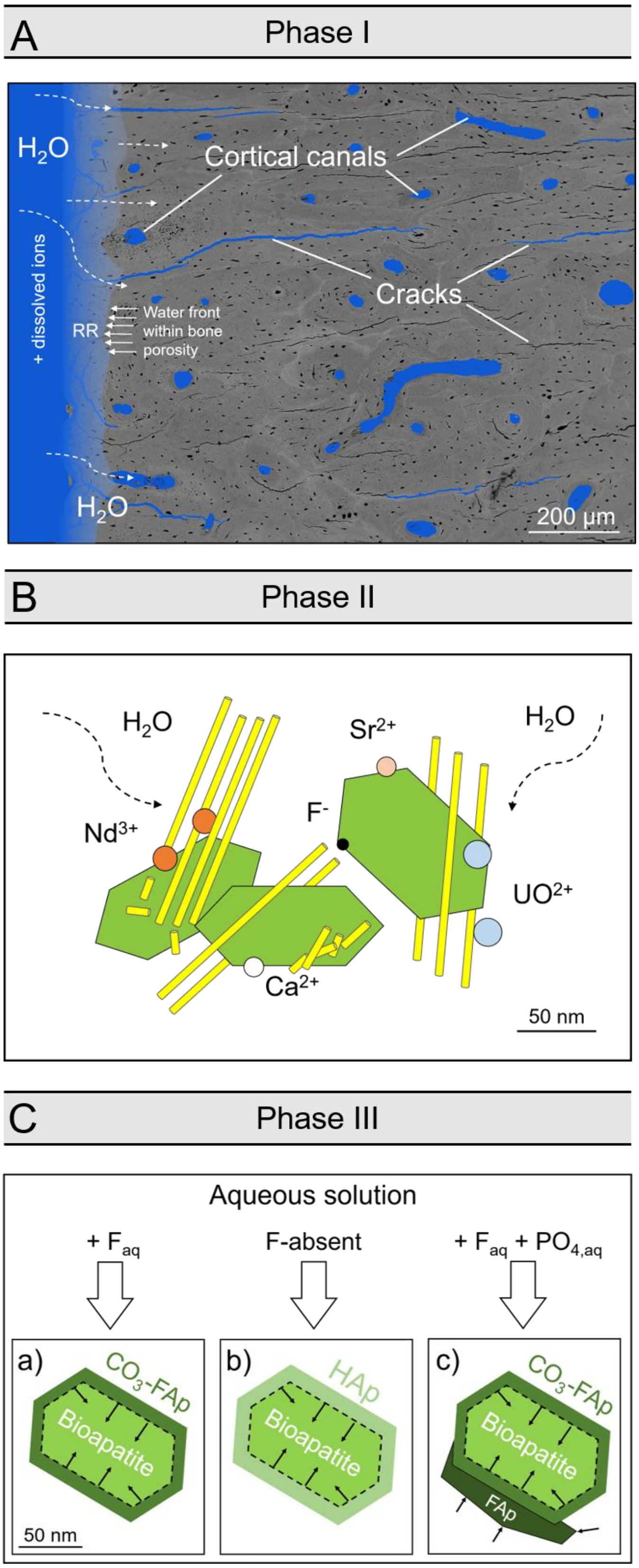

Figure 5.1 | Schematic illustration of the three main phases of the early diagenetic bone alteration process. **(A)** illustrates the fluid transport into bone via (micro-)cracks, cortical canals, and micro- and nano-porosity. **(B)** Phase II shows the adsorption of dissolved ions onto bioapatite crystallite surfaces and collagen fibers while apatite dissolution and collagen degradation occur. Collagen is colored in yellow and bioapatite in green. The circles represent different dissolved ion species. **(C)** shows the apatite and collagen replacement ± new apatite growth as well as the incorporation of adsorbed elements in the new apatite. RR = reaction rim. Arrows indicate the direction of mass transport.

At the same time, a dissolution-transport-reprecipitation process, for instance, operating during Ostwald ripening, led to the relocation of calcium and phosphate from the rim area further into the cortical bone. This is reflected by filling and subsequent disappearing of the microcracks, which cannot be traced after 21 to 30 days, implying the formation of authigenic apatite. In the reaction rim, bioapatite nano-crystals re-equilibrate through a temporally- and spatially-coupled dissolution-reprecipitation process, ultimately leading to the formation of carbonated fluorapatite (Fig. 5.1.C-a, c) or hydroxylapatite if fluorine is absent (Fig. 5.1.C-b).

At this point, it must also be differentiated between freshwater and freshwater plus sediment experiments. In the freshwater plus sediment experiments, new fluorapatite crystallites are additionally formed from ^{18}O-labelled phosphate derived from the sediment source (Fig. 5.1-c). In contrast, it is suggested that only carbonated fluorapatite was formed in freshwater experiments due to dissolution-reprecipitation processes, but no new fluorapatite or hydroxylapatite crystallites (Fig. 5.1C-a, b). Thus, in both cases, the chemical and structural modification of the organic and inorganic phases of the cortical bone samples was already active directly after exposure to an aqueous solution, while only under the presence of a sedimentary phosphate source, the mineralization process was significantly accelerated, and the oxygen isotope signature of the bone was rapidly modified.

The modifications in seawater samples cannot be easily identified because of the chemical conditions, i.e., the pH was in the range of the recrystallization window, in which dissolution and reprecipitation are balanced. Thus, the weight loss might have been counterbalanced by apatite recrystallization. This assumption is supported by the increased, but finally, after 30 days, decreased porosity. Therefore, in this model, the focus was placed on the freshwater series.

Methodological implications also emerged from this study. Generally, a practical result of the experiments and multi-method approach using analytical techniques with different resolutions was to show that it is crucial to not only rely on a single method. Due to the fine hierarchical structure and thus the chemical composition of cortical bone, it is possible only to a limited extent to detect chemical modifications in detail using EMPA, LA-ICP-MS, or any other methods with a spot size in the µm range. In such a case, every measurement covers much larger unaltered than altered areas, thus leading to mixed analysis and average signatures, concentrations, or distribution patterns, which has serious implications for data interpretation. Furthermore, combining imaging and quantitative techniques was also very useful. For instance, it was observed that large numbers of microcracks were formed within a few days after the bone's exposure to the solution, thereby enhancing the solution penetration and element transport. However, after 21 to 30 days, most microcracks were sealed again without showing significant differences in bone composition, thus allowing the identification of the microcracks, probably due to the filling by authigenic apatite which, however, can only hardly be differentiated from the original bioapatite phase. Collagen hydrolysis and recrystallization began quickly after the cortical bone samples got into contact with the aqueous solution, leading to the dissolution of bone apatite at one place and the recrystallization at another (e.g., via Ostwald ripening), but without changing the overall morphology significantly (pseudomorphosis). This has serious implications for any research field focusing on paleo-reconstruction.

It is usually assumed that the inner parts of cortical bone are less altered and modified by diagenetic processes; however, even if the bone looks intact and well-preserved, it is does not necessarily mean that it is. The results presented here show that relying only on a single method for interpretation would have led to a false impression. In addition, the approach of investigating samples qualitatively before quantitative analysis was only rarely used, even though it would provide an overview of the spatial distribution of elements/isotopes and enable identifying representative areas for subsequent quantitative analysis. This is of particular importance as with increasing resolution of quantitative methods, the analytical volume is decreasing significantly. The risk of analyzing unrepresentative areas and, therefore, losing important information or coming to incorrect conclusions is high.

5.2 Limitations of the study

In the following, it is briefly discussed what could have been done better in retrospect.

Initially, it was not planned to perform such a comprehensive quantitative µCT study, so less attention was paid to specific details. One shortcoming was that no phantom was used as an internal standard during the scans – this would have allowed a more precise comparison of different samples. However, in the case of the present study, this did not matter too much because the same bone sample was characterized before and after the experiments. Thus, each sample was its own reference and allows for internal comparison. Future studies should consider the use of a phantom as it facilitates the analysis. In addition, the scans were performed using an isotropic voxel size of 3 µm so that canaliculi could not be resolved. Therefore, higher voxel and spatial resolutions would be desirable.

Moreover, the elemental composition of the cortical bone samples should initially be determined by LA-ICP-MS, EMPA, and APT, which, however, worked only to a limited extent for several reasons. On the one hand, the reaction rim was only a few µm thick, so the beam size should not be too large (<5 µm); on the other hand, the samples were susceptible to high-energy electron beams or high laser intensities because of their high organic content and porosity. However, the beam intensity has to be increased to analyze a sufficient volume at such a small beam diameter. In the present case, this resulted in the burning of the samples and thus a strong distortion of the elemental composition, especially for the light elements. For example, the total values of the quantitative electron microprobe analysis varied between 43 and 120 %. For APT analysis, several cones from the reaction rim area of three samples were prepared. However, most of them collapsed during the measurement. Only the signal from only a single cone was strong enough, although but still weak, to be evaluated. Additionally, the applied currents varied strongly, which led to the formation of so-called "fir tree" artifacts. The obtained calcium and phosphorus concentration patterns were anti-correlated; thus, no conclusions could be made about whether they represent an apatite or non-apatite phase. There are known difficulties with getting the correct stoichiometry for apatite in APT analyses: for example, the Ca:P ratio is typically measured at around 14:1, as it was here, while the stoichiometric ratio is 5:3.

Furthermore, one problem for which a solution was not yet found was the penetration of the embedding resin into the pore space of the samples due to the low viscosity of the resin and the bone’s porosity. Here, Technovit® 5071 was used, an organic methyl methacrylate-based resin that did not affect the nanoSIMS and EMPA measurements. However, it did affect the Raman measurements, because the Raman signal from the penetrated resin overlapped or caused shifts of the bone Raman bands. Although the outermost reaction rim areas were concerned, the results were not significantly affected or distorted, because specific Raman bands characterized the infiltrated resin. This allowed the affected area to be precisely delineated and these spectra were then sorted out. Nevertheless, an approach should be found to embed the samples without allowing the resin to penetrate the pore space, especially if the interaction between aqueous solutions and the organic components of the bone is to be studied.

Another unforeseen problem that affected the Raman measurements was the composition of the experimental solutions. Although the composition of the experimental solutions led to unexpected but important findings, it also hindered specific investigations. For instance, the added neodymium acted as luminescence centers in minerals, thus leading to strong photoluminescence signals in the Raman spectra with two maxima at 866 and 872 nm, which were precisely in the wavenumber range of the collagen components. This made it almost impossible to investigate whether the Raman spectroscopic parameters of these particular bands changed under differing experimental conditions. Thus, in this study, Raman spectroscopy could not be used to conclude the change in the organic phase as initially planned.

5.3 Outlook

The following are some ideas and suggestions for future studies that have emerged from this dissertation to be considered in future studies:

- As mentioned earlier, quantitative µCT measurements would benefit greatly from using a phantom. Moreover, it would probably be worthwhile to perform measurements on a high-resolution synchrotron beamline with a voxel size of, e.g., 1 x 1 x 1 µm. In addition, small markers could be placed on each sample to facilitate spatial comparison before and after the experiments. This could, for example, allow a direct comparison of the changes in the cortical canal network in three dimensions.
- The degradation or preservation of collagen and the underlying processes still raise some questions and could only partially be answered in this study for the reasons already discussed. Therefore, it is here proposed to perform the experiments under similar conditions as in the present studies. However, the freshwater solutions should not contain rare earth elements, which could act as luminescence centers in minerals, thereby impeding or even preventing the analysis of collagen bands by Raman spectroscopy.
- The possibility of analyzing organic degradation products in cortical bone samples by MALDI-TOF MS and experimental solutions by HPLC should be investigated.
- The preservation or dissolution of bioapatite is strongly dependent on local pH conditions, especially during early diagenesis. To allow bone preservation, it is assumed

that a pH window between 7.6 and 8.1 at 25 °C must be present for balanced dissolution and re-precipitation reactions to occur. However, the exact limiting conditions are unknown, and further research on this aspect is needed.

- *In vitro* taphonomy experiments of biogenic apatite in isotope-enriched tracer solutions under conditions similar to those in the present study would be of great interest. For example, whether the experimentally formed cracks are filled by authigenic or newly formed apatite could be investigated. For this purpose, isotopically labeled calcium could be added to the solution to distinguish the source of the calcium. In addition, it would be imperative to know whether the enrichment of Mg, Sr, and Zn in the cortical canal network detected by nanoSIMS significantly affects the isotopic signature of the sample.
- Another intriguing point is that the observations made so far clearly show that the uptake of Sr, U, Nd, and Lu is relatively rapid and occurs both along a transport-reaction front and the percolating cortical canal network. However, it is still not known whether these elements are precipitated as independent phases, incorporated into the bioapatite lattice, or bound by adsorption onto crystallite surfaces or collagen. To further explore these questions, it could be beneficial to perform measurements with a synchrotron μXAS beamline for three-dimensional chemical and structural imaging with an isotropic spatial resolution of 1 μm or less.
- The major limitation of the experimental setup was that the bone taphonomy studies were performed *ex situ*. Therefore, it was not possible to study the experimental solutions as well as bone samples until the experiments were completed. Furthermore, both the experimental solutions and bone samples had cooled to room temperature or dried, respectively. This experimental approach interrupts the processes taking place and can lead to chemical and structural changes in the mineral or organic phases as well as phase precipitation from the pore solution. In addition, conventional isothermal *ex situ* experiments require using a new sample for each time step. These limitations make it difficult to reliably link macroscopic observations to temperature, time, and sample properties, especially for bones with heterogeneous structure and composition. As a result, it is challenging to obtain detailed and precise information about the structural and chemical changes that occur during the aqueous modification of bone tissue and, more generally, about the mechanisms and time dependence of the individual reaction steps, especially those that occur and change on short time scales (i.e., within a few

hours or less). To identify and reliably quantify the rate-limiting reaction steps, an analytical technique is needed that allows the interaction of bone with aqueous solutions to be studied *in situ* at the micrometer-scale and with a temporal resolution of a few minutes. *In operando* and *in situ* fluid-cell Raman spectroscopy would be such a suitable technique (e.g., Geisler et al., 2019; Lenting & Geisler, 2021).

- It may be worthwhile to further investigate, whether the outermost areas of fossilized cortical bone are affected by the oxygen signature of the depositional environment immediately after death and whether the oxygen signature further inside a fossil cortical bone might be more representative of the long-term diagenetic conditions.

6 References

Abdel-Maksoud, G. (2010). Comparison between the properties of ‘accelerated-aged’ bones and archaeological bones. Mediterranean Archaeology and Archaeometry 10, 89–112.

Agerbaek, M. O., Eriksen, E. F., Kragstrup, J., Mosekilde, L., Melsen, F. (1991). A reconstruction of the remodelling cycle in normal human cortical iliac bone. Bone and Mineral 1,101-112. https://doi.org/10.1016/0169-6009(91)90039-3.

Amiot, R., Angst, D., Legendre, S., Buffetaut, E., Fourel, F., et al. (2017). Oxygen isotope fractionation between bird bone phosphate and drinking water. The Science of Nature 104:47. https://doi.org/10.1007/s00114-017-1468-2.

Amoroso, A. J., Pope, S. J. A. (2015). Using lanthanide ions in molecular bioimaging. Chemical Society Reviews 44, 4723–4742. https://doi.org/10.1039/C4CS00293H.

Asjadi, F., Geisler, T., Salahi, I., Euler, H., Mobasherpour, I. (2019). Ti-substituted hydroxylapatite precipitated in the presence of titanium sulfate: A novel photocatalyst? American Journal of Applied Chemistry 6, 1–10.

Aufort, J., Gervais, C., Ségalen, L., Labourdette, N., Coelho-Diogo, C., et al. (2019a). Atomic scale transformation of bone in controlled aqueous alteration experiments. Palaeogeography, Palaeoclimatology, Palaeoecology 526, 80–95. https://doi.org/10.1016/j.palaeo.2019.03.042.

Aufort, J., Gommery, D., Gervais, C., Segalen, L., Labourdette, N., et al. (2019b). Assessing bone transformation in late Miocene and Plio-Pleistocene deposits of Kenya and South Africa. Archaeometry 61, 1129–1143. https://doi.org/10.1111/arcm.12471.

Baertschi, P. (1976). Absolute ^{18}O content of standard mean ocean water. Earth and Planetary Science Letters 31, 341–344. https://doi.org/10.1016/0012-821X(76)90115-1.

Bahia, M. T., Hecke, M. B., Mercuri, E. G. F., Pinheiro, M. M. (2020). A bone remodeling model governed by cellular micromechanics and physiologically based pharmacokinetics. Journal of the Mechanical Behavior of Biomedical Materials 104:103657. https://doi.org/10.1016/j.jmbbm.2020.103657.

Balter, V., Blichert-Toft, J., Braga, J., Telouk, P., Thackeray, F., Albarède, F. (2008). U–Pb dating of fossil enamel from the Swartkrans Pleistocene hominid site, South Africa. Earth and Planetary Science Letters 267, 236–246. https://doi.org/10.1016/j.epsl.2007.11.039.

Barfod, G. H., Otero, O., Albarède, F. (2003). Phosphate Lu–Hf geochronology. Chemical Geology 200, 241–253. https://doi.org/10.1016/S0009-2541(03)00202-X.

Barrios-de Pedro, S., Rogers, K. M., Alcorlo, P., Buscalioni, A. D. (2020). Food web reconstruction through isotopic compositions of fossil faeces: Insights into the ecology of a late Barremian freshwater ecosystem (Las Hoyas, Cuenca, Spain). Cretaceous Research 108:104343. https://doi.org/10.1016/j.cretres.2019.104343.

Barry, P. S. I. (1975). A comparison of concentrations of lead in human tissues. British Journal of Industrial Medicine 32, 119–139. https://doi.org/10.1136/oem.32.2.119.

Barthel, J. H., Fougerouse, D., Geisler, T., Rust, J. (2020). Fluoridation of a lizard bone embedded in Dominican amber suggests open-system behavior. PLoS ONE 15 (2):e0228843. https://doi.org/10.1371/journal.pone.0228843.

Beard, B. L., Johnson, C.M. (2000). Strontium isotope composition of skeletal material can determine the birth place and geographic mobility of humans and animals. Journal of Forensic Sciences 45:1049–1061.

Beck-Nielsen, S. S., Greggio, N. A., Hagenäs, L. (2021). Defining a growing and maturing skeleton and its relevance in diseases that affect skeletal growth, such as X-linked hypophosphatemia. International Journal of Rare Diseases & Disorders 4:029. https://doi.org/10.23937/2643-4571/1710029.

Bentley, A. R. (2006). Strontium isotopes: From earth to archaeological skeleton: A review. Journal of Archaeological Method and Theory 13, 135–187. https://doi.org/10.1007/s10816-006-9009-x.

Berna, F., Matthews, A., and Weiner, S. (2004). Solubilities of bone mineral from archaeological sites: the recrystallization window. Journal of Archaeological Science 31, 867–882. https://doi.org/10.1016/j.jas.2003.12.003.

Bernard, A., Lecuyer, C., Vincent, P., Amiot, R., Bardet, N., et al. (2010). Regulation of body temperature by some mesozoic marine reptiles. Science 328, 1379–1382. https: //doi.org/10.1126/science.1187443.

Blake, R. E., Chang, S. E., Lepland, A. (2010). Phosphate oxygen isotopic evidence for a temperate and biologically active Archaean ocean. Nature 464, 1029–1032. https://doi.org/10.1038/nature08952.

Bloebaum, R. D., Skedros, J. G., Vajda, E. G., Bachus, K. N., Constantz, B. R. (1997). Determining mineral content variations in bone using backscattered electron imaging. Bone 20, 485–490. https://doi.org/10.1016/S8756-3282(97)00015-X.

Bloebaum, R. D., Holmes, J. L., Skedros, J. G. (2005). Mineral content changes in bone associated with damage induced by the electron beam. Scanning 27, 240–248. https://doi.org/10.1002/sca.4950270504.

Boanini, E., Gazzano, M., Bigi, A. (2010). Ionic substitutions in calcium phosphates synthesized at low temperature. Acta Biomaterialia 6, 1882–1894. https://doi.org/10.1016/j.actbio.2009.12.041.

Bocherens, H., Drucker, D. G., Billiou, D., Patou-Mathis, M., Vandermeersch, B. (2005). Isotopic evidence for diet and subsistence pattern of the Saint-Césaire I Neanderthal: review and use of a multi-source mixing model. Journal of Human Evolution 49, 71–87. https://doi.org/10.1016/j.jhevol.2005.03.003.

Bocherens, H. (2009). Neanderthal dietary habits: Review of the isotopic evidence. In Hublin, J. J., Richards, M. P. (Eds). The evolution of hominin diets. Vertebrate Paleobiology and Paleoanthropology. Springer, Dordrecht. https://doi.org/10.1007/978-1-4020-9699-0_19.

Boskey, A. L., Robey, P. G. (2013). The Regulatory Role of Matrix Proteins in Mineralization of Bone in Osteoporosis, in: Marcus, R., Feldman, D., Dempster, D.W., Luckey, M., Cauley, J.A. (Eds.), Osteoporosis. Academic Press, Cambridge), pp. 235–255. https://doi.org/10.1016/B978-0-12-415853-5.00011-X.

Boskey, A. L. (2015). Bone composition: relationship to bone fragility and antiosteoporotic drug effects. BoneKEy Reports 4:710. https://doi.org/10.1038/bonekey.2015.79.

Bourgon, N., Jaouen, K., Bacon, A.-M., Jochum, K. P., Dufour, E., et al. (2020). Zinc isotopes in Late Pleistocene fossil teeth from a Southeast Asian cave setting preserve paleodietary information. Proceedings of the National Academy of Sciences 117, 4675–4681. https://doi.org/10.1073/pnas.1911744117.

Bozec, L., Odlyha, M. (2011). Thermal denaturation studies of collagen by microthermal analysis and atomic force microscopy. Biophysical Journal 101, 228–236. https://doi.org/10.1016/j.bpj.2011.04.033.

Brazeau, M. D, Freidman, M. (2014). The characters of Palaeozoic jawed vertebrates. Zoological Journal of the Linnean Society 170, 779–821. https://doi.org/10.1111/zoj.1211.

Burton, J., Katzenberg, M. A. (2018). Strontium isotopes and the chemistry of bones and teeth. In Biological Anthropology of the Human Skeleton, Katzenberg, A. M., Grauer, A. L., (Eds.), 504–514. https://doi.org/10.1002/9781119151647.ch15.

Buss, D. J., Kröger, R., McKee, M. D., Reznikov, N. (2022). Hierarchical organization of bone in three dimensions: A twist of twists. Journal of Structural Biology: X 6:100057. https://doi.org/10.1016/j.yjsbx.2021.100057.

Cardoso, L., Fritton, S. P., Gailani, G., Benalla, M., Cowin, S. C. (2013). Advances in assessment of bone porosity permeability and interstitial fluid flow. Journal of Biomechanics 46, 253–265. https://doi.org/10.1016/j.jbiomech.2012.10.025.

Castro-Ceseña, A. B., Noviskaya, E. E., Chen, P.-Y., Hirate, G. A., McKittrick, J. (2011). Kinetic studies of bone demineralization at different HCl concentrations and temperatures. Materials Science and Engineering: C 31, 523–530. https://doi.org/10.1016/j.msec.2010.11.003.

Caut, S., Angulo, E., Courchamp, F. (2008). Discrimination factors (Δ^{15}N and Δ^{13}C) in an omnivorous consumer: effect of diet isotopic ratio. Functional Ecology 22, 255–263. https://doi.org/10.1111/j.1365-2435.2007.01360.x.

Cersoy, S., Zazzo, A., Rofes, J., Tresset, A., Gauthier, C., et al. (2017). Radiocarbon dating minute amounts of bone (3–60 mg) with ECHoMICADAS. Scientific Reports 7:7141. https://doi.org/10.1038/s41598-017-07645-3.

Chapin, R. E., Ku, W. W., Kenney, M. A., McCoy, H., Gladen, B., et al. (1997). The effects of dietary boron on bone strength in rats. Fundamental and Applied Toxicology 35, 205–215. https://doi.org/10.1006/faat.1996.2275.

Chang, S. J., Blake, R. E., Colman, A. S. (2021). Oxygen isotope exchange rates between phosphate and water catalyzed by inorganic pyrophosphatase: Implications for the biogeochemical cycle of phosphorus. Earth and Planetary Science Letters 570:117071. https://doi.org/10.1016/j.epsl.2021.117071.

Cooper, D. M., Kawalilak, C. E., Harrison, K., Johnston, B. D., Johnston, J. D. (2016). Cortical bone porosity: What is it, why is it important, and how can we detect it? Current Osteoporosis Reports 14, 187–198. https://doi.org/10.1007/s11914-016-0319-y.

Copeland, S. R., Sponheimer, M., le Roux, P. J., Grimes, V., Lee-Thorp, J. A., de Ruiter, D. J., Richards, M. P. (2008). Strontium isotope ratios ($^{87}Sr/^{86}Sr$) of tooth enamel: a comparison of solution and laser ablation multicollector inductively coupled plasma mass spectrometry methods. Rapid Communications in Mass Spectrometry 22, 3187–3194 https://doi.org/10.1002/rcm.3717.

Currey, J. D. (2011). The structure and mechanics of bone. Journal of Materials Science 47, 41–54. https://doi.org/10.1007/s10853-011-5914-9.

Currey, J. D., Shahar, R. (2013). Cavities in the compact bone in tetrapods and fish and their effect on mechanical properties. Journal of Structural Biology 183, 107-122. https: //doi.org/10.1016/j.jsb.2013.04.012.

Collins, M. J., Riley, M. S., Child, A. M., Turner-Walker, G. (1995). A basic mathematical simulation of the chemical degradation of ancient collagen. Journal of Archaeological Science 22, 175-183. https://doi.org/10.1006/jasc.1995.0019.

Collins, M. J., Nielsen-Marsh, C. M., Hiller, J., Smith, C. I., Roberts, J. P., et al. (2002). The survival of organic matter in bone: a review. Archaeometry 44 ,383-394. https://doi.org/10.1111/1475-4754.t01-1-00071

Combes, C., Cazalbou, S., Rey, C. (2016). Apatite biominerals. Minerals 6, 34. https://doi.org/10.3390/min6020034.

Daeschler, E. B., Shubin, N. H., Jenkins, Jr. F. A. (2006). A Devonian tetrapod-like fish and the evolution of the tetrapod body plan. Nature 440, 757–763. https://doi.org/10.1038/nature04639.

Dahl, S. G., Allain, P., Marie, P. J., Mauras, Y., Bovivin, G., et al. (2001). Incorporation and distribution of strontium in bone. Bone 28, 446–453. https://doi.org/10.1016/S8756-3282(01)00419-7.

Dal Sasso, G., Angelini, I., Maritan, L., Artiolo, G. (2018). Raman hyperspectral imaging as an effective and highly informative tool to study the diagenetic alteration of fossil bones. Talanta 179, 167–176. https://doi.org/10.1016/j.talanta.2017.10.059.

Dalrymple. G. B. (2001). The age of the Earth in the twentieth century: a problem (mostly) solved. Geological Society, London, Special Publications, 190, 205–221. https://doi.org/10.1144/GSL.SP.2001.190.01.14.

Dauphin, Y. (2022). Vertebrate taphonomy and diagenesis: Implications of structural and compositional alterations of phosphate biominerals. Minerals 12:180. https://doi.org/10.3390/min12020180.

Davis, M., Pineda-Munoz, S. (2016). The temporal scale of diet and dietary proxies. Ecology and Evolution 6, 1883–1897. https://doi.org/10.1002/ece3.2054.

Dawson, R. R., Field, D. J., Hull, P. M., Zelenitsky, D. K., Therrien, F., Affek, H. P. (2020). Eggshell geochemistry reveals ancestral metabolic thermoregulation in Dinosauria. Science Advances 6:eaax9361. https://doi.org/10.1126/sciadv.aax936.

Decrée, S., Herwartz, D., Mercadier, J., Miján, I., de Buffrénil, et al. (2018). The post-mortem history of a bone revealed by its trace element signature: The case of a fossil whale rostrum. Chemical Geology 477, 137–150. https://doi.org/10.1016/j.chemgeo.2017.12.021.

De Graaf, S., Vonhof, H. B., Weissbach, T., Wassenburg, J. A., Levy, E. J., et al. (2020). A comparison of isotope ratio mass spectrometry and cavity ring-down spectroscopy techniques for isotope analysis of fluid inclusion water. . Rapid Communications in Mass Spectrometry 34:e8837. https://doi.org/10.1002/rcm.8837.

De Graaf, S., Vonhof, H. B., Levy, E. J., Markowska, M., Haug, G. H. (2021). Isotope ratio infrared spectroscopy (IRIS) analysis of water samples without memory effects. Rapid Communications in Mass Spectrometry 35:e9055. https://doi.org/10.1002/rcm.9055.

De Laeter, J. R., Böhlke, J. K., De Bièvre, P., Hidaka, H., Peiser, H. S., et al. (2003). Atomic weights of the elements: Review 2000 (IUPAC Technical Report). Pure and Applied Chemistry 75, 683–800. https://doi.org/10.1351/pac200375060683.

Deng, H., Poonoosamy, J., Molins, S. (2022). A reactive transport modeling perspective on the dynamics of interface-coupled dissolution-precipitation. Applied Geochemistry 137:105207. https://doi.org/10.1016/j.apgeochem.2022.105207.

DeNiro, M. J., Epstein, S. (1978). Influence of diet on the distribution of carbon isotopes in animals. Geochimica et Cosmochimica Acta 42, 495–506. https://doi.org/10.1016/0016-7037(78)90199-0.

DeNiro, M. J., Epstein, S. (1981). Influence of diet on the distribution of nitrogen isotopes in animals. Geochimica et Cosmochimica Acta 45, 341–351. https://doi.org/10.1016/0016-7037(81)90244-1.

DeNiro, M.J. (1985). Postmortem preservation and alteration of in vivo bone collagen isotope ratios in relation to palaeodietary reconstruction. Nature 317, 806–809.

Denys, C. (2002). Taphonomy and experimentation. Archaeometry 44, 469-484. https://doi.org/10.1111/1475-4754.00079.

Dirks, P., Roberts, E. M., Hilbert-Wolf, H., Kramers, J. D., Hawks, J., et al. (2017). The age of Homo Naledi and associated sediments in the Rising Star Cave, South Africa. Evolutionary Biology, eLife 6:e24231. https://doi.org/10.7554/eLife.24231.001.

Dessordi, R., Navarro, M. A. (2017). Boron action in bone health. Rheumatology and orthopedic medicine 2, 1–3. https://doi.org/10.15761/ROM.1000112.

Dobberstein, R. C., Collins, M. J., Craig, O. E., Taylor, G., Penkman, K. E. H., and Ritz-Timme, S. (2009). Archaeological collagen: why worry about collagen diagenesis? Archaeological and Anthropological Sciences 1, 31–42. https://doi.org/10.1007/s12520-009-0002-7.

Dodat, P. J., Tacail, T., Albalat, E., Gómez-Olivencia, A., Couture-Veschambre, C., et al. (2021). Isotopic calcium biogeochemistry of MIS 5 fossil vertebrate bones: application to the study of the dietary reconstruction of Regourdou 1 Neandertal fossil. Journal of Human Evolution 151:102925. https://doi.org/10.1016/j.jhevol.2020.102925.

Dodd, M., Papineau, D., Grenne, T., Slack, J. F., Rittner, M., Pirajno, F., O'Neil, J., Little, C. T. S. (2017). Evidence for early life in Earth's oldest hydrothermal vent precipitates. Nature 543, 60–64. https://doi.org/10.1038/nature21377.

Doineau, E., Cathala, N., Benezet, J.-C., Bras, J., Le Moigne, N. (2021). Development of Bio-Inspired Hierarchical Fibres to Tailor the Fibre/Matrix Interphase in (Bio)composites. Polymers 13(5):804. https://doi.org/10.3390/polym13050804.

Donovan, J. J., Hanchar, J. M., Picolli, P. M., Schrier, M. D., Boatner, L. A., Jarosewich, E. (2003). A re-examination of the rare-earth-element orthophosphate standards in use for electron-microprobe analysis. The Canadian Mineralogist 41, 221–232. https://doi.org/10.2113/gscanmin.41.1.221.

Dow, E. C., Stanbury, J. B. (1960). Strontium and calcium metabolism in metabolic bone diseases. Journal of Clinical Investigations 39, 885–903. https://doi.org/10.1172/JCI104109.

Drucker, D. G., Naito, Y. I., Coromina, N., Rufí, I., Soler, N., Soler, J. (2021). Stable isotope evidence of human diet in Mediterranean context during the Last Glacial Maximum. Journal of Human Evolution 154:102967. https://doi.org10.1016/j.jhevol.2021.102967.

Eagle, R. A., Schauble, E. A., Tripatia, A. K., Tütken, T., Hulbert, R. C., Eiler, J. M. (2010). Body temperatures of modern and extinct vertebrates from ^{13}C-^{18}O bond abundances in bioapatite. Proceedings of the National Academy of Sciences of the United States of America 107, 10377–10382. https://doi.org/10.1073/pnas.0911115107.

Eagle, R. A., Tütken, T., Martin, T. S., Tripati, A. K., Fricke, H. C., et al. (2011). Dinosaur body temperatures determined from isotopic (^{13}C-^{18}O) ordering in fossil biominerals. Science 333, 443–445. https://doi.org/10.1126/science.1206196.

Eagle, R. A., Enriquez, M., Grellet-Tinner, G., Pérez-Huerta, A., Hu, D., et al. (2015). Isotopic ordering in eggshells reflects body temperatures and suggests differing thermophysiology in two Cretaceous dinosaurs. Nature Communications 6:8296. https://doi.org/10.1038/ncomms9296.

Elorza, J., Astibia, H., Murelaga, X., Pereda-Suberbiola, X. (1999). Francolite as a diagenetic mineral in dinosaur and other Upper Cretaceous reptile bones (Lano, Iberian Peninsula): Microstructural, petrological and geochemical features. Cretaceous Research 20, 169–187. https://doi.org/10.1006/cres.1999.0144.

Erel, Y., Pinhasi, R., Coppa, A., Ticher, A., Tirosh, O., et al. (2021). Lead in archeological human bones reflecting historical changes in lead production. Environmental Science & Technology 55, 14407–14413. https://doi.org/10.1021/acs.est.1c00614.

Ericson, J.E. (1985). Strontium isotope characterization in the study of prehistoric human ecology. Journal of Human Evolution 14, 503–514.

Fanale, F. P., Schaeffer, O. A. (1965). Helium-Uranium Ratios for Pleistocene and Tertiary Fossil Aragonites. Science 149, 312–317. https://doi.org/10.1126/science.149.3681.312.

Farkh, S., Zaiour, A., Abdallah, J., Farkh, S., Ismail, H., et al., 2015. New concept for calculating the age of a fossil bone by uranium-Series method. International Journal of Scientific & Technology Research 4, 8-14.

Fassett, J. E., Heaman, L. M., Simonetti, A. (2011). Direct U-Pb dating of Cretaceous and Paleocene dinosaur bones, San Juan Basin, New Mexico. Geology 39, 159–162. https://doi.org/10.1130/G31466.1.

Fau, A., Beyssac, O., Gauthier, M., Panczer, G., Gasnault, O., et al. (2022). Time-resolved Raman and luminescence spectroscopy of synthetic REE-doped hydroxylapatites and natural apatites. American Mineralogist, *in press*. https://doi.org/10.2138/am-2022-8006.

Fernández-Seara, M. A., Wehrli, S. L., Wehrli, F. W. (2002). Diffusion of exchangeable water in cortical bone studied by nuclear magnetic resonance. Biophysical Journal 82, 522–529. https://doi.org/10.1016/S0006-3495(02)75417-9.

Feng, D., Tütken, T., Löffler, N., Tröster, G., Pack, A. (2022). Isotopically anomalous metabolic oxygen in marine vertebrates as physiology and atmospheric proxy. Geochimica et Cosmochimica Acta 328, 85–102. https://doi.org/10.1016/j.gca.2022.05.008.

Fogel, M. L., Tuross, N. (2003). Extending the limits of paleodietary studies of humans with compound specific carbon isotope analysis of amino acids. Journal of Archaeological Science. 30, 535–545. https://doi.org/10.1016/S0305-4403(02)00199-1.

Forbes, S. (2014). Taphonomy in Bioarchaeology and Human Osteology. In: Smith C. (Eds) Encyclopedia of Global Archaeology. Springer, New York, NY. https://doi.org/ 10.1007/978-1-4419-0465-2_137.

Fraser, D., Kim, S. L., Welker, J. M., Clementz, M. T. (2021). Pronghorn (*Antilocapra americana*) enamel phosphate δ^{18}O values reflect climate seasonality: Implications for paleoclimate reconstruction. Ecology and Evolution 11, 17005–17021. https://doi.org/10.1002/ece3.8337.

Fricke, H. C., O'Neil, J. R. (1999). Inter- and intra-tooth variation in the oxygen isotope composition of mammalian tooth enamel phosphate: implications for palaeoclimatological and palaeobiological research. Palaeogeography, Palaeoclimatology, Palaeoecology 126, 91–99. https://doi.org/10.1016/S0031-0182(96)00072-7.

Fricke, H. C., Rogers, R. R., Backlund, R., Dwyer, C. N., Echt, S. (2008). Preservation of primary stable isotope signals in dinosaur remains, and environmental gradients of the Late Cretaceous of Montana and Alberta. Palaeogeography, Palaeoclimatology, Palaeoecology 266, 13–27. https://doi.org/10.1016/j.palaeo.2008.03.030.

Fripiat, J. J., Letellier, M., Levitz, P. (1984). Interaction of water with clay surfaces. Philosophical transactions. Series A, Mathematical, physical, and engineering sciences 311, 287–299. https://doi.org/10.1098/rsta.1984.0029.

Frost, H. M. (1969). Tetracycline-based histological analysis of bone re-modeling. Calcified Tissue Research 3, 211-237. https://doi.org/10.1007/BF02058664.

Gäb, F., Ballhaus, C., Stinnesbeck, E., Kral, A. G., Janssen, K., and Bierbaum, G. (2020). Experimental taphonomy of fish - role of elevated pressure, salinity and pH. Scientific Reports 10, 7839. https://doi.org/10.1038/s41598-020-64651-8.

Gehler, A., Tütken, T., Pack, A. (2011). Triple oxygen isotope analysis of bioapatite as tracer for diagenetic alteration of bones and teeth. Palaeogeography, Palaeoclimatology, Palaeoecology 310, 84–91. https://doi.org/10.1016/j.palaeo.2011.04.014.

Gehler, A., Tütken, T., Pack, A. (2012). Oxygen and Carbon Isotope Variations in a Modern Rodent Community – Implications for Palaeoenvironmental Reconstructions. PLoS ONE 7:e49531. https://doi.org/10.1371/journal.pone.0049531.

Geisler T., Kasioptas A., Menneken M., Perdikouri C., and Putnis A. (2009). A preliminary in situ Raman spectroscopic study of the oxygen isotope exchange kinetics between H_2O and $(PO_4)_{aq}$. Journal of Geochemical Exploration, 101, 37. https://doi.org/ 10.1016/j.gexplo.2008.12.004.

Geisler, T., Dohmen, L., Lenting, C., Fritzsche, M. B. K. (2019). Real-time *in situ* observations of reaction and transport phenomena during silicate glass corrosion by fluid-cell Raman spectroscopy. Nature Materials, 18, 342–348. https://doi.org/10.1038/s41563-019-0293-8.

Geisler, T., Menneken, T. (2021). Raman spectroscopy in fossilization research: Basic principles, applications in paleontology, and a case study on an acanthodian fish spine, in Gee, C.T., McCoy, V.E., Sander, P.M. (Eds.), Fossilization: Understanding the Material Nature of Ancient Plants and Animals. John Hopkins University Press, Baltimore, pp. 73–114.

Gilfrich, J. V., Skelton, E. F., Qadri, S. B., Kirkland, J. P., Nagel, D. J. (1983). Synchrotron radiation x-ray fluorescence analysis. Analytical Chemistry 55, 187-190. https://doi.org/10.1021/ac00253a006.

Glimcher, M. J. (2006). Bone: Nature of the calcium phosphate crystals and cellular, structural, and physical chemical mechanisms in their formation. Reviwes in Mineralogy and Geochemistry. 64, 223–282. https://doi.org/10.2138/rmg.2006.64.8.

Göhring, A., von Carnap-Bornheim, C., Hilberg, V., Mayr, C., Gruppe, G. (2018). Diet and species-specific oxygen isotope relationship and isotope spacing between structural carbonate and phosphate in archaeological mammalian bones. Archaeological and Anthropological Sciences 11, 2467–2487. https://doi.org/10.1007/s12520-018-0704-9.

Goodwin, M. B., Grant, P. G., bench, G., Holroyd, P. A. (2007). Elemental composition and diagenetic alteration of dinosaur bone: Distinguishing micron-scale spatial and compositional heterogeneity using PIXE. Palaeogeography, Palaeoclimatology, Palaeoecology 253, 458-476. https://doi.org/10.1016/j.palaeo.2007.06.017.

Goldstein, J. I., Newbury, D. E., Echlin, P., Joy, D. C., Romig Jr., A. D., et al. (1992). Quantitative X-Ray Analysis: The Basics. In: Goldstein, J.I., Newbury, D.E., Echlin, P., Joy, A.C., Romig Jr., A.D., Lyman, C.E., Fiori, C., Lifshin, E. (Eds.), Scanning Electron Microscopy and X-Ray Microanalysis. Springer, Boston, MA, pp. 395–416. https://doi.org/10.1007/978-1-4613-0491-3_8.

Grandfield, K., Vuong, V., Schwarcz, H. P. (2018). Ultrastructure of Bone: Hierarchical Features from Nanometer to Micrometer Scale Revealed in Focused Ion Beam Sections in the TEM. Calcified Tissue International 103, 606–616. https://doi.org/10.1007/s00223-018-0454-9.

Green, D. R., Olack, G., Colman, A. S. (2018). Determinants of blood water $\delta^{18}O$ variation in a population of experimental sheep: implications for paleoclimate reconstruction. Chemical Geology 485, 32–43. https://doi.org/10.1016/j.chemgeo.2018.03.034.

Grimstead, D. N., Clark, A. E., Rezac, A. (2018). Uranium and vanadium concentrations as a trace element method for identifying diagenetically altered bone in the inorganic phase. Journal of Archaeological Method and Theory 25, 689–704. https://doi.org/10.1007/s10816-017-9353-z.

Grupe G., Harbeck M. (2015). Taphonomic and diagenetic processes. In: Henke W., Tattersall I. (Eds.) Handbook of Paleoanthropology. Springer, Berlin, Heidelberg. https://doi.org/10.1007/978-3-642-39979-4_7.

Grün, R. (2006). Direct dating of human fossils. American Journal of Physical Anthropology 131, 2–48. https://doi.org/10.1002/ajpa.20516.

Grün, R. (2008). Electron spin resonance dating. In Encyclopedia of Archaeology Pearsall DM, Ed. Academic Press, 1120-1128. https://doi.org/10.1016/B978-012373962-9.00099-6.

Grün, R., Aubert, M., Hellstorm, J. C., Duval, M. (2010). The challenge of direct dating old human fossils. Quaternary International 223-224, 87-93. https://doi.org/10.1016/j.quaint.2009.10.005.

Grün, R., Eggins, S., Kinsley, L., Moseley, H., Sambride, M. (2014). Laser ablation U-series analysis of fossil bones and teeth. Palaeogeography, Palaeoclimatology, Palaeoecology 416, 150-167. https://doi.org/10.1016/j.palaeo.2014.07.023.

Guntur, A. R., Rosen, C. J. (2012). Bone as an endocrine organ. Endocrine practice: official journal of the American College of Endocrinology and the American Association of Clinical Endocrinologists 18, 758–762. https://doi.org/10.4158/EP12141.RA.

Guiry, E., Royle, T. C. A., Matson, R. G., Ward, H., Weir, T. (2020). Differentiating salmonid migratory ecotypes through stable isotope analysis of collagen: Archaeological and ecological applications. PLoS ONE 15, e0232180. https://doi.org/10.1371/journal.pone.0232180.

Hardy, K., Bocherens, H., Miller, J. B., Copeland, L. (2022). Reconstructing Neanderthal diet: The case for carbohydrates. Journal of Human Evolution 162:103105. https://doi.org/10.1016/j.jhevol.2021.103105.

Hare, D., Austin, C., Doble, P., Arora, M. (2011). Elemental bio-imaging of trace elements in teeth using laser ablation-inductively coupled plasma-mass spectrometry. Journal of Dentistry 39, 397-403. https://doi.org/10.1016/j.jdent.2011.03.004.

Hedges, R. E. M. (2002). Bone diagenesis: an overview of processes. Archaeometry 44, 319-328. https://doi.org/10.1111/1475-4754.00064.

Hedges, R. E. M, Stevens, R. E., Richards, M. P. (2004). Bone as a stable isotope archive for local climatic information. Quaternary Science Reviews 23, 959–965. https://doi.org/10.1016/j.quascirev.2003.06.022.

Hellstrom, J., Pickering, R. (2015). Recent advances and future prospects of the U–Th and U–Pb chronometers applicable to archaeology. Journal of Archaeological Science 56, 32–40. https://doi.org/10.1016/j.jas.2015.02.032.

Henderson, P., Marlow, C.A., Molleson, T. I., Williams, C. T. (1983). Patterns of chemical change during bone fossilization. Nature 306, 358–360.

Herwartz, D., Tütken, T., Münker, C., Jochum, K. P., Stoll, B., et al. (2011). Timescales and mechanisms of REE and Hf uptake in fossil bones. Geochimica et Cosmochimica Acta 75, 82–105. https://doi.org/10.1016/j.gca.2010.09.036.

Herwartz, D., Tütken, T., Jochum, K. P., Sander, P. M. (2013a). Rare earth element systematics of fossil bone revealed by LA-ICPMS analysis. Geochimica et Cosmochimica Acta 103, 161–183. https://doi.org/10.1016/j.gca.2012.10.038.

Herwartz, D., Münker, C., Tütken, T., Hoffmann, J. E., Wittke, A., Barbier, B. (2013b). Lu–Hf isotope systematics of fossil biogenic apatite and their effects on geochronology. Geochimica et Cosmochimica Acta 101, 328–343. https://doi.org/10.1016/j.gca.2012.09.049.

Heuser, A., Tütken, T., Gussone, N., Galer, S. J. (2011). Calcium isotopes in fossil bones and teeth — Diagenetic versus biogenic origin. Geochimica et Cosmochimica Acta 75, 3419–3433. https://doi.org/10.1016/j.gca.2011.03.032.

Hinz, E. A., Kohn, M. J. (2010). The effect of tissue structure and soil chemistry on trace element uptake in fossils. Geochimica et Cosmochimica Acta 74, 3213–3231. https://doi.org/10.1016/j.gca.2010.03.011.

Hoppe, K. A., Koch, P. L., Carlson, R. W., Webb, S. D. (1999). Tracking mammoths and mastodons: reconstruction of migratory behavior using strontium isotope ratios. Geology 27, 439–442. https://doi.org/10.1130/0091-7613(1999)027<0439:TMAMRO>2.3.CO;2.

Hubert, J. F., Panish, P. T., Chure, D. J., Prostak, K. S. (1996). Chemistry, microstructure, petrology, and diagenetic model of Jurassic dinosaur bones, Dinosaur National Monument, Utah. Journal of Sedimentary Research 66, 531–547. https://doi.org/10.1306/D426839C-2B26-11D7-8648000102C1865D.

Iacumin, P., Bocherens, H., Mariotti, A., Longinelli, A. (1996). Oxygen isotope analyses of co-existing carbonate and phosphate in biogenic apatite: a way to monitor diagenetic alteration of bone phosphate? Earth and Planetary Science Letters 142, 1–6. https://doi.org/10.1016/0012-821X(96)00093-3.

Jans, M. M. E. (2008). Microbial bioerosion of bone - A review. In: Wisshak, M., Tapanila, L. (eds) Current Developments in Bioerosion. Erlangen Earth Conference Series. Springer, Berlin, Heidelberg. https://doi.org/10.1007/978-3-540-77598-0_20.

Jaouen, K., Pons, M.-L., Balter, V. (2013). Iron, copper and zinc isotopic fractionation up mammal trophic chains. Earth and Planetary Science Letters 374, 164e172.

Jaouen, K., Beasley, M., Schoeninger, M., Hublin, J.-J., Richards, M.P. (2016a). Zinc isotope ratios of bones and teeth as new dietary indicator. Scientific Reports 6:26281. https://doi.org/10.1038/srep26281. CHAPTER 3

Jaouen, K., Szpak, P., Richards, M. P. (2016b). Zinc Isotope Ratios as Indicators of Diet and Trophic Level in Arctic Marine Mammals. PLoS ONE 11: e0152299. https://doi.org/10.1371/journal.pone.0152299. INTRODUCTION

Jaouen, K., Richards, M. P., Le Cabec, A., Welker, F., Rendu, W. (2019). Exceptionally high δ^{15}N values in collagen single amino acids confirm Neandertals as high-trophic level carnivores. Proceedings of the National Academy of Sciences 116, 4928–4933. https://doi.org/10.1073/pnas.1814087116.

Jaouen, K., Trost, M., Bourgon, N., Colleter, R., Le Cabec, A., et al. (2020). Zinc isotope variations in archeological human teeth (Lapa do Santo, Brazil) reveal dietary transitions in childhood and no contamination from gloves. PLoS ONE 15:e0232379. https://doi.org/10.1371/journal.pone.0232379.

Jarosewich, E., Nelen, J. A., Norberg, J. A. (1980). Reference Samples for Electron Microprobe Analysis. Geostandard Newsletter 4, 43–47. https://doi.org/10.1111/j.1751-908X.1980.tb00273.x.

Jarosewich, E., White, J. S. (1987). Strontianite reference sample for electron microprobe and SEM analyses. Journal of Sedimentary Research 57, 762–763. https://doi.org/10.1306/212F8C10-2B24-11D7-8648000102C1865D.

Jarosewich, E., Boatner, L. A. (1991). Rare-Earth Element Reference Samples for Electron Microprobe Analysis. Geostandards and Geoanalytical Research 15, 397–399. https://doi.org/10.1111/j.1751-908X.1991.tb00115.x.

Joannes-Boyau, R. (2014). Electron Spin Resonance (ESR) dating in archaeology. In Smith C. (Ed). Encyclopedia of Global Archaeology. Springer, New York, NY. https: //doi.org/10.1007/978-1-4419-0465-2_244.

Karr, L. P., Outram, A. K. (2012). Bone degradation and environment: understanding, assessing and conducting archaeological experiments using modern animal bones. International Journal of Osteoarchaeology 25, 201–212. https://doi.org/10.1002/oa.2275.

Keenan, S. W. (2016). From bone to fossil: A review of the diagenesis of bioapatite. American Mineralogist 101, 1943–1951. https://doi.org/10.2138/am-2016-5737.

Keenan, S. W. (2021). Fossilization. Encyclopedia of Geology, 2nd Edition, Elsevier, pp 1-11. https://doi.org/10.1016/B978-0-12-409548-9.12067-6.

Keenan, S. W., and Engel, A. S. (2017). Early diagenesis and recrystallization of bone. Geochimica et Cosmochimica Acta 196, 209–223. https://doi.org/10.1016/j.gca.2016.09.033.

Kelly, P. J., Bassingthwaighte, J. B. (1977). Studies on bone ion exchanges using multiple-tracer indicator-dilution techniques. Federation proceedings 36, 2634–2639.

Kendall, C., Eriksen, A. M. H., Kontopoulos, I., Collins, M. J., Turner-Walker, G. (2018) Diagenesis of archaeological bone and tooth. Palaeogeography, Palaeoclimatology, Palaeoecology 491, 21-37. https://doi.org/10.1016/j.palaeo.2017.11.041.

Kenkre, J. S., Bassett, J. H. D. (2018). The bone remodeling cycle. Annals of Clinical Biochemistry 55, 308–327. https://doi.org/10.1177/0004563218759371.

Kini, U., Nandeesh, B. N. (2012). Physiology of bone formation, remodelling, and metabolism. In I Fogelman, G Gnanasegaran, H Wall, Eds., Radionuclide and Hybrid Bone Imaging, Springer, Berlin, Heidelberg, 29–57. https://doi.org/10.1007/978-3-642-02400-9_2.

Knudson, K. J., Williams, H. M., Buikstra, J. E., Tomczak, P. D., Gordon, G. W., Anbar, A. D. (2010). Introducing $\delta^{88/86}$Sr analysis in archaeology: A demonstration of the utility of strontium isotope fractionation in paleodietary studies. Journal of Archaeological Science. 37, 2352e2364.

Kocsis, L., Trueman, C. N., Palmer, M. R. (2010). Protracted diagenetic alteration of REE contents in fossil bioapatites: Direct evidence from Lu–Hf isotope systematics. Geochimica et Cosmochimica Acta 74, 6077–6092. https://doi.org/10.1016/j.gca.2010.08.007.

Koehler, S. J., Harouiya, N., Chaïat, C., Oelkers, E. H. (2005). Experimental studies of REE fractionation during water–mineral interactions: REE release rates during apatite dissolution from pH 2.8 to 9.2. Chemical Geology 222, 168–182. https://doi.org/10.1016/j.chemgeo.2005.07.011.

Koeppenkastrop, D., Carlo de, E. H. (1992). Sorption of rare-earth elements from seawater onto synthetic mineral particles: An experimental approach. Chemical Geology 95, 251–263. https://doi.org/10.1016/0009-2541(92)90015-W.

Kohn, M. J. (1996). Herbivore tooth oxygen isotope compositions: Effects of diet and physiology. Geochimica et Cosmochimica Acta 60, 3889–3896. https://doi.org/10.1016/0016-7037(96)00248-7.

Kohn, M. J., Schoeninger, M. J., Barker, W. W. (1999). Altered states. Effects of diagenesis on fossil tooth chemistry. Geochimica et Cosmochimica Acta 63, 2737–2747. https://doi.org/10.1016/S0016-7037(99)00208-2.

Kohn, M. J. (2008). Models of diffusion-limited uptake of trace elements in fossils and rates of fossilization. Geochimica et Cosmochimica Acta 72, 3758–3770. https://doi.org/10.1016/j.gca.2008.05.045.

Kohn, M. J., Moses, R. J. (2013). Trace element diffusivities in bone rule out simple diffusive uptake during fossilization but explain in vivo uptake and release. Proceedings of the National Academy of Sciences 110, 419–424. https://doi.org/10.1073/pnas.1209513110.

Kohn, M. J., Morris, J., Olin, P. (2013). Trace element concentrations in teeth – a modern Idaho baseline with implications for archeometry, forensics, and palaeontology. Journal of Archaeological Science 40, 1689–1699. https://doi.org/10.1016/j.jas.2012.11.012.

Kolodny, Y., Luz, B., Navon, O. (1983). Oxygen isotope variations in phosphate of biogenic apatites, I. Fish bone apatite - rechecking the rules of the game. Earth and

Planetary Science Letters 64, 398–404. https://doi.org/10.1016/0012-821X(83)90100-0.

Kolodny, Y., Luz, B., Sander, M., Celemens, W. A. (1996). Dinosaur bones: fossils or pseudomorphs? The pitfalls of physiology reconstruction from apatitic fossils. Palaeogeography, Palaeoclimatology, Palaeoecology126, 161–171. https://doi.org/10.1016/S0031-0182(96)00112-5.

Konrad-Schmolke, M., Halama, R., Wirth, R., Thomen, A., Klitscher, N., et al. (2018). Mineral dissolution and reprecipitation mediated by an amorphous phase. Nature Communications 9:1637. https://doi.org/10.1038/s41467-018-03944-z.

Kowalik, N., Anczkiewicz, R., Wilczyński, J., Wojtal, P., Müller, W., (2020). Tracing human mobility in central Europe during the Upper Paleolithic using sub-seasonally resolved Sr isotope records in ornaments. Scientific Reports 10, 10386. https://doi.org/10.1038/s41598-020-67017-2.

König, A. E., Rogers, R. R., Trueman, C. N. (2009). Visualizing fossilization using laser ablation–inductively coupled plasma–mass spectrometry maps of trace elements in Late Cretaceous bones. Geology 37, 511-514. https://doi.org/10.1130/G25551A.1.

Krajcarz, M. T., Krajcarz, M., Bocherens, H. (2018). Collagen-to-collagen prey-predator isotopic enrichment ($\Delta^{13}C$, $\Delta^{15}N$) in terrestrial mammals - a case study of a subfossil red fox den. Palaeogeography, Palaeoclimatology, Palaeoecology 490, 563–570. https://doi.org/10.1016/j.palaeo.2017.11.044.

Kral, A. G., Ziegler, A., Tütken, T., Geisler, T. (2021). Experimental aqueous alteration of cortical bone microarchitecture analyzed by quantitative micro-computed tomography. Frontiers in Earth Science 9:609496. https://doi.org/10.3389/feart.2021.609496.

Kral, A. G., Tütken, T., Guagliardo, P., Lagos, M. (under review). Rapid alteration of cortical bone in fresh- and seawater solutions visualized and quantified from the millimeter down to the atomic scale. Chemical Geology.

Kramers, J. D., Makhubela, T. V. (2022). (U,Th)-He dating of Pleistocene carbonates: Analytical methods and age calculations. MethodsX 9:101608. https://doi.org/10.1016/j.mex.2021.101608.

Kuipers, J., Giepmans, B.N.G. (2020). Neodymium as an alternative contrast for uranium in electron microscopy. Histochemistry and Cell Biology 153, 271–277. https://doi.org/10.1007/s00418-020-01846-0.

Lambri, M. L., Giordano, E. D., Bozzano, P. B., Bonifacich, F. G., Pérez-Landazábal, J. I., et al. (2016). Thermal degradation of type I collagen from bones. Journal of Renewable Materials 4, 251–257. https://doi.org/10.7569/JRM.2016.634111.

Lanfranco, A. M., Schofield, P. F., Murphy, P. J., Hodson, M. E., Mosselmans, J. F. W., Valsami-Jones, E. (2003). Characterization and identification of mixed-metal phosphates in soils: the application of Raman spectroscopy. Mineralogical Magazine, 67, 1299–1316. https://doi.org/10.1180/0026461036760166.

Langelier, B., Wang, X., Grandfield, K. (2017). Atomic scale chemical tomography of human bone. Scientific Reports 7:39958. https://doi.org/10.1038/srep39958.

Langlois, C., Simon, L., Lécuyer, C. (2003). Box-modeling of bone and tooth phosphate oxygen isotope compositions as a function of environmental and physiological parameters. Isotopes in Environmental and Health Studies 39, 259-272. https://doi.org/10.1080/10256010310001621146.

Larivière, D., Tolmachev, S. Y., Kochermi, V., Johnson, S. (2013). Uranium bone content as an indicator of chronic environmental exposure from drinking water. Journal of Environmental Radioactivity 121, 98–103. https://doi.org/10.1016/j.jenvrad.2012.05.026.

Lécuyer, C., Grandjean, P., Sheppard, S. M. F. (1999). Oxygen isotope exchange between dissolved phosphate and water at temperatures ≤135°C: inorganic versus biological fractionations. Geochimica et Cosmochimica Acta 63, 855–862. https://doi.org/10.1016/S0016-7037(99)00096-4.

Lécuyer, C., Bogey, C., Garcia, J. P., Grandjean, P., Barrat, J. A., et al. (2003). Stable isotope composition and rare earth element content of vertebrate remains from the Late Cretaceous of northern Spain (Lano): did the environmental record survive? Palaeogeography Palaeoclimatology Palaeoecology 193, 457–472. https://doi.org/10.1016/S0031-0182(03)00261-X.

Leichliter, J. N., Lüdecke, T., Foreman, A. D., Duprey, N. N., Winkler, D. E., et al. (2021). Nitrogen isotopes in tooth enamel record diet and trophic level enrichment: Results from a controlled feeding experiment. Chemical Geology 563:120047. https: //doi.org/10.1016/j.chemgeo.2020.120047.

LeGeros, R. Z., Trautz, O. R., Klein, E., LeGeros, J. P. (1969). Two types of carbonate substitution in the apatite structure. Experimentia 25, 5–7. https://doi.org/10.1007/BF01903856.

LeGeros, R. Z., LeGeros, J. P. (1984). Phosphate Minerals in Human Tissues. In: JO Nriagu, PB Moore, Eds. Phosphate Minerals. Springer, Berlin, Heidelberg, 351–385. https://doi.org/10.1007/978-3-642-61736-2_12.

Lenting, C., Geisler, T. (2021). Corrosion of ternary borosilicate glass in acidic solution studied in operando by fluid-cell Raman spectroscopy. npj Materials Degradation 5:37. https://doi.org/10.1038/s41529-021-00182-5.

Lenz, C., Talla, D., Ruschel, K., Skoda, R., Götze, J., Nasdala, L. (2013). Factors Affecting the Nd^{3+} (REE^{3+}) Luminescence of Minerals. Mineralogy and Petrology 107, 415–428. https://doi.org/10.1007/s00710-013-0286-2.

Levin, N. E., Cerling, T. E., Passey, B. H., Harris, J. M., Ehleringer, J. R. (2006). A stable isotope aridity index for terrestrial environments. Proceedings of the National Academy of Sciences of the United States of America 103, 11201–11205. https://doi.org/10.1073/pnas.0604719103.

Lewis, J., Pike, A. W. G, Coath, C. D., Eversehd, R. P. (2017). Strontium concentration, radiogenic ($^{87}Sr/^{86}Sr$) and stable ($\delta^{88}Sr$) strontium isotope systematics in a controlled feeding study. STAR: Science & Technology of Archaeological Research 3, 45–57, https://doi.org/10.1080/20548923.2017.1303124.

Lin, J., Raghavan, S., Fuerstenau, D. W. (1981). The adsorption of fluoride ions by hydroxyapatite from aqueous solution. Colloids and Surfaces 3, 357−370, https://doi.org/10.1016/0166-6622(81)80062-5.

Liu, Y., Luo, D., Wang, T. (2016). Hierarchical Structures of Bone and Bioinspired Bone Tissue Engineering. Small 12, 4611–4632. https://doi.org/10.1002/smll.201600626.

Longinelli, A., Nuti, S. (1973). Revised phosphate-water isotopic temperature scale. Earth and Planetary Science Letters 19, 373–376. https://doi.org/10.1016/0012-821X(73)90088-5.

Longinelli, A. (1984). Oxygen isotopes in mammal bone phosphate: A new tool for paleohydrological and paleoclimatological research? Geochimica et Cosmochimica Acta 48, 385–390. https://doi.org/10.1016/0016-7037(84)90259-X.

Ludwig, K. R. (2012). Direct U-Pb dating of Cretaceous and Paleocene dinosaur bones, San Juan Basin, New Mexico: COMMENT. Geology 40: e258. https://doi.org/10.1130/G32503C.1

Lugli, F., Cipriani, A., Peretto, C., Mazzucchelli, M., Brunelli, D. (2017). In situ high spatial resolution $^{87}Sr/^{86}Sr$ ratio determination of two Middle Pleistocene (c.a. 580 ka) Stephanorhinus hundsheimensis teeth by LA–MC–ICP–MS. International Journal of Mass Spectrometry 412, 38–48. https://doi.org/10.1016/j.ijms.2016.12.012.

Luz B, Kolodny Y, 1989. Oxygen isotope variation in bone phosphate. Applied Geochemistry 4, 317–323. https://doi.org/10.1016/0883-2927(89)90035-8.

Luz B, Barkan E (2010). Variations of $^{17}O/^{16}O$ and $^{18}O/^{16}O$ in meteoric waters. Geochimica et Cosmochimica Acta 74, 6276−6286. https://doi.org/10.1016/j.gca.2010.08.016.

Lyman, R. (2010). What Taphonomy is, what it isn’t, and why taphonomists should care about the difference. Journal of taphonomy 8, 1-16.

Makhubela, T. V., Kramers, J. D. (2022). Testing a new combined (U,Th)–He and U/Th dating approach on Plio-Pleistocene calcite speleothems. Quaternary Geochronology 67:101234. https://doi.org/10.1016/j.quageo.2021.101234.

Martin, R. B., Burr, D. B. (1989). Structure, function, and adaptation of compact bone. New York: Raven Press.

Martin, J. E., Vance, D., Balter, V. (2014). Natural variation of magnesium isotopes in mammal bones and teeth from two South African trophic chains. Geochimica et Cosmochimica Acta 130, 12–20. https://doi.org/10.1016/j.gca.2013.12.029.

Martin, J. E., Vance, D., Balter, V. (2015). Magnesium stable isotope ecology using mammal tooth enamel. Proceedings of the National Academy of Sciences 112, 430–435. https://doi.org/10.1073/pnas.1417792112.

Martin, J. E., Tacail, T., Balter, V. (2017). Non-traditional isotope perspectives in vertebrate palaeobiology. Palaeontology 60, 485–502. https://doi.org/10.1111/pala.12300.

Madupalli, H., Pavan, B., Tecklenburg, M. (2017). Carbonate substitution in the mineral component of bone: Discriminating the structural changes, simultaneously imposed by carbonate in A and B sites of apatite. Journal of solid-state chemistry, 255, 27–35. https://doi.org/10.1016/j.jssc.2017.07.025.

Marenzana, M., Shipley, A. M., Squitiero, P., Kunkel, J. G., Rubinacci, A. (2005). Bone as an ion exchange organ: Evidence for instantaneous cell-dependent calcium efflux from bone not due to resorption. Bone 37, 545–554. https://10.1016/j.bone.2005.04.036.

Marenzana, M., Arnett, T. R. (2013). The key role of the blood supply to bone. Bone Research 1, 203–215. https://doi.org/10.4248/BR201303001.

Martin, J. E., Vance, D., Balter, V. (2015). Magnesium stable isotope ecology using mammal tooth enamel. Proceedings of the National Academy of Sciences of the United States of America 112, 430–435. https://doi.org/10.1073/pnas.1417792112.

Martin, J. E., Tacail, T., Balter, V. (2017). Non-traditional isotope perspectives in vertebrate palaeobiology. Paleontology 60, 485–502. https://doi.org/10.1111/pala.12300.

Marx, D., Yazdi, A. R., Papini, M., Towler, M. (2020). A review of the latest insights into the mechanism of action of strontium in bone. Bone Reports 12:100273. https://doi.org/10.1016/j.bonr.2020.100273.

Matthiesen, H., Høier Eriksen, A. M., Hollesen, J., Collins, M. (2021). Bone degradation at five Arctic archaeological sites: Quantifying the importance of burial environment and bone characteristics. Journal of Archaeological Science. 125, 105296. https://doi.org/10.1016/j.jas.2020.105296.

Maurer, A. F., Galer, S. J., Knipper, C., Beierlein, L., Nunn, E. V., et al. (2012). Bioavailable $^{87}Sr/^{86}Sr$ in different environmental samples – effects of anthropogenic contamination and implications for isoscapes in past migration studies. Science of The Total Environment 433, 216–229. https://doi.org/10.1016/j.scitotenv.2012.06.046.

McCormack, J. M., Bahr, A., Gerdes, A., Tütken, T., Prinz-Grimm, P. (2015). Preservation of successive diagenetic stages in Middle Triassic bonebeds: evidence from in situ trace element and strontium isotope analysis of vertebrate fossils. Chemical Geology 410, 108–123. https://doi.org/10.1016/j.chemgeo.2015.06.003.

McKernan, W. M., Dailly, S. D. (1966). The relationship between swelling of hard tissue collagen in acid and alkali and the presence of phosphate cross-links, in Fleisch H., Blackwood H.J.J., Owen M. (Eds.), Calcified Tissues. Springer, Berlin, Heidelberg, pp. 171–174. https://doi.org/10.1007/978-3-642-49802-2_33.

Mikhalyova, E. A., Khomenko, O. V., Gavrilenko, K. S., Dotsenko, V. P., Addison, A. W., Pavlishchuk, V. V. (2019). Absorption- and Excitation-Modulated Luminescence of Pr^{3+}, Nd^{3+}, and Lu^{3+} Compounds with Dianions of Tetrafluoroterephthalic and Camphoric Acids. ACS Omega 4, 2669–2675. https://doi.org/10.1021/acsomega.8b02388.

Millard, A. R., and Hedges, R. E. M. (1996). A diffusion-adsorption model of uranium uptake by archaeological bone. Geochimica et Cosmochimica. Acta 60, 2139–2152. https://doi.org/10.1016/0016-7037(96)00050-6.

Miller Wolf, K. A., Freiwald, C. (2018). Re-interpreting ancient Maya mobility: a strontium isotope baseline for Western Honduras. Journal of Archaeological Science: Reports 20, 799–807. https://doi.org/10.1016/j.jasrep.2018.04.023.

Mills, R. (1973). Self-diffusion in normal and heavy water in the range 1-45.eg. The Journal of Physical Chemistry 77, 685–688. https://doi.org/10.1021/j100624a025.

Monti, F., Robert, A., Dominici, J.M., Sforzi, A., Bagur, R.T., et al. (2021). Using GPS tracking and stable multi-isotopes for estimating habitat use and winter range in Palearctic ospreys. Oecologia, 195, 655–666. https://doi.org/10.1007/s00442-021-04855-5.

Morgan, E. F., Barnes, G. L., Einhorn, T. A. (2013). The bone organ system: Form and function. In Osteoporosis R Marcus, D Feldman, DW Dempster, M Luckey, JA Cauley, Eds. Academic Press, 3–20. https://doi.org/10.1016/B978-0-12-415853-5.00001-7.

Mosiman, D. S., Sutrisno, A., Fu, Riqiang, Marinas, B. J. (2021). Internalization of fluoride in hydroxyapatite nanoparticles. Environmental Science & Technology 55, 2639–2651. https://doi.org/10.1021/acs.est.0c07398.

Müller, A. H. (1992). Lehrbuch der Paläozoologie. 1. Allgemeine Grundlagen, pp. 514. Stuttgart, Fischer.

Mueller, F., Zeitz, C., Mantz, H., Ehses, K.-H., Soldera, F., et al. (2010). Elemental depth profiling of fluoridated hydroxyapatite: saving your Dentition by the skin of your teeth? Langmuir 26, 18750−18759. https://doi.org/10.1021/la102325e.

Munro, L. E., Longstaffe, F. J., White, C. D. (2007). Burning and boiling of modern deer bone: effects on crystallinity and oxygen isotope composition of bioapatite phosphate. Palaeogeography, Palaeoclimatology, Palaeoecology 249, 90–102. https://doi.org/10.1016/j.palaeo.2007.01.011.

Nelson, B.K., DeNiro, M.J., Schoeninger, M.J., DePaolo, D.J., Hare, P.E. (1986). Effects of diagenesis on strontium, carbon, nitrogen and oxygen concentration and isotopic composition of bone. Geochimica et Cosmochimica Acta 50, 1941–1949.

Nemliher, J., Kurvits, T., Kallaste, T., Puura, I. (2004). Apatite varieties in the shell of the Cambrian lingulate brachiopod Obolus apollinis Eichwald. Proceedings of the Estonian Academy of Sciences. Geology 53, 246–256. https://doi.org/10.3176/geol.2004.4.02.

Neuman, W. F., Mulryan, B. J. (1951). The surface chemistry of bone. VI. Recrystallization in vivo. Journal of Biological Chemistry 195, 843–848. https://doi.org/10.1016/S0021-9258(18)55795-1.

Nielsen, F.H. (2014). Update on human health effects of boron. Journal of Trace Elements in Medicine and Biology 28, 383–387. https://doi.org/10.1016/j.jtemb.2014.06.023.

Nielsen-Marsh, C. M., and Hedges, R. E. M. (2000). Patterns of diagenesis in bone I: the effects of site environments. Journal of Archaeological Science 27, 1139–1150. https://doi.org/10.1006/jasc.1999.0537.

Nitzsche, K. N., Shin, K.-C., Kato, Y., Kamauchi, H., Takano, S., Tayasu, I. (2020). Magnesium and zinc stable isotopes as a new tool to understand Mg and Zn sources in stream food webs. Ecosphere 11:e03197. https://doi.org/10.1002/ecs2.3197.

O'Flaherty, E. J. (1991a). Physiologically based models for bone-seeking elements: I. Rat skeletal and bone growth. Toxicology and Applied Pharmacology 111, 299–312. https://doi.org/10.1016/0041-008X(91)90032-A.

O'Flaherty, E. J. (1991b). Physiologically based models for bone-seeking elements: III. Human skeletal and bone growth. Toxicology and Applied Pharmacology 111, 332–341. https://doi.org/10.1016/0041-008X(91)90034-C.

O'Flaherty, E. J. (1991c). Physiologically based models for bone-seeking elements: II. Kinetics of lead disposition in rats. Toxicology and Applied Pharmacology 111, 313–331. https://doi.org/10.1016/0041-008X(91)90033-B.

O'Flaherty, E. J. (1993). Physiologically based models for bone-seeking elements: IV. Kinetics of lead disposition in humans. Toxicology and Applied Pharmacology 118, 16–29. https://doi.org/10.1006/taap.1993.1004.

O'Flaherty, E. J. (1995). Physiologically based models for bone-seeking elements: V. Lead absorption and disposition in childhood. Toxicology and Applied Pharmacology 131, 297–308. https://doi.org/10.1006/taap.1995.1072.

O'Neil, J. R., Vennemann, T. W., McKenzie, W. F. (2003). Effects of speciation on equilibrium fractionations and rates of oxygen isotope exchange between $(PO_4)_{aq}$ and H_2O. Geochimica et Cosmochimica Acta 67, 3135–3144. https://doi.org/10.1016/S0016-7037(02)00970-5.

Pack, A., Gehler, A., Süssenberger, A. (2013). Exploring the usability of isotopically anomalous oxygen in bones and teeth as a paleo-CO_2-barometer. Geochimica et Cosmochimca Acta 102, 306–317. https://doi.org/10.1016/j.gca.2012.10.017.

Pan, Y., Fleet, M. (2002). Compositions of the apatite-group minerals: Substitution mechanisms and controlling factors. Reviews in Mineralogy and Geochemistry 48, 13–49. https://doi.org/10.2138/rmg.2002.48.2.

Panczer, G., Ligny de, D., Mendoza, C., Gaft, M., Seydoux-Guillaume, A.-M., Wang, X. (2012). Raman and fluorescence, in Dubessy, J., Caumon, M.-C., Rull, F. (Eds.), Raman spectroscopy applied to Earth sciences and cultural heritage. European Mineralogical Union Notes in Mineralogy 12, 61–82. https://doi.org/10.1180/EMU-notes.12.2.

Panigrahi, M., Grabda, M., Kozak, D., Dorai, A., Shibata, E., et al. (2016). Liquid-liquid extraction of neodymium ions from aqueous solutions of $NdCl_3$ by phosphonium-based ionic liquids. Separation and Purification Technology 171, 263–269. https://doi.org/10.1016/j.seppur.2016.07.044.

Parfitt, A. M. (1994). Osteonal and hemi-osteonal remodeling: the spatial and temporal framework for signal traffic in adult human bone. Journal of Cellular Biochemistry, 55, 273-286. https://doi.org/10.1002/jcb.240550303.

Passey, B. H., Levin, N. E. (2021). Triple Oxygen Isotopes in Meteoric Waters, Carbonates, and Biological Apatites: Implications for Continental Paleoclimate Reconstruction. Reviews in Mineralogy & Geochemistry 86, 429–462. https://doi.org/10.2138/rmg.2021.86.13

Pasteris, J. D., Wopenka, B., Valsami-Jones, E. (2008). Bone and tooth mineralization: Why apatite? Elements 4, 97–104. https://doi.org/10.2113/GSELEMENTS.4.2.97.

Pasteris, J. D., Ding, D. Y. (2009). Experimental fluoridation of nanocrystalline apatite. American Mineralogist 94, 53–63. https://doi.org/10.2138/am.2009.2926.

Pasteris, J. D., Yoder, C. H., Wopenka, B. (2014). Molecular water in nominally unhydrated carbonated hydroxylapatite: The key to a better understanding of bone mineral. American Mineralogist 99, 16–27. https://doi.org/10.2138/am.2014.4627.

Pemmer, B., Roschger, A., Wastl, A., Hofstaetter, J. G., Wobrauschek, P., Simon, R., Thaler, H. W., Roschger, P., Klaushofer, K., & Streli, C. (2013). Spatial distribution of the trace elements zinc, strontium and lead in human bone tissue. Bone, 57, 184–193. https://doi.org/10.1016/j.bone.2013.07.038.

Penel, G., Leroy, G., Rey, C., Sombret, B., Huvenne, J. P., Bres, E. (1997). Infrared and Raman microspectrometry study of fluor-fluor-hydroxy and hydroxy-apatite powders. Journal of Materials Science: Materials in Medicine 8, 271–276. https://doi.org/10.1023/A:1018504126866.

Pfretzschner, H.-U. (2000). Microcracks and fossilization of Haversian bone. Neues Jahrbuch für Geologie und Paläontologie – Abhandlungen 216, 413–432. https://doi.org/10.1127/njgpa/216/2000/413.

Pfretzschner, H.-U. (2004). Fossilization of Haversian bone in aquatic environments. Comptes. Rendus Palevol 3, 605–616. https://doi.org/10.1016/j.crpv.2004.07.006.

Pfretzschner, H.-U. (2006). Collagen gelatinization: the key to understand early bone-diagenesis. Palaeontographica Abteilung A Band 278, 135–148. https://doi.org/10.1127/pala/278/2006/135.

Philibert, J., Tixier, R. (1968). Electron penetration and the atomic number correction in electron probe microanalysis. Journal of Physics D: Applied Physics 1, 685–694. https://doi.org/10.1088/0022-3727/1/6/302.

Piga, G., Baró, M. D., Escobal, I. G., Goncalves, D., Makhoul, C, et al. (2016). A structural approach in the study of bones: fossil and burnt bones at nanosize scale. Applied Physics A 122:1031. https://doi.org/10.1007/s00339-016-0562-1.

Pike, A. W. G., Hedges, R. E. M., Van Calsteren, P. (2002). U-series dating of bone using the diffusion-adsorption model. Geochimica et Cosmochimica Acta 66, 4273–4286. https://doi.org/10.1016/S0016-7037(02)00997-3.

Plotnick, R. E., Smith, F. A., Lyons, S. K. (2016). The fossil record of the sixth extinction. Ecology Letters 19, 546-553. https://doi.org/10.1111/ele.12589.

Prieto, M. (2009). Thermodynamics of solid solution-aqueous solution systems. Reviews in Mineralogy and Geochemistry 70, 47–85. https://doi.org/10.2138/rmg.2009.70.2.

Procopio, N., Mein, C. A., Starace, S., Bonicelli, A., Williams, A. (2021). Bone diagenesis in short timescales: Insights from an exploratory proteomic analysis. Biology 10:460. https://doi.org/10.3390/biology10060460.

Pucéat, E., Reynard, B., Lécuyer, C. (2004). Can crystallinity be used to determine the degree of chemical alteration of biogenic apatites? Chemical Geology 205, 83–97. http://dx.doi.org/10.1016/j.chemgeo.2003.12.014.

Pucéat, E., Jochimski, M. M., Bouilloux, A., Monna, F., Bonin, A., et al. (2010). Revised phosphate–water fractionation equation reassessing paleotemperatures derived from biogenic apatite. Earth and Planetary Sciences Letters 298, 135–142. https://doi.org/10.1016/j.epsl.2010.07.034.

Putnis, A. (1992). An Introduction to Mineral Sciences. Cambridge University Press, Cambridge. https://doi.org/10.1017/CBO9781139170383.

Putnis, A. (2002). Mineral replacement reactions: from macroscopic observations to microscopic mechanisms. Mineralogical Magazine, 66, 689-708. https://doi.org/10.1180/0026461026650056.

Putnis, A., Putnis, C. (2007). The mechanism of reequilibration of solids in the presence of a fluid phase. Journal of Solid State Chemistry 180, 1783-1786. https://doi.org/10.1016/j.jssc.2007.03.023.

Putnis, A. (2009). Mineral replacement reactions. Reviews in Mineralogy and Geochemistry 70, 87–124. https://doi.org/10.2138/rmg.2009.70.3.

Qiao, W., Liu, Q., Li, Z., Zhang, H., Chen, Z. (2017). Changes in physicochemical and biological properties of porcine bone derived hydroxyapatite induced by the incorporation of fluoride. Science and technology of advanced materials, 18, 110–121. https://doi.org/10.1080/14686996.2016.1263140.

Rasmussen, K. L., Milner, G. R., Delbey, T., Skytte L., Lynnerup, N., et al. (2020). Trace element distribution in human cortical bone microstructure: the potential for unravelling diet and social status in archaeological bones. Heritage Science 8, 111. https://doi.org/10.1186/s40494-020-00457-1.

Reddy, S. M., Saxey, D., Rickard, W., Fougerouse, D., Montalvo, S. D., Verberne, R., Riessen, van, A. (2020). Atom probe tomography: Development and application to the geosciences. Geostandards and Geoanalytical Research 44, 5–50. https://doi.org/10.1111/ggr.12313.

Ren, C., Yu, Z., Philips, B. L., Wang, H., Ji, J., Pan, B., Li, W. (2019). Molecular-scale investigation of fluoride sorption mechanism by nanosized hydroxyapatite using ^{19}F solid-state NMR spectroscopy. Journal of Colloid and Interface Science 557, 357–366, https://doi.org/10.1016/j.jcis.2019.09.039.

Renard, F., Røyne, A., Putnis, C. V. (2019). Timescales of interface-coupled dissolution-precipitation reactions on carbonates. Geoscience Frontiers 10, 17-27. https://doi.org/ 10.1016/j.gsf.2018.02.013.

Reilly, G. C., Knapp, H. F., Stemmer, A., Niederer, P., and Knothe Tate, M. L. (2001). Investigation of the morphology of the lacunocanalicular system of cortical bone using atomic force microscopy. Annals of Biomedical Engineering 29, 1074–1081. https://doi.org/10.1114/1.1424910.

Ressler, A., Žužić, A., Ivanišević, I., Kamboj, N., Ivanković, H. (2021). Ionic substituted hydroxyapatite for bone regeneration applications: A review. Open Ceramics 6:100122. https://doi.org/10.1016/j.oceram.2021.100122.

Reynard, B., Lécuyer, C., Grandjean, P. (1999). Crystal-chemical controls on rare-earth element concentrations in fossil biogenic apatites and implications for paleoenvironmental reconstructions. Chemical Geology 155, 233–241. https://doi.org/10.1016/s0009-2541(98)00169-7.

Reynard, B., Balter, V. (2014). Trace elements and their isotopes in bones and teeth: Diet, environments, diagenesis, and dating of archeological and paleontological samples. Palaeogeography, Palaeoclimatology, Palaeoecology 416, 4–16. https://doi.org/10.1016/j.palaeo.2014.07.038.

Reynard, L. M., Henderson, G. M., Hedges, R. E. M. (2011). Calcium isotopes in archaeological bones and their relationship to dairy consumption. Journal of Archaeological Science 38, 657–664. https://doi.org/10.1016/j.jas.2010.10.017.

Reznikov, N., Almany-Magal, R., Shahar, R., Weiner, S. (2013). Three-dimensional imaging of collagen fibril organization in rat circumferential lamellar bone using a dual beam electron microscope reveals ordered and disordered sub-lamellar structures. Bone 52, 676–683. https://doi.org/10.1016/j.bone.2012.10.034.

Reznikov, N., Shahar, R., Weiner, S. (2014a). Bone hierarchical structure in three dimensions. Acta Biomaterialia 10, 3815–3826. https://doi.org/10.1016/j.actbio.2014.05.024.

Reznikov, N., Shahar, R., Weiner, S. (2014b). Three-dimensional structure of human lamellar bone: The presence of two different materials and new insights into the hierarchical organization. Bone 59, 93–104. https://doi.org/10.1016/j.bone.2013.10.023

Reznikov, N., Chase, H., Brumfeld, V., Shahar, R., Weiner, S. (2015). The 3D structure of the collagen fibril network in human trabecular bone: Relation to trabecular organization. Bone 71, 189–195. https://doi.org/10.1016/j.bone.2014.10.017.

Reznikov, N., Steele, J. A. M., Fratzl, P., Stevens, M. M. (2016). A materials science vision of extracellular matrix mineralization. Nature Reviews Materials 1:16041. https://doi.org/10.1038/natrevmats.2016.41.

Reznikov, N., Bilton, M., Lari, L., Stevens, M. M., Kröger, R. (2018). Fractal-like hierarchical organization of bone begins at the nanoscale. Science 360(6388):eaao2189. https://doi.org/10.1126/science.aao2189.

Richards, M. P., Pettitt, P. B., Trinkaus, E., Smith, F. H., Paunović, M., Karavanić, I. (2000). Neanderthal diet at Vindija and Neanderthal predation: the evidence from stable isotopes. Proceedings of the National Academy of Science of the United States of America 97, 7663–7666. https://doi.org/10.1073/pnas.120178997.

Richards, M. P., Taylor, G., Steele, T., McPherron, S. P., Soressi, M., et al. (2008). Isotopic dietary analysis of a Neanderthal and associated fauna from the site of Jonzac (Charente-Maritime), France. Journal of Human Evolution 55, 179–185. https://doi.org/10.1016/j.jhevol.2008.02.007.

Richards, M. P., Trinkaus, E. (2009). Isotopic evidence for the diets of European Neanderthals and early modern humans. Proceedings of the National Academy of Sciences Sep 106, 16034–16039. https://doi.org/10.1073/pnas.0903821106.

Richard, M., Moreno, D., Bahain, J.-J., Duval, M., Falguères, C. (2017). Electron spin resonance dating of fossil teeth: some basic guidelines to ensure optimal sampling conditions. International Journal of the French Quaternary Association 28, 155–159. https://doi.org/10.4000/quaternaire.8003.

Rickard, W., Reddy, S. M., Saxey, D., Fougerouse, D., Timms, N., et al. (2020). Novel applications of FIB-SEM-based ToF-SIMS in atom probe tomography workflows. Microscopy and Microanalysis 26, 1–8. https://doi.org/10.1017/S1431927620000136.

Rigo, J., Pieltain, C., Viellevoye, R., Bagnoli, F. (2012). Calcium and phosphorus homeostasis: Pathophysiology. In G Buonocore, R Bracci, M Weindling, Eds. Neonatology. Springer, Milano. https://doi.org/10.1007/978-88-470-1405-3_49.

Rogers, K. D., Zioupos, P. (1999). The bone tissue of the rostrum of a Mesoplodon Densirostris whale: a mammalian biomineral demonstrating extreme texture. Journal of Materials Science Letters 18, 615–654. https://doi.org/10.1023/A:1006615422214.

Romer, R. L. (2001). Isotopically heterogeneous initial Pb and continuous ^{222}Rn loss in fossils: The U-Pb systematics of *Brachiosaurus brancai.* Geochimica et Cosmochimica Acta 65, 4201–4213. https://doi.org/10.1016/S0016-7037(01)00716-5.

Rondanelli, M., Faliva, M.A., Peroni, G., Infantino, V., Gasparri, C., et al. (2020). Pivotal role of boron supplementation on bone health: A narrative review. Journal of Trace Elements in Medicine and Biology 62:126577. https://doi.org/10.1016/j.jtemb.2020.126577.

Rowland, R. E., Farnham, J. E. (1969). The deposition of uranium in bone. Health Physics 17, 139–144. https://doi.org/10.1097/00004032-196907000-00015.

Rudolph, W., Irmer, G. (2018). Hydration and Ion Pair Formation in Aqueous Lu^{3+}-Solution. Molecules 23, 3237. https://doi.org/10.3390/molecules23123237.

Ruiz-Agudo, E., King, H. E., Patiño-López, L. D., Putnis, C. V., Geisler, T. et al. (2016). Control of silicate weathering by interface-coupled dissolution-precipitation processes at the mineral-solution interface. Geology 44, 567-570. https://doi.org/10.1130/G37856.1.

Sadat-Shojai, M., Khorasani, M.-T., Dinpanah-Khoshdargi, E., Jamshidi, A., (2013). Synthesis methods for nanosized hydroxyapatite with diverse structures. Acta Biomaterialia 9, 7591-7621. https://doi.org/10.1016/j.actbio.2013.04.012.

Saloman, E. B., Craig, J.S. (2006). Wavelengths, energy level classifications, and energy levels for the spectrum of neutral neon. Journal of Physical and Chemical Reference Data 35, 1113–1119. https://doi.org/10.1063/1.2204960.

Scott, G. R., Poulson, S. R. (2012). Stable carbon and nitrogen isotopes of human dental calculus: a potentially new non-destructive proxy for paleodietary analysis. Journal of Archaeological Science. 39, 1388–1393. https://doi.org/10.1016/j.jas.2011.09.029.

Schindelin, J.; Arganda-Carreras, I. & Frise, E. et al. (2012), "Fiji: an open-source platform for biological-image analysis", Nature methods 9, 676–682, PMID 22743772, https://doi.org/10.1038/nmeth.2019.

Schoeninger, M. J., DeNiro, M. J. (1984). Nitrogen and carbon isotopic composition of bone collagen from marine and terrestrial animals. Geochimica et Cosmochimica Acta 48, 625–639.

Schopf, W. J., Kitajima, K., Spicuzza, M. J., Kudryavtsev, A. B., Valley, J. W. (2018). SIMS analyses of the oldest known assemblage of microfossils document their taxon-correlated carbon isotope compositions. Proceedings of the National Academy of Sciences 115, 53–58. https://doi.org/10.1073/pnas.1718063115.

Shoulders, M. D., Raines, R. T., (2009). Collagen structure and stability. Annual review of biochemistry 78, 929–958. https://doi.org/10.1146/annurev.biochem.77.032207.120833.

Schweizer, M. K., Steele, A., Torporski, J. K. W., Fogel, M. L. (2007). Stable isotopic evidence for fossil food webs in Eocene Lake Messel. Paleobiology 33, 590–609.

Shah, F.A. (2020). Towards refining Raman spectroscopy-based assessment of bone composition. Scientific Reports 10:16662. https://doi.org/10.1038/s41598-020-73559-2.

Simpson, R., Cooper, D. M. L., Swanston, T., Coulthard, J., Varney, T. L. (2021). Historical overview and new directions in bioarchaeological trace element analysis: a review. Archaeological and Anthropological Sciences 13, 24. https://doi.org/10.1007/s12520-020-01262-4.

Smith, D. W., Gardiner, B. S., Dunstan, C. (2012). Bone balance within a cortical BMU: Local controls of bone resorption and formation. PLoS ONE 7:e40268. https://doi.org/10.1371/journal.pone.0040268.

Smolek, S., Streli, C., Zoeger, N., Wobrauschek, P. (2010). Improved micro x-ray fluorescence spectrometer for light element analysis. The Review of scientific instruments 81: 053707. https://doi.org/10.1063/1.3428739.

Snoeck, C., Lee-Thorp, J., Schulting, R., De Jong, J., Debouge, W., Mattielli, N. (2015). Calcined bone provides a reliable substrate for strontium isotope ratios as shown by an enrichment experiment. Rapid communications in mass spectrometry 29, 107–114. https://doi.org/10.1002/rcm.7078.

Sommerfeldt, D., Rubin, C. (2001). Biology of bone and how it orchestrates the form and function of the skeleton. European Spine Journal 10, 86–95. https://doi.org/10.1007/s005860100283.

Snoeck, C., Lee-Thorp, J., Schulting, R., Jong, J. de, Debouge, W., Mattielli, N. (2015). Calcined bone provides a reliable substrate for strontium isotope ratios as shown by an enrichment experiment. Reviews in Cardiovascular Medicine 29, 107–114. https://doi.org/10.1002/rcm.7078.

Sponheimer, M., Lee-Thorp, J. A. (1999). Oxygen Isotopes in Enamel Carbonate and their Ecological Significance. Journal of Archaeological Science 26, 723–1728. https://doi.org/10.1006/jasc.1998.0388.

Sponheimer, M., Lee-Thorp, J.A. (2006). Enamel diagenesis at South African Australopith sites: Implications for paleoecological reconstruction with trace elements. Geochimica et Cosmochimica Acta 70, 1644–1654. https://doi.org/10.1016/j.gca.2005.12.022.

Sternitzke, V., Kaegi, R., Audinot, J.-N., Lewin, E., Hernig, J. G., Kohnson, C. A. (2012). Uptake of fluoride from aqueous solution on nano-sized hydroxyapatite: examination of a fluoridated surface layer. Environmental Science & Technology 46, 802–809. https://doi.org/10.1021/es202750t.

Streli, C., Rauwolf, M., Turyanskaya A., Ingerle, D., Wobrauschek, P. (2019). Elemental imaging of trace elements in bone samples using micro and nano-X-ray fluorescence spectrometry. Applied Radiation and Isotopes 149, 200–205. https://doi.org/10.1016/j.apradiso.2019.04.033.

Suarez, C. A., Macpherson, G. L., González, L. A., Grandstaff, D. E. (2010). Heterogeneous rare earth element (REE) patterns and concentrations in a fossil bone: Implications for the use of REE in vertebrate taphonomy and fossilization history. Geochimica et Cosmochimica Acta74, 2970–2988. https://doi.org/10.1016/j.gca.2010.02.023.

Suarez, M. B., Passey, B. H. (2014). Assessment of the clumped isotope composition of fossil bone carbonate as a recorder of subsurface temperatures. Geochimica et Cosmochimica Acta 140, 142–159. https:/doi.org/ 10.1016/j.gca.2014.05.026.

Syku, M., Pawełczy, S., Borowik, T., Pokorny, B., Flajšman, K., et al. (2021). Environmental factors shaping stable isotope signatures of modern red deer (Cervus elaphus) inhabiting various habitats. PLoS ONE 16: e0255398. https://doi.org/10.1371/journal.pone.0255398.

Tacail, T., Le Houedec, S., Skulan, J.L. (2020). New frontiers in calcium stable isotope geochemistry: perspectives in present and past vertebrate biology. Chemical Geology 537:119471. https://doi.org/10.1016/j.chemgeo.2020.119471.

Talal, A., Hamid, S. K., Khan, M., Khan, A. S. (2020). Structure of biological apatite: bone and tooth. In Handbook of Ionic Substituted Hydroxyapatites. AS Khan, AA Chaudhry, Eds. Woodhead Publishing, 1–19. https://doi.org/10.1016/B978-0-08-102834-6.00001-X.

Tanabe, K., Hiraishi, J. (1980). Correction of finite slit width effects on Raman line widths. Spectrochimica Acta Part A: Molecular Spectroscopy 36, 341–344. https://doi.org/10.1016/0584-8539(80)80141-3.

Taylor, R. E. (1992). Radiocarbon dating of bone: To collagen and beyond. In Taylor, R. E., Long, A., Kra, R. S. (Eds). Radiocarbon After Four Decades. Springer, New York, NY. https://doi.org/10.1007/978-1-4757-4249-7_25

Taylor, R. E. (2000). Fifty years of radiocarbon dating: This widely applied technique has made major strides since its introduction a half-century ago at the University of Chicago. American Scientist 88, 60–67. http://www.jstor.org/stable/27857964.

Taylor, L. D., O'Dea, A., Bralower, T. J., Finnegan, S. (2019). Isotopes from fossil coronulid barnacle shells record evidence of migration in multiple Pleistocene whale populations. Proceedings of the National Academy of Sciences of the United States of America 116, 7377–7381. https://doi.org/10.1073/pnas.1808759116.

Thomas, D. B., Fordyce, R. E., Russel, D. F., Gordon, K. C. (2007). A rapid, non-destructive method of detecting diagenetic alteration in fossil bone using Raman spectroscopy. Journal of Raman Spectroscopy 38, 1533–1537. https://doi.org/10.1002/jrs.1851.

Thomas, D. B., McGoberin, C. M., Fordyve, R. E., Russel, D. F., Gordon, K. C. (2011). Raman spectroscopy of fossil bioapatite — A proxy for diagenetic alteration of the oxygen isotope composition. Palaeogeography, Palaeoclimatology, Palaeoecology 310, 62–70. https://doi.org/10.1016/j.palaeo.2011.06.016.

Tomaschek, F., Keiter, M., Kennedy, A. K., Ballhaus, C. (2008). Pre-alpine basement within the northern cycladic blueschist unit on Syros Island, Greece. Zeitschrift der deutschen Gesellschaft für Geowissenschaften. 159, 521–531. https://doi.org/10.1127/1860-1804/2008/0159-0521.

Tonegawa, T., Ikoma, T., Yoshioka, T., Hanagata, N., Tanaka, J. (2010). Crystal structure refinement of A-type carbonate apatite by X-ray powder diffraction. Journal of Materials Science 45, 2419–2426. https://doi.org/10.1007/s10853-010-4209-x.

Toots, H., Voorhies, M. R. (1965). Strontium in fossil bones and the reconstruction of food chains. Science 149, 854–855. https://doi.org/10.1126/science.149.3686.854.

Trueman, C. N., Benton, M. J. (1997). A geochemical method to trace the taphonomic history of reworked bones in sedimentary settings. Geology 25, 263-266. https://doi.org/10.1130/0091-7613(1997)025<0263:AGMTTT>2.3.CO;2.

Trueman, C. N. (1999). Rare earth element geochemistry and taphonomy of terrestrial vertebrate assemblages. PALAIOS 14, 555-568. https://doi.org/10.2307/3515313.

Trueman, C N., Martill, D. M. (2002). The long–term survival of bone: the role of bioerosion. Archaeometry 44, 371-381. https://doi.org/10.1111/1475-4754.t01-1-00070.

Trueman, C. N., and Tuross, N. (2002). Trace elements in recent and fossil bone apatite. Reviews in Mineralogy and Geochemistry 48, 489–521. https://doi.org/10.2138/rmg.2002.48.13.

Trueman, C.N.G., Behrensmeyer, A.K., Tuross, N., Weiner, S. (2004). Mineralogical and compositional changes in bones exposed on soil surfaces in Amboseli National Park, Kenya: diagenetic mechanisms and the role of sediment pore fluids. Journal of Archaeological Science. 31, 721–739. https://doi.org/10.1016/j.jas.2003.11.003.

Trueman, C. N., Behrensmeyer, A. K., Potts, R., Tuross, N. (2006). High-resolution records of location and stratigraphic provenance from the rare earth element composition of fossil bones. Geochimica et Cosmochimica Acta70, 4343–4355. https://doi.org/10.1016/j.gca.2006.06.1556.

Trueman, C. N., Privat, K., and Field, J. (2008). Why do crystallinity values fail to predict the extent of diagenetic alteration of bone mineral? Palaeogeography, Palaeoclimatology, Palaeoecology 266, 160–167. https://doi.org/10.1016/j.palaeo.2008.03.038.

Trueman, C. N., Kocsis, L., Palmer, M. R., Dewdney, C. (2011). Fractionation of rare earth elements within bone mineral: A natural cation exchange system. Palaeogeography, Palaeoclimatology, Palaeoecology 310, 124–132. https://doi.org/10.1016/j.palaeo.2011.01.002.

Trueman, C. N. (2013). Chemical taphonomy of biomineralized tissues. Paleontology 56, 475–486. https://doi.org/10.1111/pala.12041.

Turner-Walker, G. (2011). The mechanical properties of artificially aged bone: probing the nature of the collagen-mineral bond. Palaeogeography, Palaeoclimatology, Palaeoecology 310, 17–22. https://doi.org/10.1016/j.palaeo.2011.03.024.

Turner-Walker, G. (2012). Early bioerosion in skeletal tissues: persistence through deep time. Neues Jahrbuch für Geologie und Paläontologie – Abhandlungen 265, 165–183. https://doi.org/10.1127/0077-7749/2012/0253.

Turner-Walker, G. (2019). Light at the end of the tunnels? The origins of microbial bioerosion in mineralised collagen. Palaeogeography, Palaeoclimatology, Palaeoecology 529, 24–38. https://doi.org/10.1016/j.palaeo.2019.05.020.

Turyanskaya, A., Smetaczek, S., Pichler, V., Rauwolf, M., Perneczky L., et al. (2021). Correlation of µXRF and LA-ICP-MS in the analysis of a human bone-cartilage sample. Journal of Analytical Atomic Spectrometry 36, 1512–1523. https://doi.org/10.1039/D1JA00007A.

Tuschel, D. (2016). Photoluminescence spectroscopy using a Raman spectrometer. Spectroscopy 31, 14–21.

Tütken, T. (2003). Die Bedeutung der Knochenfrühdiagenese für die Erhaltungsfähigkeit in vivo erworbener Element- und Isotopenzusammensetzungen in fossilen Knochen. PhD Thesis, Universität Tübingen, 334 pp. Online dissertation: http://tobias-lib.uni-tuebingen.de/volltexte/2003/962/.

Tütken, T., Vennemann, T. W., Pfretzschner, H.-U. (2008). Early diagenesis of bone and tooth apatite in fluvial and marine settings: Constraints from combined oxygen isotope, nitrogen and REE analysis. Paleogeography, Palaeoclimatology, Palaeoecology, 266, 254–268. https://doi.org/10.1016/j.palaeo.2008.03.0.

Tütken, T., Vennemann, T. W. (2011). Fossil bones and teeth: Preservation or alteration of biogenic compositions? Palaeogeography, Palaeoclimatology, Palaeoecology, 310, 1-8. https://doi.org/10.1016/j.palaeo.2011.06.020.

Tütken, T., Vennemann, T. W., Pfretzschner, H.-U. (2011). Nd and Sr isotope compositions in modern and fossil bones - Proxies for vertebrate provenance and taphonomy. Geochimica et Cosmochimica Acta 75, 5951–5970. https://doi.org/10.1016/j.gca.2011.07.024.

Tütken, T. (2014). Isotope compositions (C, O, Sr, Nd) of vertebrate fossils from the Middle Eocene oil shale of Messel, Germany: Implications for their taphonomy and palaeoenvironment. Palaeogeography, Palaeoclimatology, Palaeoecology 416, 92–109. https://doi.org/10.1016/j.palaeo.2014.08.005.

Tütken, T., Weber, M., Zohar, I., Helmy, H., Bourgon, N., et al. (2020). Strontium and Oxygen Isotope Analyses Reveal Late Cretaceous Shark Teeth in Iron Age Strata in the Southern Levant. Frontiers in Ecology and Evolution 8:570032. https://doi.org/10.3389/fevo.2020.570032.

Tzaphlidoi, M. (2008). Bone architecture: collagen structure and calcium/phosphorus maps. Journal of Biological Physics 34, 39–49. https://doi.org/10.1007/s10867-008-9115-y.

Ullmann, P. V., Voegele, K. K., Grandstaff, D. E., Ash, D. A., Zheng, W., et al. (2020). Molecular tests support the viability of rare earth elements as proxies for fossil biomolecule preservation. Scientific Reports 10:15566. https://doi.org/10.1038/s41598-020-72648-6.

Vellet-Regí, M., Arcos, D. (2016). Biological apatites in bone and teeth. In Nanoceramics in Clinical Use: From Materials to Applications (2). M Vallet-Regí, D Arcos, Eds. The Royal Society of Chemistry, 1–29. http://doi.org/10.1039/9781782622550-00001.

Valsami-Jones, E., Ragnarsdottir, K.V., Putnis, A., Bosbach, D., Kemp, G., Cressey, G. (1998). The dissolution of apatite in the presence of aqueous metal cations at pH 2–7. Chemical Geology 151, 215–233. https://doi.org/10.1016/S0009-2541(98)00081-3.

Van der Plicht, J., Palstra, S. W. L. (2016). Radiocarbon and mammoth bones: What's in a date', Quaternary International 406, 246–251. https://doi.org/10.1016/j.quaint.2014.11.027.

Varga, P., Hesse, B., Langer, M., Schrof, S., Männicke, N., et al. (2014). Synchrotron X-ray phase nano-tomography-based analysis of the lacunar–canalicular network morphology and its relation to the strains experienced by osteocytes in situ as predicted by case-specific finite element analysis. Biomechanics and Modeling in Mechanobiology 14, 267–282. https://doi.org/10.1007/s10237-014-0601-9.

Voigt, M., Mavromatis, V., Oelkers, E. H. (2017). The experimental determination of REE partition coefficients in the water-calcite system. Chemical Geology 462, 30–43. https://doi.org/10.1016/j.chemgeo.2017.04.024.

Wang, Y., Cerling, T. E. (1994). A model of fossil tooth and bone diagenesis: Implications for paleodiet reconstruction from stable isotopes. Palaeogeography, Palaeoclimatology, Palaeoecology 107, 281–289. https://doi.org/10.1016/0031-0182(94)90100-7.

Wang, J., Bourgeois, D., Meyer, D. (2020). Mimicking bone–metal exchanges with synthetic nanocrystalline apatites. Material Advances 1, 3292–3301. http://dx.doi.org/ 10.1039/ D0MA00398K.

Weber, M., Tacail, T., Lugli, F., Clauss, M., Weber, K., et al. (2020). Strontium uptake and intra-population $^{87}Sr/^{86}Sr$ variability of bones and teeth—Controlled feeding experiments with rodents (Rattus norvegicus, Cavia porcellus). Frontiers in Ecology and Evolution 8:569940. https://doi.org/10.3389/fevo.2020.569940.

Weber, K., Weber, M., Menneken, M., Kral, A. G., Mertz-Kraus, R., Geisler, T., Vogl, J., Tütken, T. (2021). Diagenetic stability of non-traditional stable isotope systems (Ca, Sr, Mg, Zn) in teeth – An in-vitro alteration experiment of biogenic apatite in isotopically enriched tracer solution. Chemical Geology 572:120196. https://doi.org/10.1016/j.chemgeo.2021.120196.

White, L., Booth, T. J. (2014). The origin of bacteria responsible for bioerosion to the internal bone microstructure: Results from experimentally-deposited pig carcasses. Forensic Science International 239, 92–102. https://doi.org/10.1016/j.forsciint.2014.03.024.

Wierzbowski, H. (2021). Advances and Challenges in Palaeoenvironmental Studies Based on Oxygen Isotope Composition of Skeletal Carbonates and Phosphates. Geosciences 11:419. https://doi.org/10.3390/geosciences11100419.

Williams, C. T., Henderson, P., Marlow, C. A., Molleson, T. I. (1997). The environment of deposition indicated by the distribution of rare elements in fossil bones from Olduvai Gorge, Tanzania. Applied Geochemistry 12, 537–547.

Willoughby, E. (2016). Radiometric dating and the age of the Earth. In Kane, J., Willoughby, E., Keesey, T. M. (Eds). God’s Word or Human Reason? An Inside Perspective on Creationism. Portland, OR: Inkwater Press, 57–103.

Wings, O. (2004). Authigenic minerals in fossil bones from the Mesozoic of England: Poor correlation with depositional environments. Palaeogeography, Palaeoclimatology, Palaeoecology 204, 15–32. https://doi.org/10.1016/S0031-0182(03)00709-0.

Winter, E. R. S., Carlton, M., Briscoe, H. V. A. (1940). The interchange of heavy oxygen between water and inorganic oxy-anions. Journal of the Chemical Society 0, 131–138. https://doi.org/10.1039/JR9400000131.

Wißing, C., Rougier, H., Baumann, C., Comeyne, A., Crevecoeur, I., et al. (2019). Stable isotopes reveal patterns of diet and mobility in the last Neandertals and first modern humans in Europe. Scientific Reports 9:4433. https://doi.org/10.1038/s41598-019-41033-3.

Wopenka, B., Pasteris, J. D. (2005). A mineralogical perspective on the apatite in bone. Materials Science and Engineering: C, 25, 131–143. https://doi.org/10.1016/j.msec.2005.01.008.

You, L.-D., Weinbaum, S., Cowin, S. C., Schaffler, M. B. (2004). Ultrastructure of the osteocyte process and ist pericellular matrix. The Anatomical Record 278A, 505–513. https://doi.org/10.1002/ar.a.20050.

Zazzo, A., Lécuyer, C., Mariotti, A. (2004). Experimentally controlled carbon and oxygen isotope exchange between bioapatites and water under inorganic and microbially-mediated conditions. Geochimica et Cosmochimica Acta 68, 1–12. https://doi.org/10.1016/S0016-7037(03)00278-3.

Zazzo, A., Saliège, J. (2011). Radiocarbon dating of biological apatites: A review. Palaeogeography, Palaeoclimatology, Palaeoecology 310, 52–61. https://doi.org/10.1016/j.palaeo.2010.12.004.

Zazzo, A., Saliège, J., Lebon, M., Lepetz, S., Moreau, C. (2012). Radiocarbon dating of calcined bones: insights from combustion experiments under natural conditions. Radiocarbon 54, 855-866. https://doi.org/10.1017/S0033822200047500.

Webpages:

North Dakota Studies, State Historical Society of North Dakota. Accessed 02 March 2022, https://www.ndstudies.gov/gr8/content/unit-i-paleocene-1200-ad/lesson-1-changing - landscapes/topic-3-plants-and-animals/section-3-animals.

Wikimedia Commons, Public domain, Hardwigg. Accessed 10 April 2022, https://commons.wikimedia.org/wiki/File:Geologic_Clock_with_events_and_periods.svg.